STRUCTURAL AND MORPHOLOGIC STUDY OF SHATSKY RISE OCEANIC PLATEAU IN THE NORTHWEST PACIFIC OCEAN FROM 2D MULTICHANNEL SEISMIC REFLECTION AND BATHYMETRY DATA AND IMPLICATIONS FOR OCEANIC PLATEAU EVOLUTION

A Dissertation

by

JINCHANG ZHANG

Submitted to the Office of Graduate and Professional Studies of
Texas A&M University
in partial fulfillment of the requirements for the degree of

DOCTOR OF PHILOSOPHY

Chair of Committee,	William W. Sager
Co-Chair of Committee,	Zuosheng Yang
Committee Members,	Mitch W. Lyle
	Richard L. Gibson
Head of Department,	Debbie J. Thomas

May 2014

Major Subject: Oceanography

ABSTRACT

Shatsky Rise is one of the largest oceanic plateaus, a class of volcanic features whose formation is poorly understood. It is also a plateau that was formed near spreading ridges, but the connection is unclear. The geologic structure and morphology of Shatsky Rise oceanic plateau provides key observations that can help understand its formation. Deep penetrating 2D multichannel seismic (MCS) reflection profiles and high-resolution multi-beam sonar data were acquired over the southern half of Shatsky Rise on *R/V Marcus G. Langseth* during two cruises. The MCS profiles allow us to image Shatsky Rise's upper crustal structure and Moho structure with unprecedented detail, and the multi-beam bathymetry data allow us to produce an improved bathymetric map of the plateau. MCS profiles and bathymetry data show that two of the volcanic massifs within Shatsky Rise are immense central volcanoes. Tamu Massif, the largest (~450 × 650 km) and oldest (~145 Ma) volcano, is a single central volcano with rounded shape and shallow flank slopes (<0.5^{o}-1.5^{o}), characterized by lava flows emanating from the volcano center and extending hundreds of kilometers down smooth, shallow flanks to the surrounding seafloor. Ori Massif is another large volcano that is similar, but smaller in size than Tamu Massif. The morphology of the massifs implies formation by extensive and far ranging lava flows emplaced at small slope angles. The relatively smooth flanks of the massifs imply that the volcanoes were not greatly affected by rifting due to spreading ridge tectonics. Several down-to-basin faults observed on the flanks of the massifs are not parallel to magnetic lineations, suggesting that they were

not formed by seafloor spreading. The Moho of Shatsky Rise starts shallow (~6-7 km) beneath normal crust at the distal flanks and dips (~3^{o}-5^{o}) towards the center of plateau massifs, reaching maximum thickness of ~ 30 km. Shatsky Rise crustal structure is consistent with the Moho topography of isostatically compensated crustal structures, which is why the plateau exhibits a small free-air gravity anomaly signature. Shatsky Rise was built on young oceanic lithosphere with little rigidity, so the plateau formed in isostatic equilibrium with a deep crustal root.

ACKNOWLEDGEMENTS

I would like to thank my advisor and committee chair, Dr. Sager, and my committee co-chair, Dr. Yang, and my other committee members, Dr. Lyle and Dr. Gibson, for their guidance throughout my dissertation work. I also want to thank the following people for helping me through my research: Dr. Korenaga, Dr. Floyd, William Durkin, Chris Paul, and the Captain, crew, and technical staff of *R/V Marcus G. Langseth*.

I am grateful for National Science Foundation and China Scholarship Council to support my entire Ph. D study at Texas A&M University.

I would also like to thank my family for their unconditional love, especially, my wife, Jie Chen.

Lastly, I would appreciate my friends and colleagues for making my time at Texas A&M University a great experience.

NOMENCLATURE

CDP	Common depth point
CVS	Constant velocity stack
IODP	Integrated ocean drilling program
MCS	Multichannel seismic
OBS	Ocean bottom seismometer
ODP	Ocean drilling program
SP	Shot point
TWTT	Two-way travel time

TABLE OF CONTENTS

Page

LIST OF FIGURES

Page

CHAPTER I

INTRODUCTION

Oceanic plateaus, the largest of the large igneous provinces (LIPs) in the deep ocean basins, are broad, more or less flat-topped undersea mountains that typically cover areas of millions of square kilometers, have volumes of millions of cubic kilometers, and rise thousands of meters above surrounding seafloor (Coffin and Eldholm, 1994; Sager et al., 1999). Most are formed by basaltic volcanism and associated igneous intrusions. Such giant volcanic edifices, with their anomalously thick oceanic crust, imply extraordinary fluxes of magma from the mantle to the lithosphere (Coffin and Eldholm, 1994; Ridley and Richards, 2010). Therefore, their formation and evolution can be important to indicate both regional tectonic events and mantle behavior and geodynamics (Sager et al., 1999). Unfortunately, oceanic plateau volcanic processes remain poorly understood because oceanic plateaus are hidden beneath the sea in remote locations far from land and are often covered by thick sediment layers, all of which make it difficult to sample and study oceanic plateaus in great detail.

Oceanic plateaus are such large volcanic features that they must have formed from some anomalous mantle process, such as a mantle plume (Sager et al., 1999), but there is ongoing debate about their origins. Several mechanisms have been proposed for the origin of oceanic plateaus. One class of mechanisms involves decompression melting of fertile upper mantle material at plate boundaries or cracks in the plates, such as leaky transform faults (Hilde et al., 1976), spreading ridge reorganizations (Anderson et al.,

1992; Foulger, 2007) and where changes in plate stress weaken the lithosphere (Saunders, 2005). However, it is hard to explain the huge volumes of magma required for building large oceanic plateaus. A second class is based on the mantle plume hypotheses. Many workers think that oceanic plateaus form when the voluminous, rising head of a nascent mantle plume arrives at the lithosphere (the "plume head" hypothesis) (Richards et al., 1989; Mahoney and Spencer, 1991; Duncan and Richards, 1991; Coffin and Eldholm, 1994). Although this model can explain many features of large oceanic plateaus, it still needs further modification and alternative development to incorporate additional complexities. For example, the bulk of Ontong Java Plateau never reached sea level contrary to the expectation from the dynamic uplift of a plume head (Korenaga, 2005), and rocks recovered from the main Shatsky Rise edifices show Mid-Ocean Ridge basalt geochemistry and isotopic signatures whereas most plume head models imply lower mantle materials carried to the surface (Mahoney et al., 2005; Sager, 2005). Another explanation is cosmic - that plateaus are the result of a large meteorite impact (Rogers, 1982; Ingle and Coffin, 2004), lack of evidence linking plateaus and impacts has limited acceptance of this hypothesis.

Among large oceanic plateaus all around the world, Shatsky Rise has a combination of factors that make it important for studying the problem of plateau evolution. Firstly, it has an area of 4.8×10^5 km^2 and a volume of 4.3×10^6 km^3 (Sager et al., 1999), which makes it big enough for an typical example of large oceanic plateaus, but not so large as to be extremely difficult to study. Its original size may have been approximately double its current size because it was formed at a spreading ridge triple

junction (Nakanishi et al., 1999), so half may have been carried away on other plates that are now subducted. Moreover, the output of the mantle source may have been significantly greater if the suggested link between Shatsky Rise and Hess Rise sources is correct (Bercovici and Mahoney, 1994). Secondly, Shatsky Rise formed at a time of magnetic reversals, during the Late Jurassic and Early Cretaceous. This means that the evolution of coeval oceanic spreading ridges, near which it formed, can be traced through time (e.g., Nakanishi et al., 1999). In contrast, many other oceanic plateaus in the Pacific formed during the Cretaceous Normal Superchron or "Cretaceous Quiet Period", a time during which the magnetic field ceased reversing, making it impossible to reconstruct the tectonic history of those plateaus from magnetic anomalies. Thirdly, it was created at a ridge-ridge-ridge triple junction (Larson and Chase 1972; Hilde et al., 1976; Sager et al., 1988; Nakanishi et al., 1999), which suggests a link to a plate boundary (spreading ridge) and allows tests of plume versus plate boundary processes as mechanisms of oceanic plateau formation. In addition, volcanism on Shatsky Rise is laterally spread out and sediments deposited on the flanks are thin, which makes it easier to sample volcanic basement and to see the morphology of the plateau from bathymetry data. Thus, Shatsky Rise combines several salutary situations that make it an important plateau to study for understanding the formation of these enigmatic features.

In my research, I studied three themes that contribute to our knowledge of the structure and morphology of Shatsky Rise and implications for oceanic plateau evolution. First theme is the upper crustal structure of Shatsky Rise. Second is deep crustal structure of the plateau. Third is the morphology of the rise. The results of these

themes are discussed in following chapters. Chapter II describes upper crustal structure of Shatsky Rise using deep penetrating 2D multichannel seismic reflection (MCS) profiles collected over the southern half of the plateau. Chapter III examines deep reflectors in the MCS reflection data and combines with wide-angle seismic refraction data to show the geometry of the Moho and give a complete view of deep crustal structure of Shatsky Rise. Chapter IV demonstrates morphologic features over Shatsky Rise from new high-resolution bathymetry data acquired by multi-beam sonar from recent surveys and combined with previous bathymetry data. Chapter V provides a summary of conclusions from studies mentioned above.

CHAPTER II

SHATSKY RISE OCEANIC PLATEAU STRUCTURE FROM 2D MULTICHANNEL SEISMIC REFLECTION PROFILES

2.1 Overview

Shatsky Rise is one of the largest oceanic plateaus, a class of volcanic feature whose formation is poorly understood. It is also a plateau that was formed near spreading ridges, but the connection is unclear. The geologic structure of Shatsky Rise is a key observation that can help understand its formation. Deep penetrating 2D multichannel seismic (MCS) reflection profiles were acquired over the southern half of Shatsky Rise and these data allow us to image its upper crustal structure with unprecedented detail. Synthetic seismograms constructed from core and log data from scientific drilling sites crossed by the MCS lines establish the seismic response to geology. High amplitude basement reflections result from the transition between sediment and underlying igneous rock. Intra-basement reflections are caused by alternations of lava flow packages with differing properties and by thick inter-flow sediment layers. MCS profiles show that two of the volcanic massifs within Shatsky Rise are immense central volcanoes. Tamu Massif, the largest (~450 x 650 km) and oldest (~145 Ma) volcano, is a single central volcano with rounded shape and shallow flank slopes (<0.5o-1.5o), characterized by lava flows emanating from the volcano center and extending hundreds of kilometers down smooth, shallow flanks to the surrounding seafloor. Ori Massif is another large volcano that is similar, but smaller in

size than Tamu Massif. The morphology of the massifs implies formation by extensive and far ranging lava flows emplaced at small slope angles. The relatively smooth flanks of the massifs imply that the volcanoes were not greatly affected by rifting due to spreading ridge tectonics. Observation of deep intra-basement reflectors parallel to the upper basement surface implies long-term isostasy, with the balanced addition of material to the surface and subsurface. No evidence of subaerial erosion is found at the summits of the massifs, suggesting that they were never highly emergent.

2.2 Introduction

Oceanic plateaus are extensive undersea mountains often rising thousands of meters above surrounding seafloor, with areas that can be in the millions of square kilometers and volumes as much as millions of cubic kilometers (Coffin and Eldholm, 1994). Many are large basaltic volcanic edifices with anomalously thick crust implying extraordinary fluxes of magma from the mantle to the lithosphere (Coffin and Eldholm, 1994; Ridley and Richards, 2010). Thus, plateau formation can be an important indication of regional tectonic events and mantle behavior.

Oceanic plateaus are broad volcanoes with shallow slopes of only ~1 °-2 °or less (Coffin and Eldholm, 1994). In spite of similar compositions, they differ in size and morphology from the greatly numerous smaller volcanic seamounts, which are characterized by steeper slopes (~5 °or greater) (Smith, 1988). How plateaus form is poorly understood and several mechanisms have been proposed for their origin. One class of proposed mechanisms envisions decompression melting of fertile upper mantle

material at plate boundaries or cracks in the plates, such as leaky transform faults (Hilde et al., 1976), spreading ridge reorganizations (Anderson et al., 1992; Foulger, 2007), and/or weaknesses in the lithosphere caused by changes in plate stress (Saunders, 2005). However, it is difficult to explain the huge volumes of magma required for building large oceanic plateaus with these mechanisms (e.g. Coffin and Eldholm, 1994). An alternate explanation is the mantle plume hypothesis. Many workers think that oceanic plateaus form when the voluminous, rising head of a nascent mantle plume arrives at the base of the lithosphere (the "plume head" hypothesis) (Richards et al., 1989; Mahoney and Spencer, 1991; Duncan and Richards, 1991; Coffin and Eldholm, 1994). Although this model is widely accepted and can explain some features of oceanic plateaus, there are notable exceptions. For example, rocks recovered from the main Shatsky Rise volcanoes are similar to mid-ocean ridge basalts in geochemistry and isotopic signatures, whereas most plume head models imply that lower mantle material is carried to the surface (Mahoney et al., 2005; Sager, 2005). A third suggested formation mechanism is cosmic - that plateaus are the result of a large meteorite impact (Rogers, 1982; Ingle and Coffin, 2004). Lack of evidence linking plateaus and impacts has led to the limited acceptance of this hypothesis.

Among oceanic plateaus, Shatsky Rise is unusual for oceanic plateaus because it has characteristics that fit both the mantle plume and plate edge hypotheses (Sager, 2005). Magnetic lineations show that it formed at a triple junction (Nakanishi et al., 1999), thus its formation is linked to plate boundaries. Moreover, the morphology of Shatsky Rise suggests that it began forming with an enormous eruption, followed by

lesser eruptions, as could be expected of the transition between plume head and plume tail (Sager and Han, 1993; Sager et al., 1999; Sager, 2005). Shatsky Rise was recently drilled on Integrated Ocean Drilling Program (IODP) Expedition 324 (Sager et al., 2010), but its structure is still poorly known because it has not been imaged by modern deep-penetration seismic data. The seismic vessel R/V Marcus G. Langseth visited Shatsky Rise on two cruises to acquire new marine seismic data. During one of these cruises, wide-angle seismic refraction data were collected over the southern Shatsky Rise and were reported elsewhere (Korenaga and Sager, 2012). Deep penetrating 2D multichannel seismic (MCS) reflection profiles were collected on both cruises over the southern half of Shatsky Rise and these data allow us to image the structure of the plateau with unprecedented detail. In this chapter, I describe the upper crustal structure of Shatsky Rise using the MCS profiles and discuss implications for oceanic plateau formation.

2.2.1 Geologic background

Shatsky Rise is located in the northwest Pacific Ocean, ~1600 km east of Japan (Figure 26). It has dimensions of ~450 km x 1650 km and has an area equivalent to Japan or California. Its summits reach 2000-3000 m depth and it is surrounded by regional seafloor of 5500-6000 m depth. Shatsky Rise consists of three bathymetric highs, Tamu Massif, Ori Massif, and Shirshov Massif, as well as a low ridge, Papanin Ridge, arranged in a SW-NE trend (Figure 26). The plateau has an estimated volume of 4.3x106 km3 (Sager et al., 1999), yet its original size may have been even larger because

it was formed at a ridge-ridge-ridge triple junction (Nakanishi et al., 1999), so part may have been carried away on other plates that are now subducted. Moreover, the total output of the mantle source may have been significantly greater if both Shatsky Rise and Hess Rise were formed from the same source, as suggested by Bercovici and Mahoney (1994).

Shatsky Rise sits at the junction of two magnetic lineation sets, the Japanese and Hawaiian lineations, which can be traced between the bathymetric highs (Figure 26; Larson and Chase 1972; Hilde et al., 1976; Nakanishi et al., 1999). The age of ocean floor trends younger towards the NE from magnetic chron M21 (149 Ma), located at the SW end of Shatsky Rise, to M1 (126 Ma) at the NE end (Figure 26; Nakanishi et al., 1999; using the time scale of Gradstein et al., 2004). Tamu Massif is the largest (~450 x 650 km) and oldest (~145 Ma) volcanic edifice among the three bathymetric highs, and if indeed a single volcano, it may be the largest single volcano on Earth (Sager et al., 2013). It apparently began to form around M21-M20 time (149-147 Ma) (Nakanishi et al., 1999; Nakanishi, this volume). Prior to that time, the Pacific-Izanagi-Farallon triple junction moved northwest relative to the Pacific plate, but at about M21 time, it jumped ~800 kilometers to the location of Tamu Massif (Nakanishi et al., 1999). Basalts cored from Ocean Drilling Program (ODP) Site 1213, on the south flank of Tamu Massif, yielded a radiometric age of 144.6 ±0.8 Ma (Mahoney et al., 2005), which is near that of the magnetic lineations that surround Tamu Massif and consistent with the idea that the volcanic edifice formed near the triple junction (Nakanishi et al., 1999; Sager, 2005). Subsequently, the triple junction drifted northeast along the axis of the rise, and the three

volcanic massifs and Papanin Ridge were created in its path. Although individual massifs may have formed rapidly (Sager and Han, 1993), the span of magnetic anomalies associated with Shatsky Rise implies that it took ~21 million years for the entire plateau to form.

Because the Shatsky Rise region on the Pacific plate has never been close to continental sediment sources, the plateau is covered by a mostly thin layer of pelagic sediments. Sediments deposited on the flanks are typically several hundred meters or less in thickness (Houtz and Ludwig, 1979; Ludwig and Houtz, 1979), whereas sediment caps at the summits are up to ~1 km in thickness (Karp and Prokudin, 1985; Khankishiyeva, 1989; Silter and Brown, 1993; Sager et al., 1999). The sediments atop the rise are mostly composed of Cretaceous pelagic carbonates that were deposited above the calcite compensation depth (Sliter and Brown, 1993).

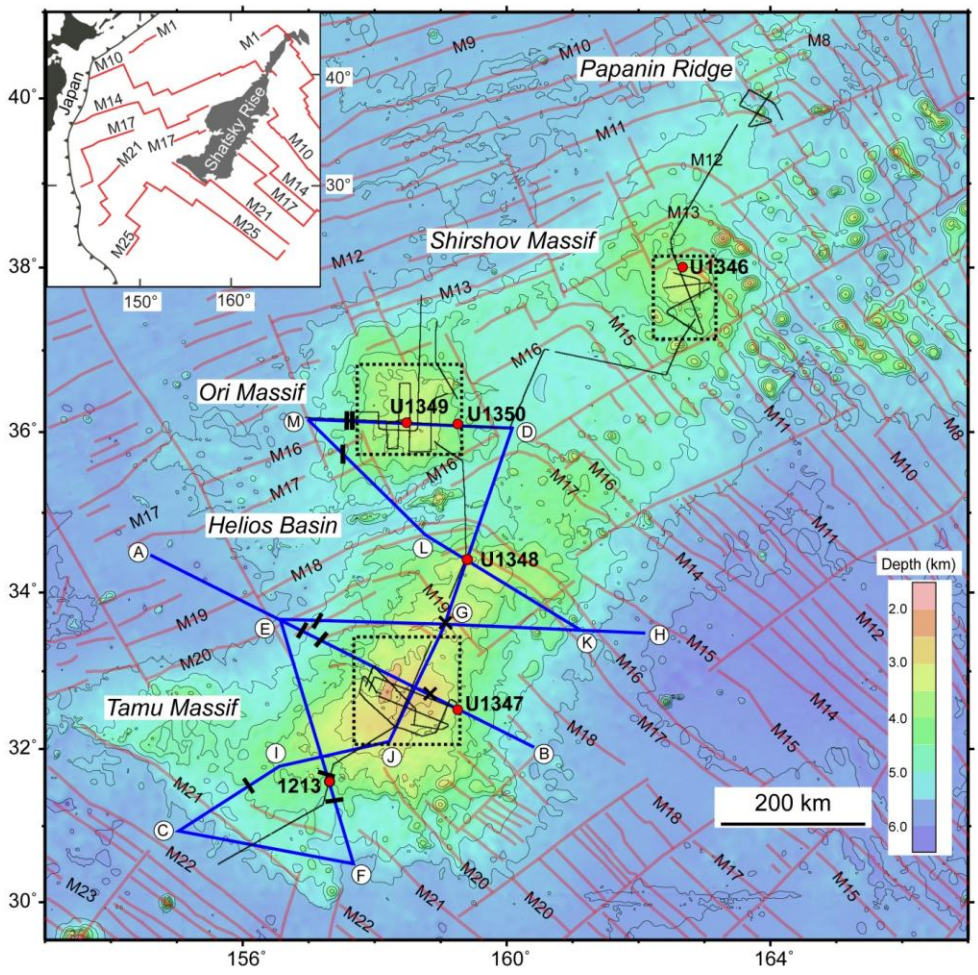

Figure 1. Bathymetry and tectonic map of Shatsky Rise with seismic track lines. Bathymetry is from satellite-predicted depths with 500-m contours (Smith and Sandwell, 1997). Heavy red lines show magnetic lineations with chron numbers labeled for reference (Nakanishi et al., 1999). Heavy blue lines show MCS reflection profiles collected by R/V *Marcus G. Langseth*. Letters next to seismic lines identify end points of MCS profiles for reference. Thin black lines show seismic reflection profiles collected during cruise TN037 (Klaus and Sager, 2002). Filled red circles show locations of the ODP and IODP drill sites mentioned in the text. Inset depicts the location of Shatsky Rise relative to Japan and nearby subduction zones (toothed lines) and the wider magnetic lineation pattern. Heavy black tick marks show the locations of large down-to-basin faults seen on the MCS profiles. The fault strikes are estimated from multibeam bathymetry. Crosses denote the locations of summit calderas. Dashed black boxes denote the summit areas of the three massifs shown in summit basement morphology maps in Figure 15.

Basaltic basement rocks from Shatsky Rise were recovered at ODP Site 1213 (Shipboard Scientific Party, 2001; Koppers et al., 2010) and at IODP sites U1346, U1347, U1349 and U1350 (Sager et al., 2010; 2011) (Figure 2). ODP and IODP coring recovered tholeiitic basalts both as pillow lavas and massive flows up to ~23 m thick. The former are associated with volcanic eruptions at modest effusion rates (Ballard et al., 1979), whereas the latter occur at high effusion rates and are characteristic of flood basalt provinces (Jerram and Widdowson, 2005; Bryan et al., 2010). Often the massive flows and pillow basalts are intercalated (Figure 2). The thickest massive flows are found on Tamu Massif at Sites 1213 and U1347. Massive flows also occur on Ori Massif at Sites U1349 and U1350 and on Shirshov Massif at Site U1346, but they are thinner and less common as the percentage of cored section composed of massive flows decreases from Tamu to Ori and Shirshov massifs. This shift implies a change from high effusion rates at Tamu Massif to lower rates for the smaller edifices, suggesting that an initial burst of magmatic activity was followed by waning igneous output. Interestingly, inter-flow sediments are intercalated with igneous material comprising the basaltic basement at Sites 1213, U1347 and U1350 and thick volcaniclastics make up significant portions of the cored igneous sections at Sites U1348 and U1349. Although some of these volcaniclastic sediments likely occur during the emplacement of lava flows, other such layers may exist because of explosive volcanism at low effusion rates occurring in shallow water (Sager et al., 2010). The Site U1348 section is an example of shallow water explosive volcanism and it implies that volcaniclastic formation is a

significant part of plateau volcanism and that many basement highs consist of this type of material (Sager et al., 2011).

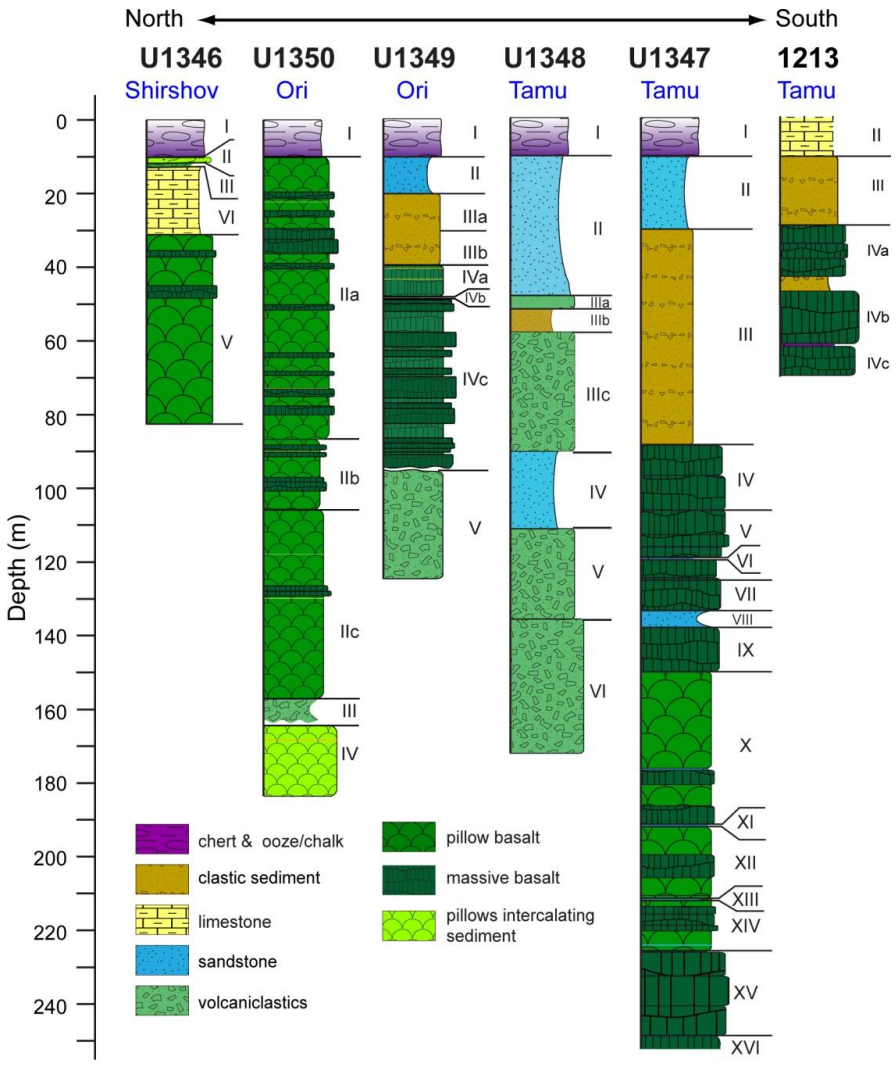

Figure 2. Lithology of cored igneous sections from Shatsky Rise. Sites are arranged in order from northeast (left) to southwest (right) and depths have been shifted to align the tops of the igneous sections. Data from Sites U1346-U1350 are from IODP Expedition 324 (Sager et al., 2010; 2011) whereas data from Site 1213 are from ODP Leg 198 (Shipboard Scientific Party, 2001; Koppers et al., 2010). Site locations are shown in Figure 1. Roman numerals are lithologic unit numbers described in Sager et al. (2010).

2.2.2 Seismic data

Seismic data collected over Shatsky Rise are scarce. Deep seismic refraction studies by Den et al. (1969) and Gettrust et al. (1980) both developed velocity-depth models, but neither was able to record the Moho discontinuity beneath the thickest part of the plateau and the results are somewhat unreliable because of the now-outdated techniques used. Recently, Korenaga and Sager (2012) collected refraction lines across the center of Tamu Massif and reported a maximum crustal thickness of ~30 km. Most seismic reflection data from Shatsky Rise consist of old, low-resolution single channel profiles, which are not useful for investigating the sub-sediment structure. A number of 2- and 3-fold multichannel seismic reflection profiles over Shatsky Rise were acquired on cruise TN037 during 1994 (Klaus and Sager, 2002) and some of these profiles were interpreted in Sager et al. (1999). Although these profiles usually show the interface between sediment and underlying igneous rocks (the "igneous basement" surface), they rarely display significant penetration below the igneous basement owing to the small sound sources used to collect these data. Thus, the TN037 data are useful for tracing igneous basement, but not for examining the sub-basement structure.

2.3 Data and methods

Deep penetrating 2D MCS reflection data were collected from the R/V *Marcus G. Langseth* during cruise MGL1004 in 2010 and cruise MGL1206 in 2012. The seismic source was a 36-airgun array of 6600 cubic inches (108.2 L) volume. The MCS lines were run with a 50-m shot spacing. The receiving array was a single, 6-km-long, 468-

channel streamer with a 12.5-m group interval. With the ship speed used during both cruises, the seismic records had a nominal fold of 59. The CDP interval was 6.25 m and the raw data were sampled at a rate of 2 ms and filtered to a frequency range of 2 to 206 Hz. In total, ~3350 kilometers of MCS reflection lines were acquired (Figure 1). ProMAX (version 2003.19.1) software was used for MCS processing. Processing steps included geometry setup, trace edit, band-pass filter, deconvolution, velocity analysis, normal moveout, stack, time migration and automatic gain control.

The MCS lines crossed one ODP drill site (Site 1213) and four IODP drill sites (Sites U1347, U1348, U1349, and U1350) (Figure 1), providing the opportunity to compare seismic data with cores and logs from the drill sites. This comparison allowed us to document the response of the seismic system to volcanic lithology, providing a basis for geologic interpretation of the seismic lines. Using core and log velocity and density data, synthetic seismograms were generated using Kingdom Suite (version 8.5) seismic interpretation software for comparison with seismic data from the field. Continuous velocity and density data from downhole logs are available only for sites U1347 and U1348, so these are the only sites for which I could calculate synthetic seismograms. The velocity and density data from core samples at other sites are too sparse for reliable synthetic computation. Additionally, since IODP logging occurs with the drill string buried 80-100 m deep within the sediment section, the seafloor response of the logging data is usually not available because that section is shielded by pipe (Sager et al., 2010). Thus, the Expedition 324 logging data for sites U1347 and U1348 do not have the complete velocity and density curves from the seafloor all the way down

to the bottom of the holes. Hence, it is not possible to match synthetics and seismic traces at the seafloor. The clearest signal in the log data occurs at the upper surface of the igneous section, so I used the top of the igneous section, instead of seafloor, to match waveform and amplitude between synthetics and seismic traces.

Kingdom Suite was also used to interpret the MCS reflection profiles. Using standard seismic stratigraphy techniques (Mitchum et al., 1977), seismic horizons were correlated and interpreted in geologic terms. In particular, my focus was on layering within the part of the seismic section thought to represent igneous rock.

Assuming an average velocity for sedimentary layers of 2000 ms^{-1} and a water column velocity of 1500 ms^{-1}, I constructed maps of summit basement depths for the three massifs of Shatsky Rise to learn about volcanic summit morphology. This plot was constructed using the *Langseth* MCS data as well as the seismic reflection profiles from cruise TN037 (Sager et al., 1999).

2.4 Results

The new high quality, deep penetration MCS reflection data generally do a good job at imaging the upper crustal structure and layering of Shatsky Rise. Features within the plateau are visible seismically because of impedance contrasts between layers with differing physical properties. The transition between sediments and igneous rocks frequently generates a high-amplitude reflection that can be interpreted as the top of the igneous basement. The igneous basement surface in my data set is mostly continuous and can be easily recognized because it often gives a strong reflection and is more

irregular than smoother reflections above, interpreted as sediment layers. Within the uppermost igneous basement, layers interpreted as lava flow sequences can be identified by piecewise-continuous and sub-parallel intra-basement reflections. Piecewise-continuous reflections are reflector series that can be connected to infer longer reflectors. Typically individual segments are 5-20 km in length, but can be connected into reflectors several times that length. Another term for such reflectors is "semi-continuous" (e.g. Inoue et al., 2008). In addition, faults can be identified by offsets of strata or lateral terminations or breaks of layering.

2.4.1 Synthetic seismograms

Calculation of synthetic seismograms from core and log velocity and density data shows the correlation of the lithology to the seismic reflections, giving a basis for geologic interpretation. In general, cored igneous sections on Shatsky Rise are short, ranging from ~50-175 m in length, but the core data have high vertical resolution on the order of centimeters. Because of the low frequency of the seismic sound source (6-60 Hz with a peak at ~30 Hz; Vuong et al., this volume), the average wavelength for the sonic waves is tens of meters (~50-100 m assuming 30-60 Hz for a velocity of 4 kms^{-1}), so it is only possible to constrain several wavelengths of the sub-basement seismic record using core and log data.

At Site U1347 on the upper eastern flank of Tamu Massif, the ~160-m igneous section shows that massive basalts are overlain by clastic sediments, intercalated with pillow basalts, and interbedded with inter-flow sediments (Figure 3). The interface

between the sediments and igneous basement (~90 m depth in Figure 3) shows an abrupt rise in both velocity and density, generating a strong reflection identified as the top of the igneous basement.

Inter-flow sediment layers apparently account for several other reflections. Expedition 324 shipboard scientists described four significant sediment layers in the section (Roman numerals in Figure 3), with three of them being ~4-5 m in thickness (Sager et al., 2010). Only one of these layers was recovered well and thus appears prominently in the graphic lithology (at 135 m depth in Figure 3). Thicknesses for the other three sediment layers were inferred from the log data, which show four prominent low velocity-density horizons at ~115 m, 130 m, 180 m, and 200 m (Sager et al., 2010). The upper three lows are likely a result of sediment layers. The lowermost low is broader than the sediment layer (Unit XIII in Figure 3) and probably occurs because of higher porosity pillow flows and inter-flow debris. Impedance contrasts caused by these low velocity-density zones appear to cause the second positive signal peak (at ~130 m in Figure 3) and the underlying broad negative (170-210 m). The lowest positive reflection occurs at the transition between pillow flows and thick massive flows, apparently caused by the slight increase in velocity and consistently high velocity and density values of the massive flows. At ~190 m depth, there is a mismatch between the synthetic traces, which show a strong positive peak, and the field data, which do not. Here it appears that a narrow spike in the velocity and density log data generate a reflector in the synthetic data that is not matched in the field data. This mismatch may be a result of the difference in vertical resolution of the two data types.

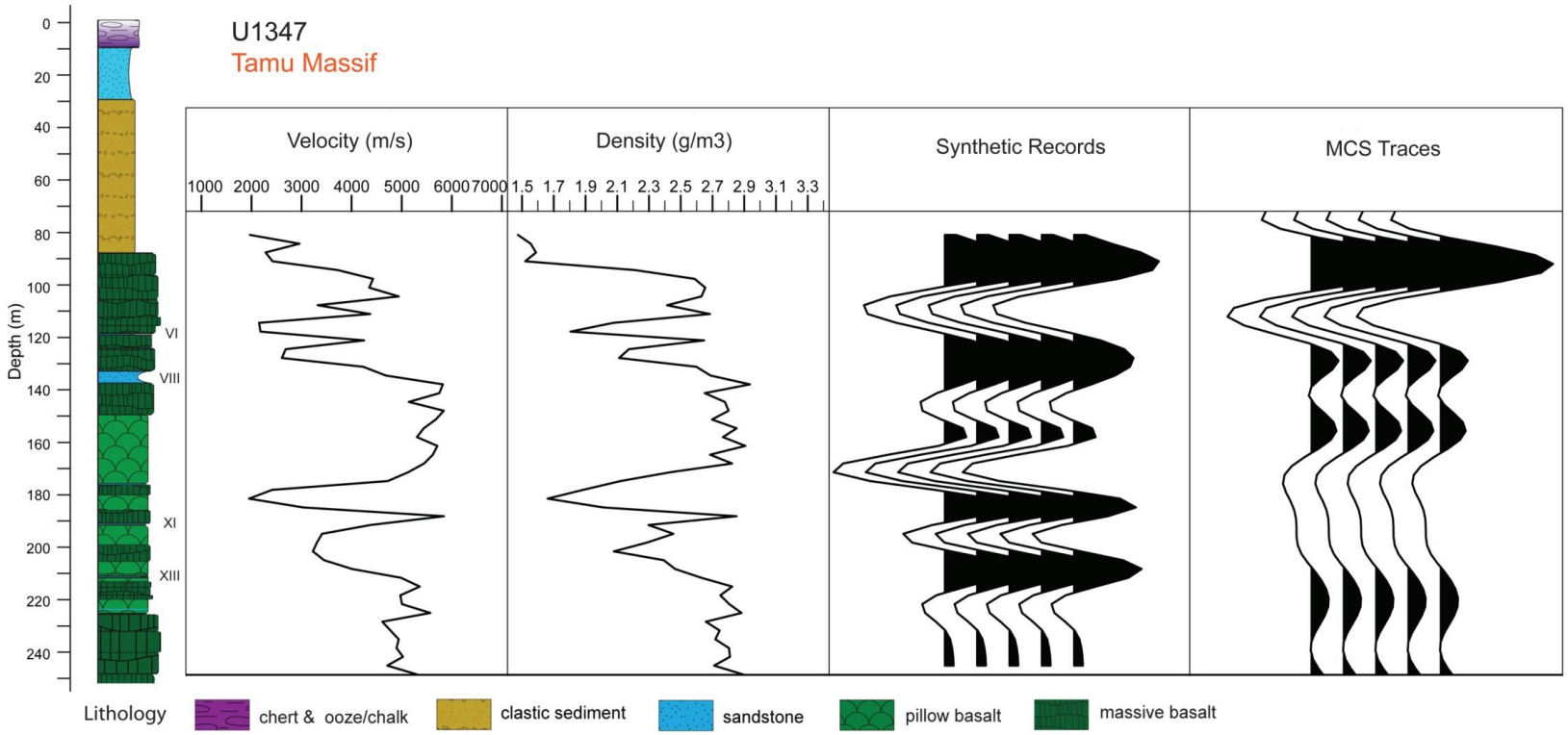

Figure 3. Synthetic seismogram of IODP Site U1347. The left panel shows lithologic description (Sager et al., 2010) and columns have been shifted in depth to align the top of the igneous sections with logging data. Roman numerals denote sediment layers discussed in text. The middle two panels show velocity (ms^{-1}) and density (gcm^{-3}) curves from logging data (Sager et al., 2010). The right two panels show synthetic records and actual MCS traces from field data. Synthetic and MCS traces are matched at the top of the igneous section.

The synthetic seismogram from Site U1348 (northern Tamu Massif) shows a variety of different sediments that exhibit multiple changes in velocity and density resulting in many reflections in the synthetic section (Figure 4). This section also shows a strong reflector at the top of the igneous section owing to an abrupt rise in velocity and density. Within the section, there is not always a clear correspondence between lithologic layers and seismic response. Although some of the modeled reflections obviously follow changes in lithology (e.g., the strong reflector at the base of the clastic sediment layer at ~50-m depth in Figure 4), other reflections occur from velocity and density changes within a layer classified as a single lithology. Thus, in volcaniclastic sections the correlation between lithology and seismic layering can be complex.

In enlargements of MCS profile sections crossing Sites 1213, U1347, U1348, U1349 and U1350 (Figure 5), the high amplitude basement reflector can be easily identified because of its strong amplitude and because it often separates rough basement from smoother sediment layers. Basement reflectors are continuous and parallel to the seafloor. Intra-basement reflectors are not usually as continuous as the basement reflector. Although some shallower intra-basement reflectors are relatively continuous and parallel to the basement surface, most are rugged, irregular, and show scattering. Intra-basement reflectors appear to be piecewise-continuous and the pattern can be traced for longer distances. In general, the intra-basement reflectors are sub-parallel to the basement surface.

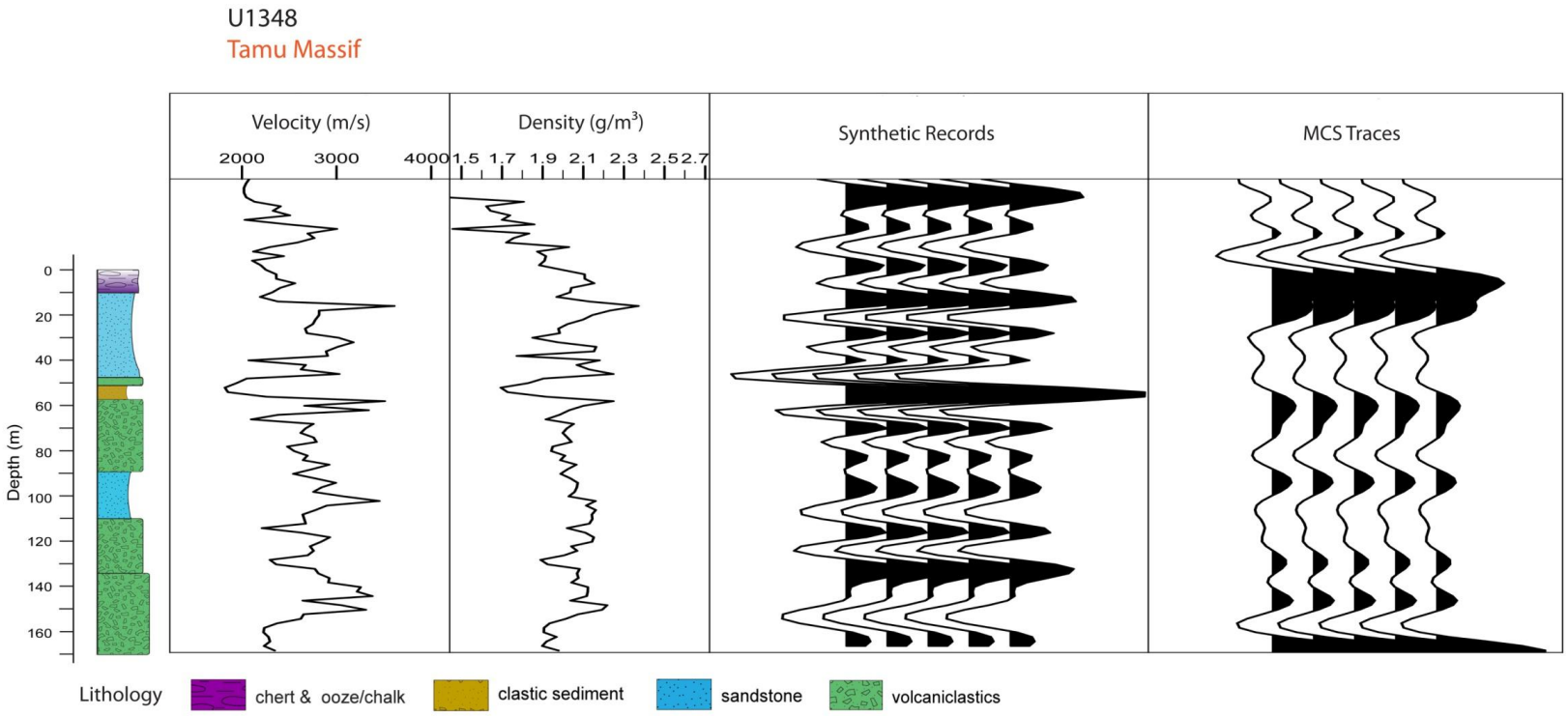

Figure 4. Synthetic seismogram of IODP Site U1348. Plot conventions as in Figure 3.

No matter whether the drill sites are located at the summits or on the flanks of Shatsky Rise (Figure 1), all the crossing short seismic sections (Figure 5) shows that the slopes of seafloor are shallow (<0.5 °). Although it is not possible to measure the true slope from widely-spaced 2D seismic lines because profile orientation relative to the maximum dip axis is unknown, the apparent slope is so shallow that it the apparent dip is not greatly different from actual dip. The slope indicator in Figure 5 and other seismic sections (calculated from the vertical exaggeration using 1500 ms-1) is strictly valid only for the seafloor, but where underlying layers are parallel to each other (i.e. layers have constant thicknesses) their velocity gradients in depth do not change the apparent slope, which means that the slopes of the sub-seafloor layers are the same as the slope of the seafloor. This applies to many of the Shatsky Rise profiles because basement and intra-basement reflectors are often parallel or sub-parallel to the seafloor (Figure 5). Therefore, the slopes of basement and intra-basement reflectors would be nearly identical to the slope of the seafloor.

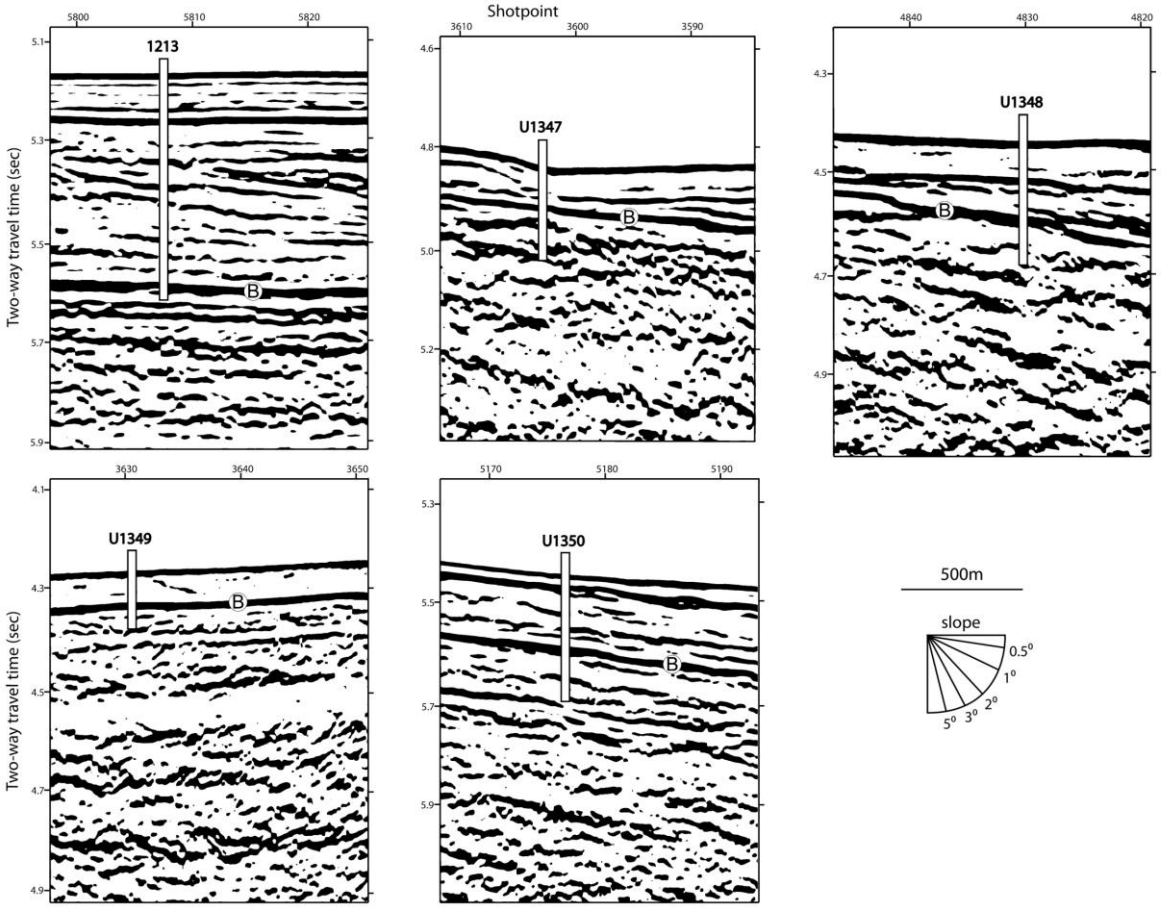

Figure 5. Enlargements of seismic sections across drill Sites 1213, U1347, U1348, U1349 and U1350. The igneous basement surface is labeled in circled letter "B". The vertical white bars with black border show the positions and depths of the drill sites. Slope indicator applies to the seafloor and is calculated from vertical exaggeration of 22:1 using water velocity of 1500 ms^{-1}.

2.4.2 Tamu Massif

Line A-B (Figure 6) is a complete profile across the SW-NE axis of Tamu Massif. It displays the shallowest parts of Tamu Massif and shows many of its characteristic features. Beneath a thin blanket of sediment (except at the summit), the igneous basement reflector is easily traced across the plateau. This reflector exhibits a shallow slope, starting from ~1°-1.5° on the upper flanks to <0.5° on the distal lower flanks. The volcanic profile is symmetric across a rounded basement summit at shot point (SP) 4400. Numerous intra-basement reflectors are observed 0.5-2.0 s in two-way travel time (TWTT) into the igneous pile (1000-4000 m sub-basement depth assuming a sonic velocity of 4000 ms^{-1}). Individual intra-basement reflectors are piecewise-continuous and can be traced continuously up to tens of kilometers in length, but the pattern continues hundreds of kilometers down the flanks. These reflectors are generally sub-parallel and follow the shallow slopes down the flanks, apparently imaging flow packages emanating from the volcanic center at SP 4400. Intra-basement reflectors continue the symmetric, domed shape of the eruptive center at depth, implying a long-term stability in relative location.

To illustrate intra-basement reflectors, two enlargements from Line A-B are shown in Figure 7. Figure 7a, near the Tamu Massif summit, shows that the intra-basement reflectors are variable in continuity. Many can be traced for a few kilometers and some for tens of kilometers or more. Often several reflectors can be connected as a single horizon (i.e., piecewise-continuous). Many intra-basement reflectors are parallel to one another and to the basement surface, whereas some reflectors depart from parallel

and show significant topography, consistent with observations of subaerial lava flows, which can display significant roughness (e.g., Macdonald, 1972). Figure 7b, from the lower west flank, exhibits significant variability of intra-basement reflectors in topography, implying complex flow geometries. In some places, the reflectors are horizontal, implying ponded flows. A notable feature of this section of the profile is the existence of segments of steeper intra-basement reflectors. These reflectors could be similar to the "foreset" beds of Planke et al., (2000) and Spitzer et al. (2008), who suggested that they are caused by volcaniclastics deposited at the toe of a subaerial lava delta.

A depression is observed at the top of the summit at SP 4400 on Line A-B (Figure 1; Figure 7a). It appears to be a graben and measures ~3 km across and ~55 m in depth (assuming a velocity of 1500 ms^{-1}), appearing similar to summit rift zone grabens or calderas on other large volcanoes (e.g. Dieterich, 1988), consistent with the idea that the summit is the volcanic center. A number of secondary cones are observed on Line A-B, including a large summit ridge (Toronto Ridge) at SP 5700. These cones have steeper slopes (~5 °) than the surrounding volcanic flanks. Large down-to-the-basin normal faults are observed on the western flank at SP 7600 (Figure 7b) and SP 8400, with ~0.2-0.5 s TWTT of offset (~150-375m assuming a velocity of 1500 ms^{-1}).

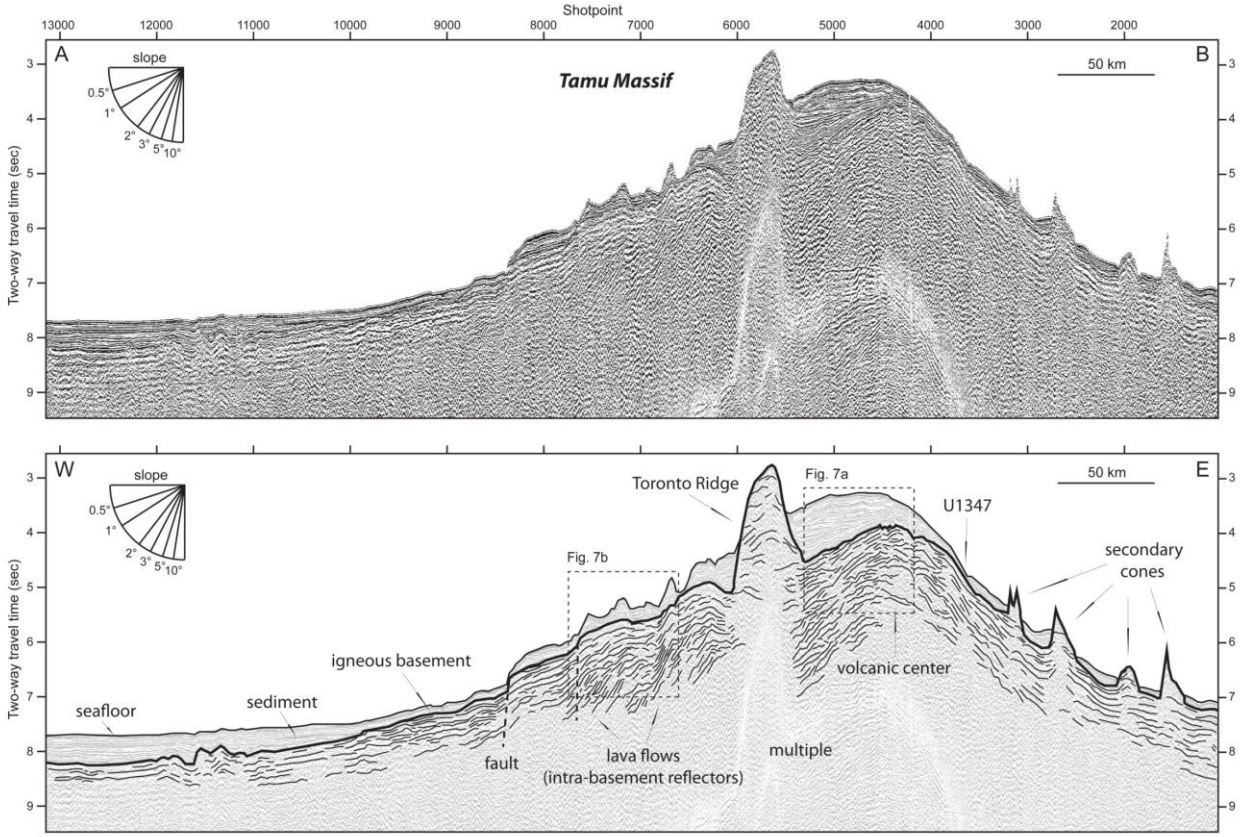

Figure 6. MCS reflection profile of Line A-B, modified from Sager et al. (2013). Top panel shows uninterpreted MCS data whereas bottom panel shows seismic interpretations. The heavy black horizon represents the sediment-basalt interface (igneous basement). Thin dark lines represent selected intra-basement reflectors (lava flows) (Note: for clarity, not all intra-basement reflectors are highlighted in this and other large scale figures). Dashed lines represent faults. The arrow labeled "U1347" shows the position of that drill site. Slope indicator refers to the seafloor (vertical exaggeration = 37:1). Dashed boxes highlight the enlarged segments shown in Figure 7.

a

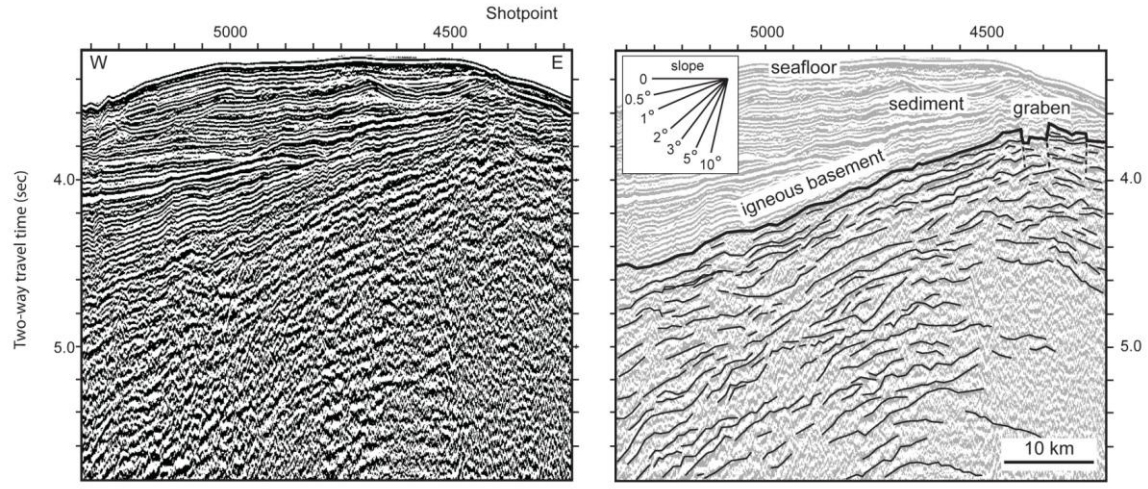

b

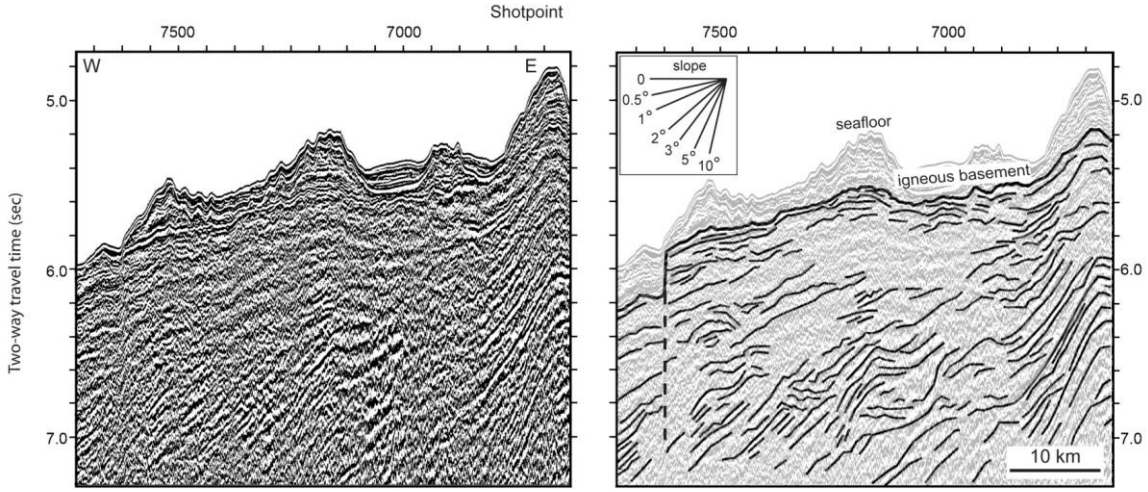

Figure 7. Segments of MCS Line A-B, illustrating intra-basement reflectors (section a modified from Sager et al., 2013). Uninterpreted data shown in left panel; interpretation in right panel. Slope indicator refers to the seafloor (vertical exaggeration = 25:1). Dark lines represent intra-basement reflectors. Dashed lines represent faults. Locations shown in Figure 6.

Other MCS profiles across the axis of Tamu Massif present similar characteristics as Line A-B. For example, Lines E-F (Figure 8), and E-H (Figure 9) also show the rounded, symmetric, shallow-slope across-axis profile of the volcano. In all of these profiles, intra-basement reflectors are observed to dip away from the Tamu Massif summit. The near-summit enlargement of Line E-H (Figure 10) shows that most intra-basement reflectors dip gently to the basin and are sub-parallel. The summit reflectors are nearly horizontal and not as continuous as those on the flank, which is similar to the observations on Line A-B in Figure 7a. Line E-H also exhibits steeper segments (~3 °-5 °) of dipping reflectors like those observed on the western flank on Line A-B (Figure 7b), with an appearance similar to sedimentary clinoform layers (e.g., Spitzer et al., 2008). Analogous steeper reflectors are also noted on the other lines that cross the axis of Tamu Massif (Line E-F in Figure 8).

The depression observed atop the basement summit on Line E-H (Figure 10) appears to be a graben. It is ~5 km across and ~170 m in depth (assuming a velocity of 1500 ms^{-1}), similar to that on Line A-B (Figure 7a), implying that this feature is common on the summit of the volcano. The depression on Line E-H occurs to the NE of that on Line A-B (Figure 1), implying that axial rifting follows the SW-NE elongated shape of Tamu Massif.

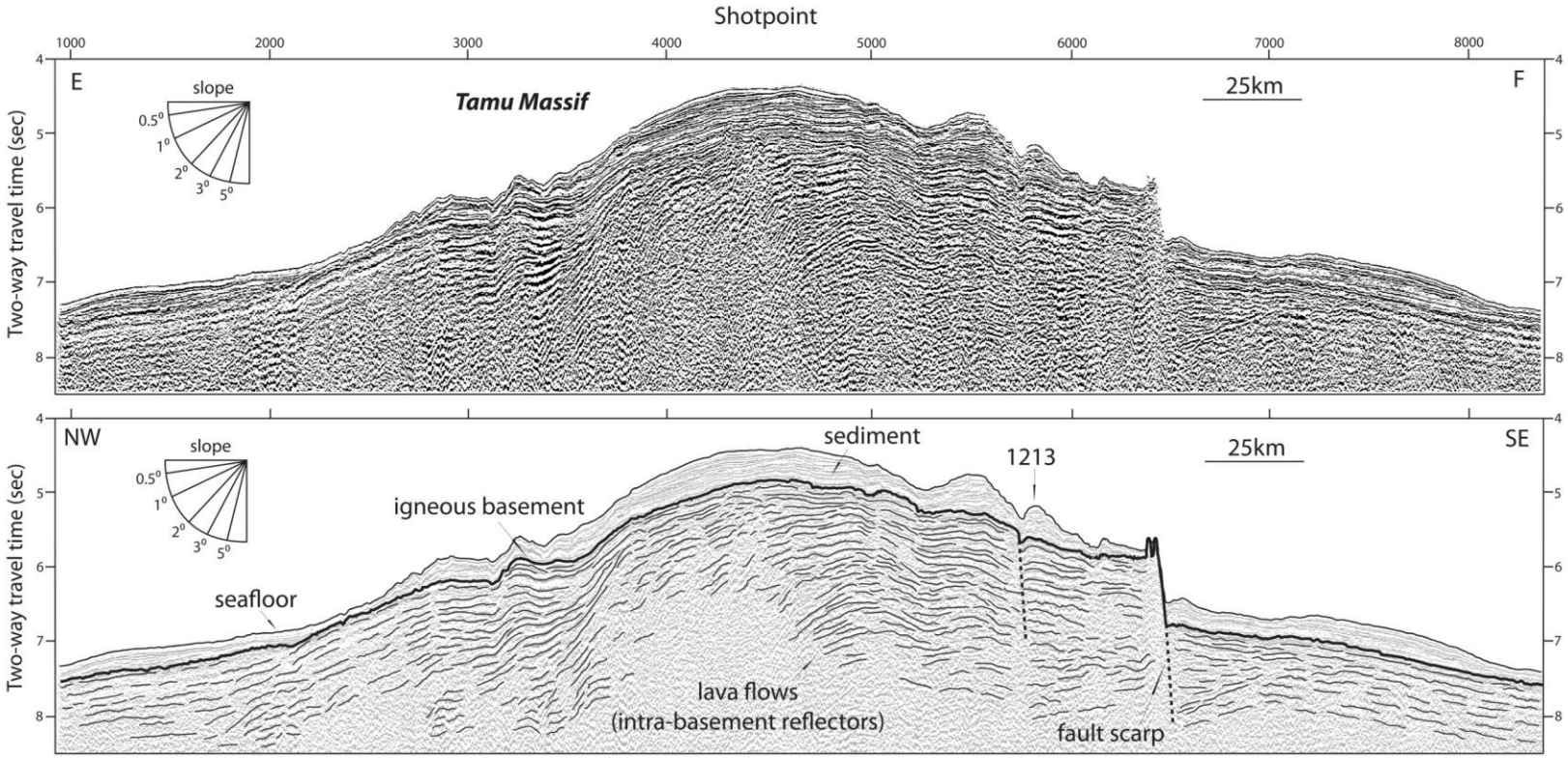

Figure 8. MCS reflection profile of Line E-F. Vertical exaggeration = 22:1. Other plot conventions as in Figure 6.

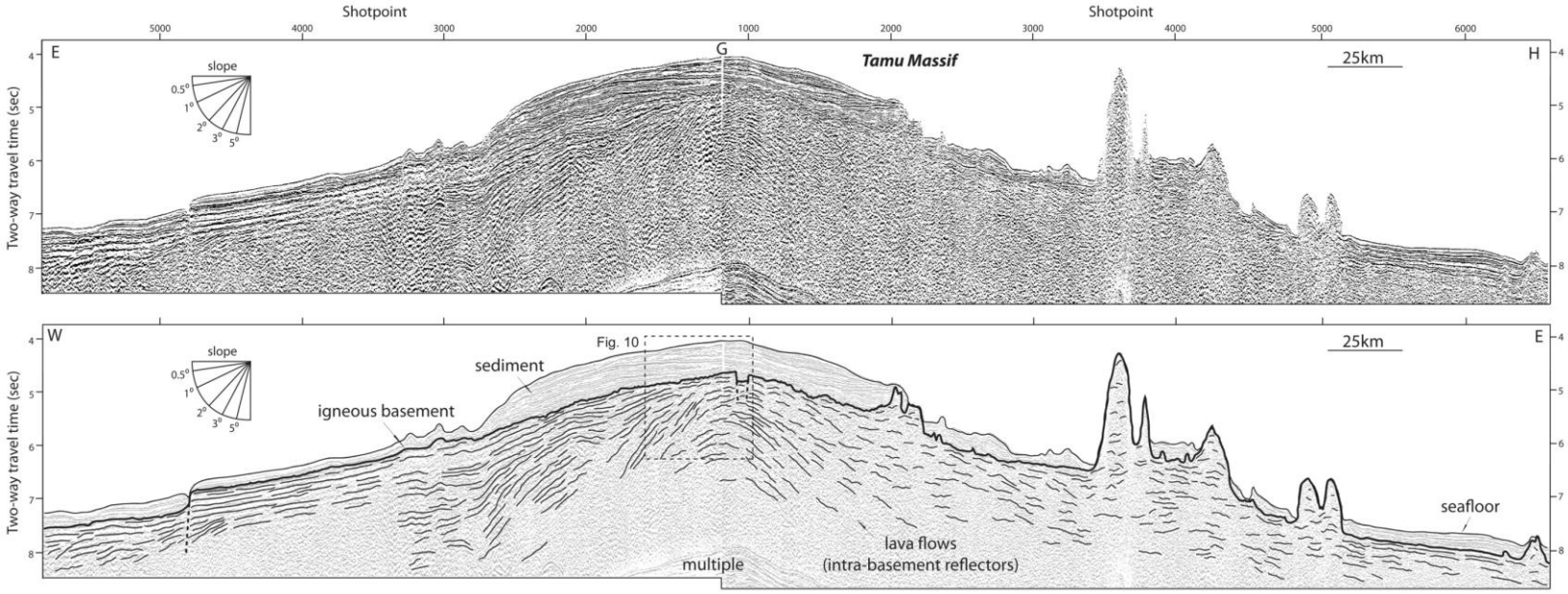

Figure 9. MCS reflection profile of Line E-H. Vertical exaggeration = 22:1. Boxed area is enlarged in Figure 10. Other plot conventions as in Figure 6.

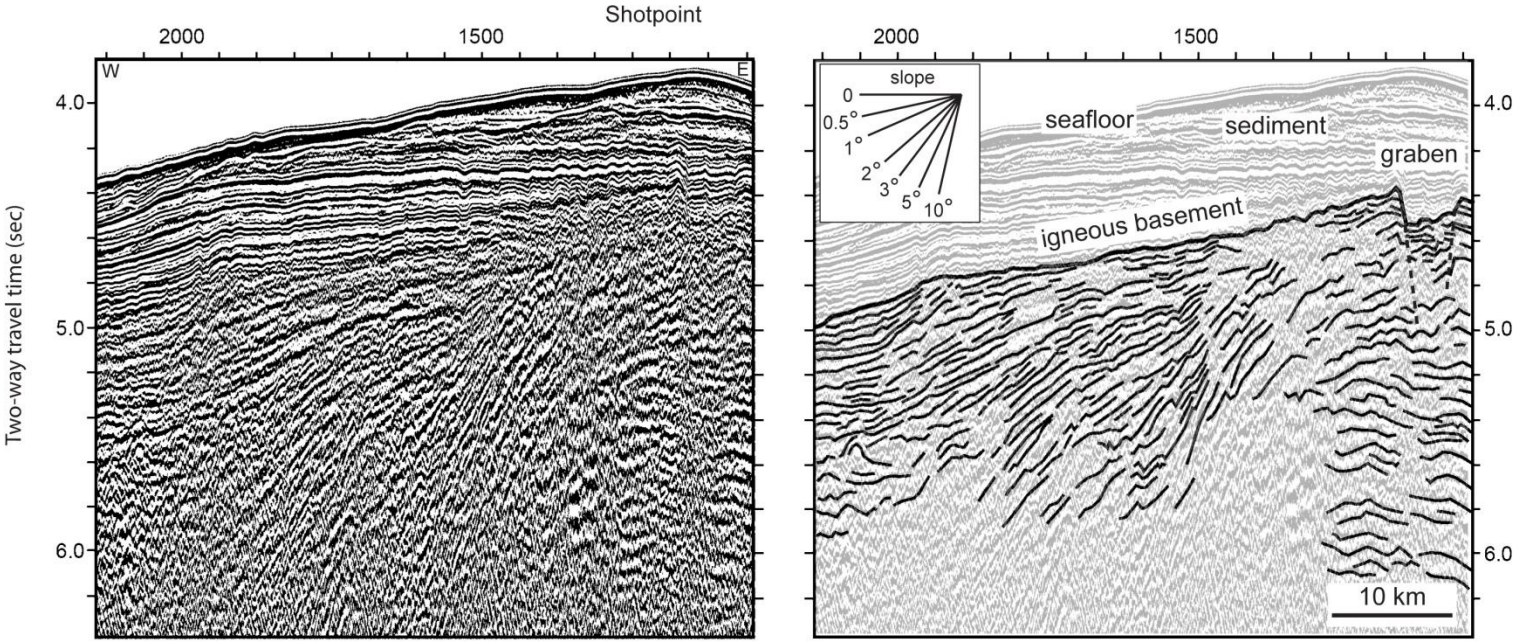

Figure 10. Detail of a segment of MCS Line E-H (dashed box, Figure 9), illustrating intra-basement reflectors. Plot conventions as in Figure 7.

Line L-K (Figure 11) also crosses the axis of Tamu Massif, but at the northeastern end. Although Line L-K shows a rounded profile like Line A-B (Figure 6), it exhibits greater structural complexity. Dips of intra-basement reflectors show at least two major eruptive centers (SP 3900 and SP 4700) and numerous small cones. The implication is that this part of Tamu Massif had a slightly more complex arrangement of volcanic centers than the center of the edifice. This line crosses Site U1348, which cored a volcaniclastic section, so the cone at SP 4700 is likely made up of volcanclastics rather than lava flows.

Lines C-I, I-J, J-G, and G-D, form a composite profile along the axis of Tamu Massif (Figure 12). Although intra-basement reflectors on lines C-I and G-D, at the south and north ends of the massif, respectively, are uniform and descend toward the basin like those noted on across-axis profiles, the basement reflectors on lines I-J and J-G at the summit are sub-horizontal and undulatory. In contrast to the across-axis lines, which show a narrow eruptive axis, the along-axis profiles show wide, shallow undulations of intra-basement reflectors as could be expected from a profile paralleling elongated volcanic centers aligned along the axis. A notable feature of this composite profile is that they show reflectors clearly to depths of >2 s TWTT. This is equivalent to a depth of ~4 km (assuming a velocity of 4 kms^{-1} for basement), and is below the level of the surrounding abyssal seafloor, implying a remarkable structural consistency of the massif as it formed. In addition, a summit depression, again interpreted as a graben, is seen at the intersections of lines J-G and G-D. It is ~ 15 km across and ~100 m in depth (assuming a velocity of 1500 ms^{-1}).

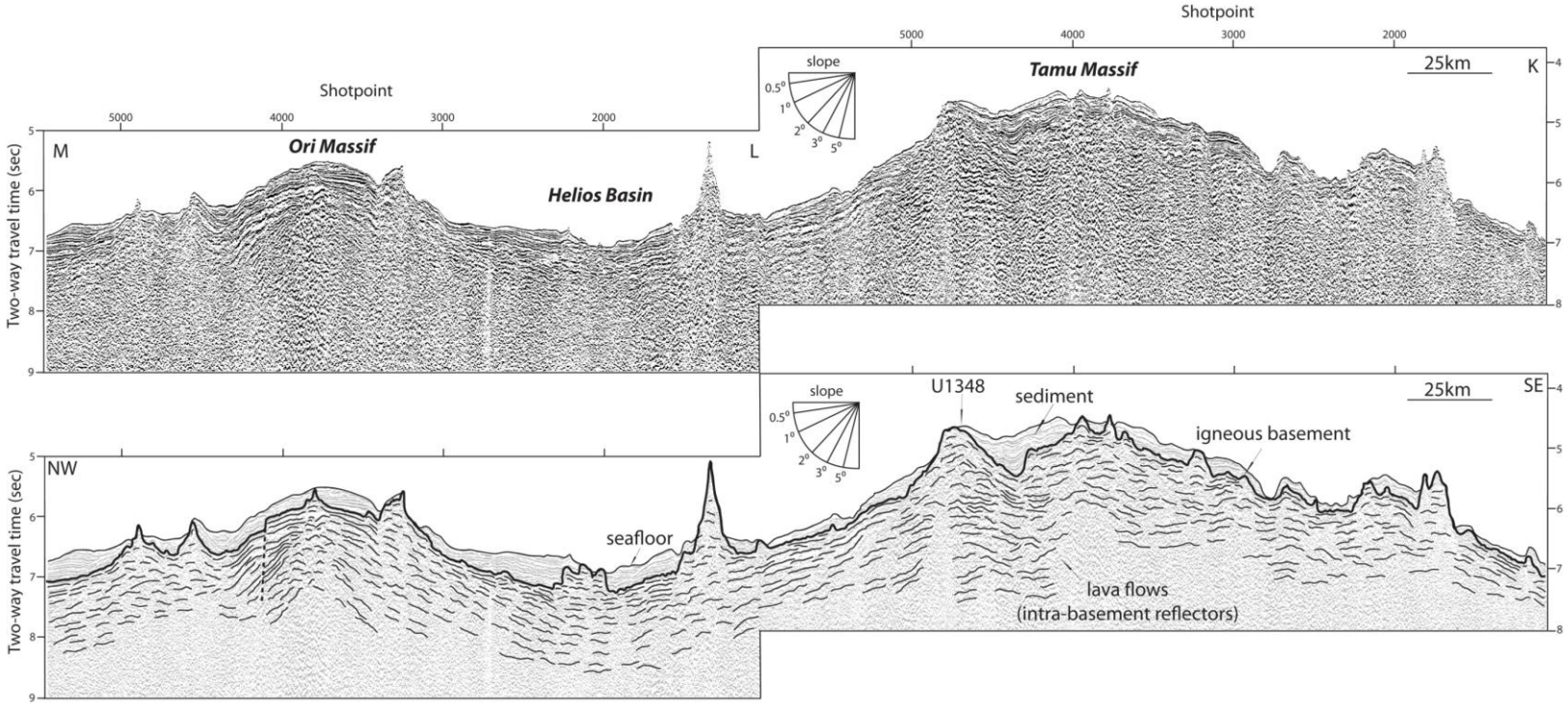

Figure 11. MCS reflection profile of Line M-K. Vertical exaggeration = 22:1. Other plot conventions as in Figure 6.

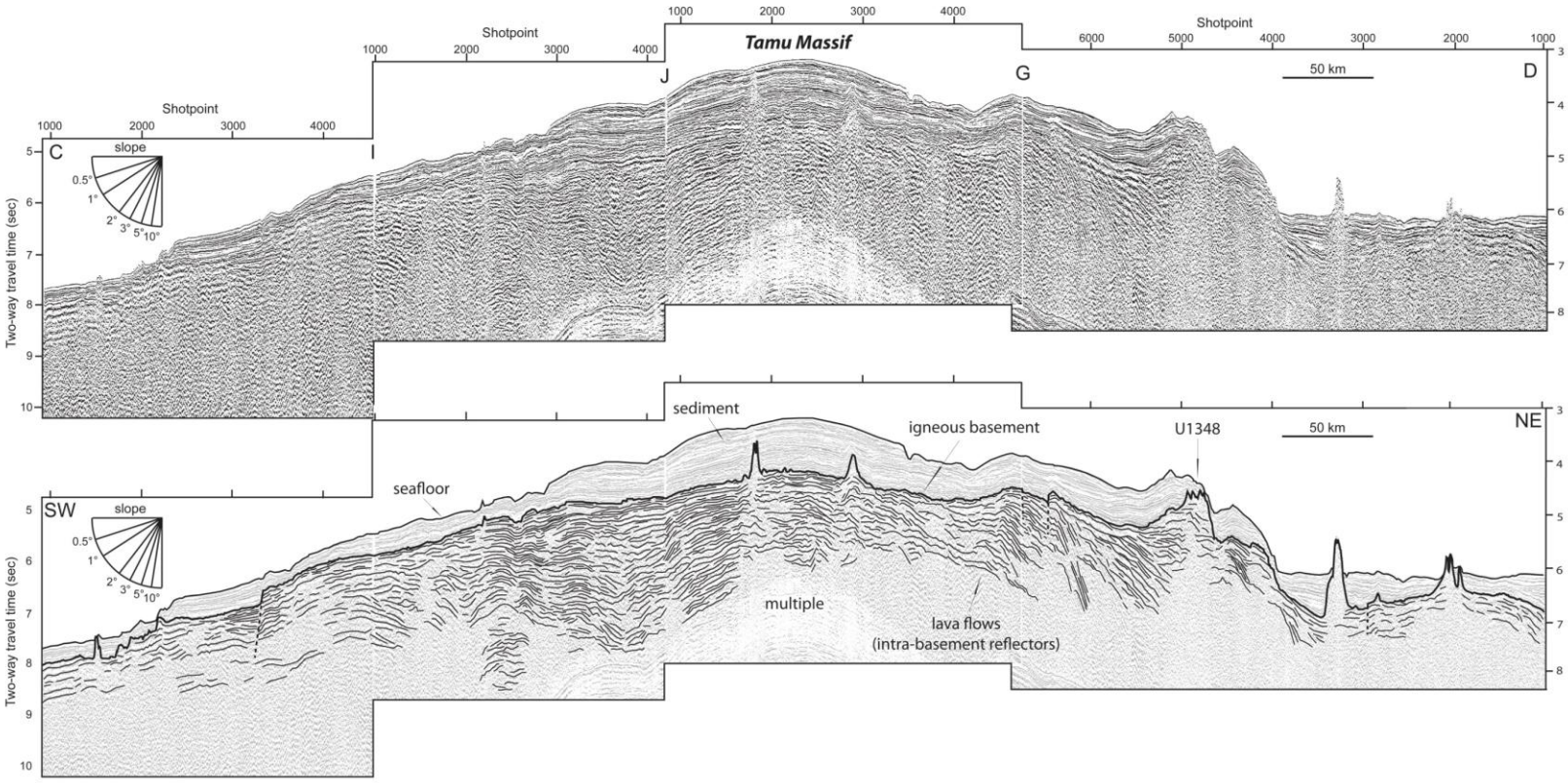

Figure 12. MCS reflection profile of Line C-D, modified from Sager et al., 2013. Plot conventions as in Figure 6.

For both across-axis and along-axis profiles, secondary cones like those observed on Line A-B (Figure 6) occur on many MCS lines (e.g. Lines E-H (Figure 9) and L-K (Figure 11)) and buried cones appear on Line J-G (Figure 12) beneath the thick summit sediment cap. Most are 10-20 km in width and 0.5-1.0 km in height. A few are larger, such as the large ridge atop Tamu Massif (Toronto Ridge) (Figure 6) and the large cone drilled at Site U1348 (Figures 11, 12). Some are rounded and some have sharp peaks and most have flank slopes >5 °. Similar features are seen on the TN037 seismic data (Klaus and Sager, 2002) and in bathymetry data. Line C-F (Figure 13), crossing a low, distal flank salient on southeast side of Tamu Massif, has many small cones of different shapes and sizes. On lines L-K (Figure 11) and G-D (Figure 12), Site U1348 sits atop a large basement high that appears to be a volcaniclastic cone, formed by explosive volcanism inferred from volcaniclastic cores recovered at the drill site (Sager et al., 2010).

Similar to the normal faults on Line A-B (Figure 6), large down-to-basin normal faults on the massif flanks are also noted at many locations on Tamu Massif: Lines E-F (Figure 8), E-H (Figure 9) and C-I (Figure 12). The fault at SP 6500 on Line E-F (Figure 8) is especially notable owing to its large throw (~1.0 s in TWTT = ~750 m assuming velocity of 1500 ms-1). This fault is also topped by a small volcanic cone, imaged by multibeam bathymetry, where Line E-F crosses the fault, suggesting that this fault can be related to secondary volcanism. Although the deeper reflectors on the basinward side of the fault on Line E-F bend downward toward the fault, faults elsewhere show simple offset of basement and intra-basement reflectors on most lines.

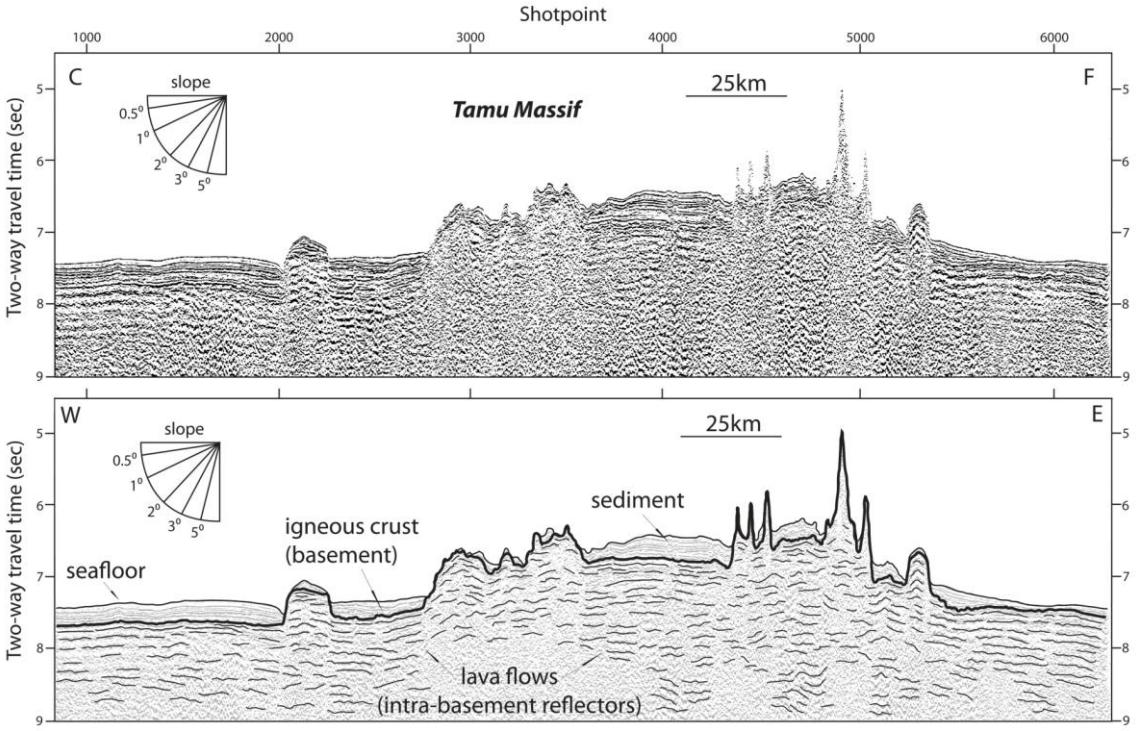

Figure 13. MCS reflection profile of Line C-F. Vertical exaggeration = 22:1. Other plot conventions as in Figure 6.

2.4.3 Helios Basin

Helios Basin separates Tamu and Ori Massifs and displays a rectangular and elongated shape (Figure 1). It contains several linear seamounts near its center, following the basin axis (Sager et al., 1999). Magnetic lineations also trend along the basin axis (Figure 1), so a hypothesis for the basin formation is the splitting of Tamu and Ori massifs by rifting (Sager et al., 1999; Nakanishi et al., 1999). MCS Line M-K (Figure 11), which crosses western Helios Basin, shows that the volcanic basement of Tamu and Ori massifs on the basin edges is not cut by large normal faults as would be

expected for a rift basin. Intra-basement reflectors on the Tamu and Ori flanks trend downhill into the basin and meet at the center against the axial volcanic ridge. Line G-D (Figure 12) crosses the east end of Helios Basin near the northward extension of Tamu Massif. It also shows descending basement and intra-basement reflectors from adjacent massifs to the bottom of the basin. Few normal faults are seen on this line. A volcanic ridge occurs at the center of a dome-like bulge in the basement surface. Intra-basement reflectors dip outward from the volcanic ridge, implying that it was a volcanic center. Thus, these observations imply that Helios Basin was not formed by the rifting apart of Tamu and Ori massifs. Instead the basin apparently formed by seafloor creation during a gap between the construction of the two volcanic centers.

2.4.4 Ori Massif

Ori Massif is the second largest and likely second oldest dome-like volcanic edifice within Shatsky Rise. MCS Line M-D (Figure 14) crosses this entire edifice in the W-E direction, whereas Line M-L (Figure 11) crosses the west side of the volcano. These profiles give a similar structural picture to Tamu Massif, showing Ori Massif to be also a rounded, symmetric volcano with low flank slopes. Intra-basement reflectors mostly dip outward from the summit of the volcano, implying that Ori Massif is also a large central volcano. In comparison to Tamu Massif, Ori Massif has somewhat rougher basement topography. Rough basement shape results from down-to-basin normal faults and secondary cones as well as short-wavelength basement topography. On Line M-D (Figure 14), at the summit of Ori Massif, the shallowest basement is a ridge (at SP 3700)

that was cored by IODP Site U1349 (Sager et al., 2010). In addition, Line M-L (Figure 11) shows similar features including rough basement caused by secondary cones and down-to-basin faults. A volcanic center is imaged at SP 3800 (Figure 11). It displays a pattern of intra-basement reflectors dipping outward from the center. The center of the pattern is roughly beneath the highest point of the basement surface, implying that the volcanic center did not move laterally as it built. Moreover, the basement summit on this line is topped by a small volcanic cone, which is likely a late-stage eruption product.

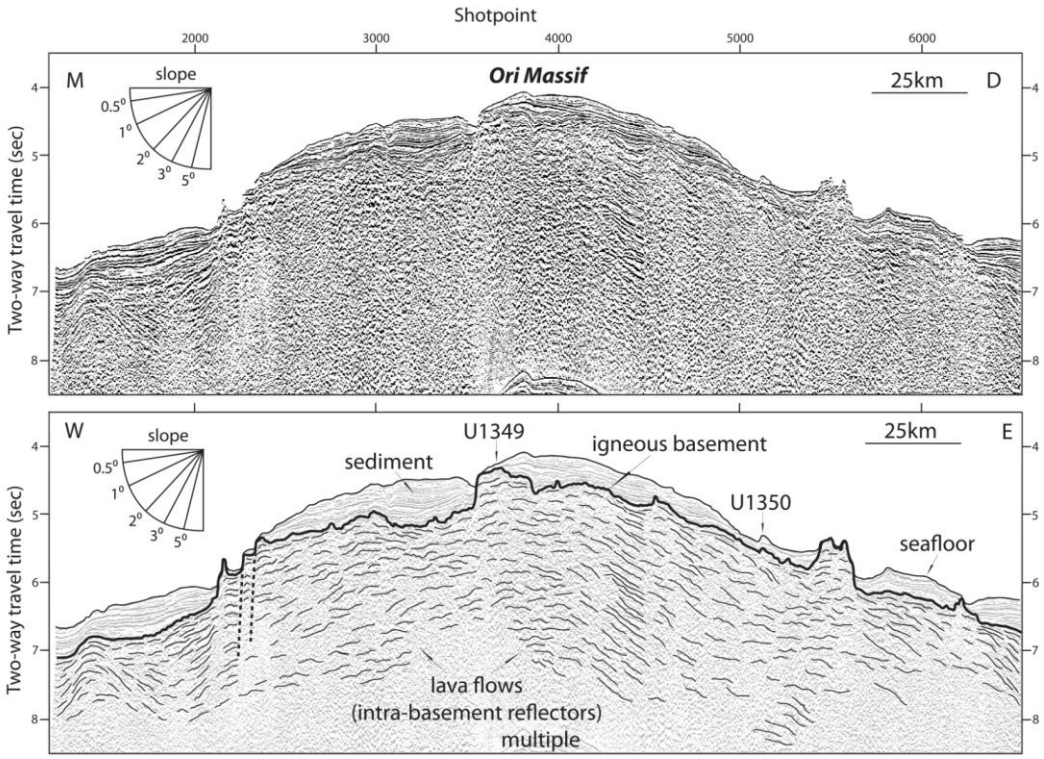

Figure 14. MCS reflection profile of Line M-D. Vertical exaggeration = 22:1. Other plot conventions as in Figure 6.

2.4.5 Massif summit basement morphology

Although the seismic lines are sparse, limiting the resolution of summit basement features and potentially missing small features, the data nonetheless reveal the broad-scale summit structure of the three massifs (Figure 15). The Tamu Massif summit has two large basement peaks that imply two volcanic centers. As stated in a previous section, the eastern peak is rounded and has low slopes and appears to be the center of the volcano shield-building stage. Toronto Ridge, on the west side of the summit, is tall (~1 km height), linear, and has steeper slopes than the shield stage (~5 °compared to <1 °). The Tamu Massif summit map also shows several small, buried cones. These are likely secondary cones such as those that dot the volcano flanks. Moreover, although Line A-B could be interpreted to show a basin between the two Tamu basement peaks, the Tamu Massif summit map shows that there is no closed basin. A remarkable feature of the Tamu Massif summit is that despite the fact that shallow water sediments have been recovered around the summit (Sager et al., 1999; Sager et al., 2010), no evidence of erosional truncation or flattening is observed around the summit in seismic sections.

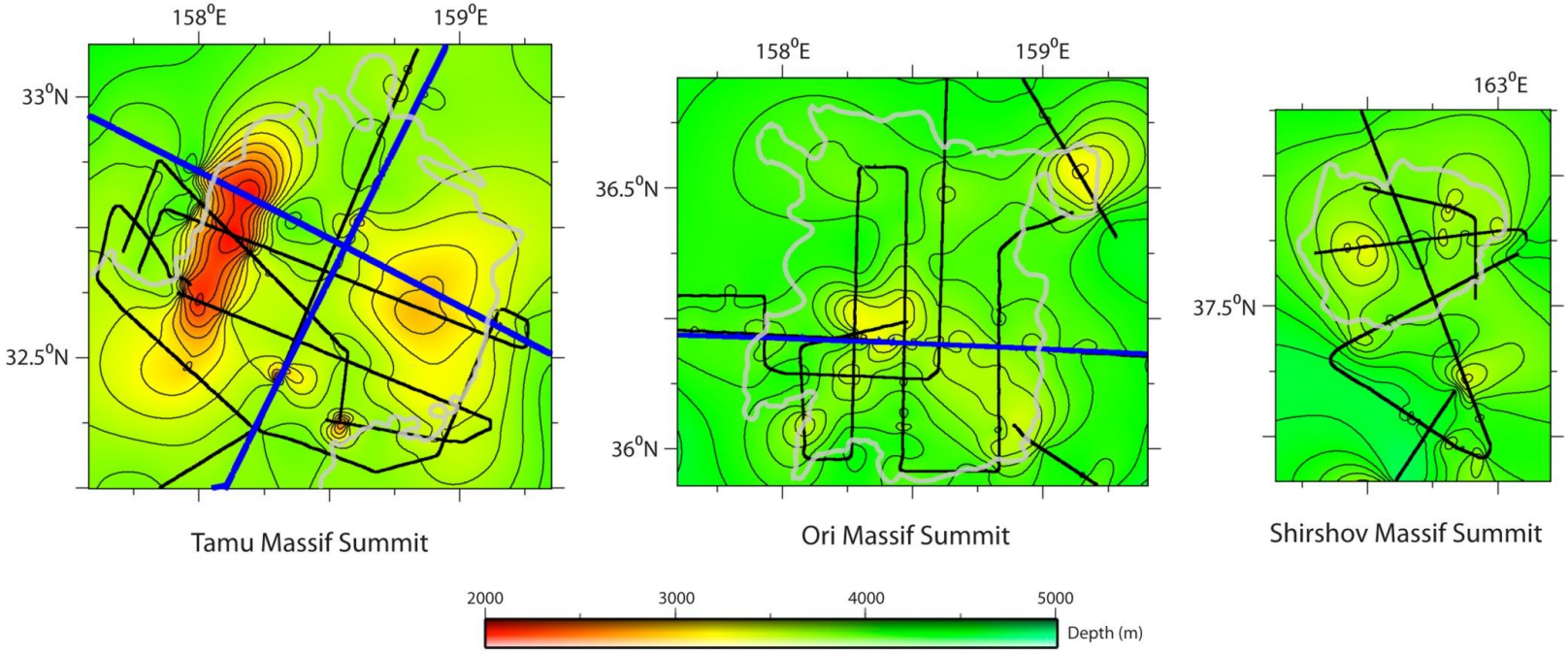

Figure 15. Summit basement morphology maps. Isobaths are gridded from the combined seismic dataset of R/V *Marcus G. Langseth* MCS data and seismic data from cruise TN037 (Klaus and Sager, 2002). The average velocity of the sediments and water column were assumed to be 2000 ms^{-1} and 1500 ms^{-1}, respectively. Basement contours are shown at 200-m intervals. Locations and extents of these maps are shown in Figure 1. Heavy blue and black lines show the seismic lines used to determine basement depths (dark blue = Marcus G. Langseth; black = TN037). Heavy gray contours show the 3000-m depth contour (left) and 3500-m depth contour (middle, right) from satellite-derived bathymetry data (Smith and Sandwell, 1997) for positional reference.

The Ori Massif summit has two large basement peaks. One basement peak occurs at the center and corresponds to the summit ridge (<0.5 km height) seen on line M-D at SP 3700 (Figure 14). This peak has a nearly flat top and contains nearly horizontal intra-basement reflectors. Cruise TN037 seismic data show that the other large basement peak on the NE side of the Ori summit is a rounded ridge (~1 km height and ~5 °slope) (Sager et al., 1999), similar to Toronto Ridge on Tamu Massif. As with Tamu Massif, cores from Site U1349 at the Ori Massif summit indicate shallow water, but again seismic sections show no unequivocal evidence of erosion or truncation.

The Shirshov Massif summit shows one larger basement peak on the west side of the summit platform and three smaller cones on the east side of the summit. Cruise TN037 seismic data show that the large basement peak has an overall rounded shape with two small secondary cones sitting atop it (Sager et al., 1999). The buried cones on the east side appear similar to other secondary cones on Tamu and Ori Massifs. Although much of the Shirshov Massif summit basement surface appears flat (Sager et al., 1999), detailed examination shows that the basement surface is undulating and shows no evidence of truncation. Thus, it does not appear to be an erosional feature. Furthermore, the summit cones are apparently constructional features, not erosional remnants. Therefore, like Tamu and Ori massifs, the summit of Shirshov Massif does not appear eroded and summit cones appear to be secondary features.

2.5 Discussion

2.5.1 Geologic interpretation of intra-basement reflectors

Based on the synthetic seismograms, reflections occur where large-scale changes in density and sonic velocity occur. In the sections, these are usually changes in lithology, including the sediment-igneous basement interface, alternations of packages of pillow flows and massive flows, and thick inter-flow sediment layers. A high amplitude basement reflection occurs at the top of the igneous crust, resulting from the large increase in density and sonic velocity at that interface. In most places, it can be recognized because of its amplitude, the contrast of its rugged surface with smoother sediments above, and the fact that it is an angular unconformity in many spots. In some places, however, intra-basement reflectors are sub-parallel to sedimentary reflectors and the basement acoustic contrast is not strong, so the igneous basement interface can be difficult to recognize. Nevertheless, in such places it is usually possible to follow the igneous basement surface from adjacent regions where it is clear.

Within the igneous basement, given the long wavelength of the sound source and the synthetic seismogram results, individual lava flows are not usually resolved because they are frequently too thin to cause a significant reflection or there is no significant velocity-density contrast across the flow boundaries. Instead, intra-basement reflectors are typically the surfaces of packages of lava flows where gross changes in lithology occur. For example, this occurs as at Site U1347 where a zone of pillow lavas punctuates a series of massive flows (Figure 3), resulting in a decrease in sonic velocity and density between the dense massive flows. This change in properties probably occurs because the

pillows are frequently separated by rubble and volcaniclastic sediment, which has lesser bulk density and velocity compared to the massive flows. This finding is similar to interpretations of seismic data from the Ontong Java Plateau, in which intra-basement reflections are thought to result from alternating groups of pillow and massive lava flows (Inoue et al., 2008). At Site U1347, I also observe reflectors apparently caused by the contrast between massive flows and thick inter-flow sediment layers (Figure 3). Site U1348 is a different situation because only volcaniclastic material was recovered and this lithology gives many, short-wavelength reflectors (Figure 4). This signature is apparently a result of highly variable density and sonic velocity caused by layering within the volcaniclastics. Although the intra-basement reflections usually occur from alternations of lithology, these changes occur at lava flow surfaces, so the seismic images are nevertheless useful to illustrate the structure of lava flows. Similar interpretations have been made for intra-basement reflectors within other oceanic plateaus (Rotstein et al., 1992; Uenzelmann-Neben et al., 1999; Inoue et al., 2008).

The correlation between the seismic reflections and the geology from synthetic seismograms gives us a key for interpreting igneous basement reflection patterns. Seismic layering results from the transition between sediments and igneous rocks, the surfaces of lava flow packages, and gross changes in lithology, which are usually bounded by lava flows. Thus, the basement reflector shape illustrates the morphology of the igneous basement surface and the intra-basement reflector geometries mainly denote sequences of lava flows.

2.5.2 Structure and evolution of Shatsky Rise massifs

The basement reflectors show that the igneous basement surface for both Tamu and Ori massifs is relatively smooth, with a shallow slope, and is punctuated with secondary cones. Typical slopes are ~1 °-1.5 °on the upper flanks and <0.5 °on the lower flanks. Analogous shallow slope characteristics are observed in Iceland, which is a large volcanic edifice formed at the Mid-Atlantic Ridge (Tryggvason and Bath, 1961; Rutten, 1964; Rossi, 1996; Sager, 1999). Considering the similar divergent plate boundary settings for both Shatsky Rise and Iceland, shallow slope angles may be a result of large volcanic eruptions on the thin and weak lithosphere at mid-ocean ridges. Moreover, high effusion rate eruptions (indicated by the massive lava flows of Tamu Massif) may result in large areas covered by shallow-angle lava flows (Sager et al., 2010; Bryan et al, 2010). Given that the slopes of Ori Massif are similar to those of Tamu Massif whereas no thick, massive flows were cored from Ori Massif (Sager et al., 2010), the tectonic setting may be the primary factor controlling the slope.

Intra-basement reflectors are continuous over lengths of several to tens of km (Figures 7a, 7b, 10), but piecewise-continuous over hundreds of kilometers (e.g., Figures 6, 9). They are not as clear, conformable, and continuous as typical sedimentary reflectors, but this is not a surprise because lava flows have rougher surfaces. Overall, the reflectors show a pattern of gently dipping lava flow packages trending downhill from the volcanic centers.

The basement and intra-basement reflectors show that Tamu Massif is a large central volcano. Lava flows dip away from the summit in all directions on all MCS lines

that cross the massif. Those profiles that cross the SW-NE-trending axis of Tamu Massif (e.g. Figures 6, 8, 9) show a rounded summit and lava flows inclined down the shallow slope. The composite profile that runs along the axis of Tamu Massif (Figure 12) shows even shallower slopes, but flows also trend downward from the summit. Although many secondary cones are observed, no significantly large sources of lava flows exist except the summit. An important implication is that the source of lava flows is at the center of Tamu Massif. This is different from continental flood basalts, which are thought to be constructed by fissure eruptions from multiple locations (Jerram and Widdowson, 2005; Bryan et al., 2010). My data do not rule out fissure eruptions as a source because individual eruptions cannot be distinguished; however, the data are clear that the pattern of lava flows dipping away from the summit is consistent. This pattern is different from Iceland (Sigmundsson, 2005) and possibly other large oceanic plateaus (e.g. Kerguelen Plateau, Rotstein et al., 1992; and Ontong Java Plateau, Inoue et al., 2008), which may have formed as composite features from multiple volcanic sources. The reason that Tamu Massif formed as a single volcano may be that the Pacific plate drifted rapidly relative to the volcanic source, so that subsequent large eruptions did not overlap (Sager et al., 2013).

Ori Massif also appears to be a large central volcano with similar structure to Tamu Massif but smaller in size. Although I have only two MCS lines that cross it, which means that important details may be missed, it appears to be a broad, central volcano as well. There were no thick, massive flows recovered from Ori Massif (Sager et al., 2010) but Ori Massif is also an immense volcano, so the thick, massive flows may

not be only what build up a large volcano, instead, thinner flows could also make it so. Thick, massive flows may be what it takes to reach the biggest size as Tamu Massif.

Basement and intra-basement reflectors on the lower flanks of Tamu and Ori massifs are smooth in all directions, indicating that the massifs are not fault bounded. On Line A-B, which crosses Tamu Massif along its shortest dimension, the volcano is >550 km in width (Figure 6). This line appears to be the only seismic line that extends beyond the plateau into the adjacent basin because on most other profiles, igneous basement is still deepening at the profile limits. On the west side of this line, Tamu Massif basement declines at shallow angles and merges smoothly with that of the surrounding ocean crust, so that it is impossible to tell precisely where the lower flank of Tamu Massif ends. This observation suggests that long flows covered a wide area around the plateau and that estimates of Shatsky Rise area and volume, which defined the limit by a lower flank depth countour (Sager et al., 1999), are underestimated. The lack of a sharp boundary also indicates that the plateau is not fault bounded, as was inferred from the proximity of plateau formation to the triple junction and the alignment of plateau edges with magnetic lineations (Sager et al., 1999). This is also true for the north flank of Tamu Massif and south flank of Ori Massif (bordering Helios Basin), where it was proposed that rifting occurred related to seafloor spreading (Sager et al., 1999). The absence of obvious faults caused by rifting in the MCS data implies that this interpretation is incorrect.

In MCS profiles crossing both Tamu and Ori massifs, intra-basement reflectors are seen to depths of 0.5-2.5 s TWTT beneath the basement surface (Figures 12, 14). At a velocity of 4 kms^{-1}, which is typical for the upper igneous crust (Korenaga and Sager,

2012), this time corresponds to 1-5 km depth. Because the massifs are ~3 km in height, this means that some of these reflectors are near or below the regional abyssal plain depth. In general, intra-basement reflectors display a shape parallel to the basement surface at depth, implying stability of the volcanic structure. Beneath the summits of both Tamu and Ori massifs, intra-basement reflectors show that the summit shape remains the same for several kilometers depth. This observation implies long-term stability of the summit location. Furthermore, the consistent flank shapes of both edifices imply an emplacement process that maintained isostatic balance. Had volcanism been concentrated solely at the top center of the volcano, the weight of the new lava flows would have depressed the center and buried lava flows would dip toward the center, as is observed for seaward-dipping reflector sequences on continental margins (Mutter, 1985; Planke and Eldholm, 1994; Planke et al., 2000). The fact that Shatsky Rise lava flows are parallel to one another and to the basement surface indicates that the lavas are not concentrated at the center, but spread over the entire surface, so no one part is pushed down relative to others. Furthermore, the emplacement of mass must be balanced to maintain the shape of these volcanoes. This result likely occurs from emplacement of material to the volcano root that balances the material added on top - otherwise the geometry would change with time as material at the top is added. Shatsky Rise was formed at a triple junction and the lithosphere near oceanic ridges is thin and weak, implying no lithospheric strength (Sager et al., 1999; Nakanishi et al., 1999), so Shatsky Rise volcanoes may be in isostatic balance at all times.

The MCS profiles exhibit steeper segments (~3°-5°) of dipping reflectors in some places (e.g. Figures 6, 9) compared to the shallow flank slopes (<0.5°-1.5°) of the volcanoes. The cause of these steeper sections is uncertain, but a possibility is that lava deltas build outward like sedimentary deltas, with steeper slopes on the leading edge. Planke et al. (2000) and Spitzer et al. (2008) attributed steeper "foreset" beds in seaward dipping reflector sequences as indicators of volcaniclastic debris formed near sea level at the toe of advancing lava flows. It is unclear whether the steeper dip of intra-basement reflectors on Shatsky Rise MCS profiles has the same connection to sea level. In many places where they are observed (e.g., Figure 7), these reflectors are too deep to have reached their present depths through normal subsidence (see subsidence curves in Sager et al., 2010), implying another cause.

Large down-to-basin normal faults on massif flanks are observed at many locations (Figure 1). They show offset of the basement and intra-basement reflectors (0.1-1.0s in TWTT =~75-750 m at a velocity of 1500 ms^{-1}). A possible explanation for these faults is rifting related to seafloor spreading around Shatsky Rise. The distribution and orientation (observed in multibeam bathymetry data) of faults shows no apparent correlation nearby magnetic lineations. Moreover, it seems unlikely that seafloor spreading related rifting would produce consistently asymmetric faulting. All of the major faults have a down-to-basin geometry. Another possible explanation for these faults is differential subsidence with the volcano center subsiding less than the flanks because of magmatic underplating beneath the volcanic center (e.g., Ito and Clift, 1998). This suggestion implies that down-to-basin faults should be found on all sides of Shatsky

Rise. In contrast, the large down-to-basin normal faults are observed only on the western flanks of Shatsky Rise (Figure 1). Although existing data are sparse and probably do not show all such faults, the uneven distribution of normal faults is an unexplained complexity to the Shatsky Rise subsidence history.

Secondary cones are seen on almost all seismic lines and it appears that they are scattered across the volcano at all depths, with no particular area of concentration. Their seemingly random distribution suggests that they are not tied to any large-scale structure. Given that about three dozen such cones are observed on the Tamu Massif seismic lines (Figures 6, 8, 9, 11, 12, 13), which sample only a small area (<5% of entire Tamu Massif), there must be on the order of hundreds of secondary cones that dot the flanks of this volcano. The secondary cones range from small (< 5 km wide, a few hundred meters height) to large (tens of km across and ~1 km in height) (e.g. Figures 6, 11). Generally they have steeper slopes (~5 °) and are sometimes conical but sometimes complex in topographic structure (e.g. Figure 13). Bathymetric maps derived from satellite gravity image them poorly, but many have been observed in shipboard bathymetry data. In many large volcanoes (e.g., Hawaii (Macdonald and Abbott, 1970)), secondary cones occur along rift zones because these are the sources of major eruptions, but that does not appear to be true for Shatsky Rise. Perhaps these secondary cones are formed when lava flows are constrained from lateral flow and breakout vertically. The large basement high upon which Site U1348 was drilled appears to be a significant secondary source of volcanism. It is a more-or-less cone-shaped feature ~25 km across and ~1 km in height (Figures, 11, 12). Volcaniclastics were cored at its summit, implying explosive shallow

water volcanism (Sager et al., 2011). Its summit was also near sea level as shown by shallow water fossils (Sager et al., 2010). Although the Site U1348 cores imply that many secondary cones consist of volcaniclastic material, some may be basaltic cones, such as those that form on other large volcanoes (Beiersdorf et al., 1995).

2.5.3 Summit morphology and sea level

Summit basement morphology maps show that large basement peaks are common atop the large Shatsky Rise massif volcanoes. Tamu Massif has two large basement peaks, the eastern broad rounded peak and Toronto Ridge (Figure 6). The broad rounded peak has low slopes and is the center of the volcano shield-building stage. Toronto Ridge has a rounded top; although, there is a break in slope between the top and the steeper flanks. Its depth (~2 km) would have made it subaerial when the deeper summit was erupted, as inferred from shallow water sediments recovered at nearby Site U1347 (Sager et al., 2010), which is ~2 s TWTT (~1.5 km) deeper. The lack of evident erosion due to subaerial exposure implies that this ridge is a late stage volcanic eruption, emplaced after significant subsidence of the volcano. Furthermore, its steeper side slopes imply a different style of volcanism from the Tamu Massif shield building stage, similar to that of the secondary cones on the massif flanks or normal seamounts.

The Ori Massif summit shows two large basement peaks as well. One, on the NE side of the Ori Massif summit, has a rounded top, similar to Toronto Ridge on Tamu Massif (Sager et al., 1999). The other, at the central summit, has a nearly flat top and intra-basement reflectors that are nearly horizontal (Figure 14). The Shirshov Massif

summit has one large basement peak with a rounded shape similar to other secondary cones (Sager et al., 1999). Layering within this peak follows its slopes, implying that it is a volcanic cone rather than an erosional remnant.

Although the large basement peaks at the three massif summits have different structures, I see similar features on other seismic lines at different locations. On Line C-F (Figure 13), which crosses a low ridge on the south distal flank of Tamu Massif, examples of three different cone structures are observed. Between SP 4900-SP 5100, two secondary cones occur and display sharp peaks (the sharpness a result of the vertical exaggeration and the true slopes are only ~5°-10°). Such cones are typical of the secondary cones that dot the Shatsky Rise flanks. At SP 5400, a broader cone occurs with a rounded top. Within this cone, seismic layering is observed to follow the summit shape (i.e., bowed upward). This cone is similar to Toronto Ridge on Tamu Massif and the ridge on the NE side of the Ori Massif summit. At SP 2100, a flat-topped ridge is observed, similar to the central Ori Massif summit ridge. Its steep sides and the apparent truncation of internal parallel reflectors along the sides could indicate bounding normal faults as well. However, interpreting both of these similar features as a horst blocks makes little sense, because there is no obvious mechanism to down-fault the volcano surrounding each of these cones. Furthermore, because of the depth of the cone on Line C-F, the flat summit cannot be attributed to erosion at sea level. Instead, I think the flat interior structure and top are constructional features. Hence, all of the summit ridges on the three massifs imply that volcanism continues and changes character after the initial shield-building stage of massive volcano construction. Similar features on other large

volcanoes form long after the main shield-building volcanism has concluded (MacDonald and Abbott, 1970) and circumstantial evidence from Shatsky Rise volcanoes implies the same.

According to the evidence from samples recovered by drilling and dredging, the summits of the three massifs within Shatsky Rise must have been in shallow water when volcanism ceased. Shallow water fossils were dredged from a secondary cone at ~3000 m depth on southeast side of Tamu summit (Sager et al., 1999). Moreover, evidence for shallow water was found in basal sediments for Sites U1347, U1348 (Tamu Massif upper flanks), U1349 (Ori Massif summit), and U1346 (Shirshov Massif summit) (Figure 1). These findings agree with backtracking of the sites using subsidence models, which also imply the sites would have been in shallow water when the sediments were deposited (Sager et al., 2010). Given that Site U1347 lies ~800 m deeper than the shield summit of Tamu Massif, Sager et al. (2010) inferred that the summit may have been subaerial. This inference seems contradicted by lack of obvious subaerial erosion on seismic lines. Line A-B (Figure 6) is the only MCS line over the shallowest part of the summit. It shows no notching or flattening of the summit owing to erosion. Cruise TN037 seismic lines also cross the Tamu Massif summit and they also show no evidence of erosion (Sager et al., 1999; Klaus and Sager, 2002). Because all of the evidence on Tamu Massif for sea level is from sediments interpreted as deposited in shallow water (not actual evidence of exposure), I infer that Tamu Massif reached near sea level, but was not emergent. Ori Massif is similar because seismic lines over this volcano also show no evidence of significant subaerial erosion (Figures 12, 14). The only evidence of

emergence is from the top of the summit ridge, where the juxtaposition of a paleosol and shallow water carbonate sediment layer imply formation exactly at sea level (Site U1349, Figure 1) (Sager et al., 2010). This ridge was likely the highest point on Ori Massif, suggesting that the bulk of the volcano formed below sea level. Site U1346 at the north edge of the Shirshov Massif summit (Figure 1) indicates shallow water depositional environment (Sager et al., 2010) and the Shirshov Massif summit has an overall flat basement structure that has been interpreted as a subaerially eroded summit platform (Sager et al., 1999); however, the TN037 seismic data show no evidence of erosion on the Shirshov Massif summit (Sager et al., 1999; Klaus and Sager, 2002). The summit cones are not erosional remnants and the "flat" summit platform is actually undulatory and shows no truncation of basement layering. Hence, Shirshov Massif may have stayed submerged as well.

Calderas are common features at the summits of large volcanoes and result from collapse of evacuated magma chambers near the end of the volcano history (MacDonald, 1972). Usually, these features exist near or at the eruptive sources. Two summit grabens are observed on Tamu Massif (Figures 6, 9, 12), range from ~55-170 m in depth and ~3-15 km across. Both dimensions and locations where the depressions are found are similar to those of calderas on other large volcanoes (MacDonald, 1972; Walker, 2000), suggesting that they may have analogous origin (Sager et al., 2013). The two observed depressions are ~ 100 km apart (Figure 1), but occur along the SW-NE axis of the elongated shape of Tamu Massif. Because there are no intervening seismic lines, it is impossible to tell whether they are connected. Both occur along the Tamu Massif

summit, consistent with the idea that Tamu Massif formed mainly from summit eruptions (Sager et al., 2013). No similar collapse depressions are found on Ori and Shirshov massifs, but data are sparse and collapse depressions may have been missed by existing tracks.

2.5.4 Origin of Shatsky Rise

Near surface structure is not diagnostic of the proposed mechanisms (plume or non-plume) of oceanic plateau formation, so surface geophysical data are not suited to determine unequivocally which is correct. However, some of the observations made here can help constrain the explanations used for oceanic plateau formation. Combined with drilling data (Figure 2; Sager et al., 2013), the seismic data offer a compelling view of Shatsky Rise as consisting of several immense volcanoes. Tamu Massif is the largest and oldest volcano within Shatsky Rise, and it appears to be a single volcano with the size of the largest volcanoes in the solar system and possibly the largest single volcano on Earth (Sager et al., 2013). Such a large volcano, characterized by massive lava flows, implies massive and rapid eruptions. Therefore, whatever mechanism is used to explain the formation of Shatsky Rise, it must be able to emplace an immense amount of magma, forming a large volcano at one place and perhaps in a short time. This result probably fits with the plume head hypothesis, as does the evident trend to smaller volcanic output with time to Ori and Shirshov massifs (Sager, 2005). However, the big dimension of volcanic constructs is not necessarily connected to the plume model, because decompression melting at plate boundaries (the "plate" model) also could form large

volcanic edifices (Foulger, 2007). It is clear from magnetic lineations that Shatsky Rise formed at a ridge-ridge-ridge triple junction (Nakanishi et al., 1999), so the plateau is definitely linked to plate boundary mechanism. Unfortunately, little evidence found from the MCS data supports the idea of spreading-ridge rifting on the flanks of the Shatsky Rise massifs. If Shatsky Rise formed from rifting related decompression, it must cover up the evidence of rifting.

Although Shatsky Rise is composed of several enormous volcanoes, it appears to have remained mostly submerged because seismic data show no evidence of the subaerial erosion that would be caused by significant uplift. This observation does not appear fit the simple thermal plume head hypothesis, which calls for significant dynamic uplift (e.g. Coffin and Edholm, 1994). However, it is notable that the larger Ontong Java Plateau also stayed submerged during its formation (Fitton et al., 2004). One explanation for submarine eruptions of Ontong Java Plateau is that dense fertile mantle was entrained by rapid seafloor spreading and this dense mantle material caused the plateau to be isostatically depressed and to subside anomalously (Korenaga, 2005). Shatsky Rise also formed near fast spreading ridges (Nakanishi et al., 1999) and its crustal velocity structure suggests that the mantle source was chemically anomalous (Korenaga and Sager, 2012), so it may have experienced similar mantle dynamics. This similarity suggests that some factor in the formation of some basaltic oceanic plateaus keeps them from rising above the sea surface.

2.6 Conclusions

Modeling and correlation of synthetic seismograms using core and log velocity and density data from scientific drilling sites crossed by the MCS lines establishes the seismic response to geology for Shatsky Rise volcanoes. High amplitude basement reflections result from the transition between the sediment and igneous rock. Intra-basement reflections are caused by alternations of lava flow packages with differing properties and by thicker inter-flow sediment or volcaniclastic layers. Therefore, the basement and intra-basement reflectors can be traced in the MCS profiles to examine the morphology of the igneous basement surface and the structure of lava flows below that surface.

The overall structure of Shatsky Rise shows that the plateau is composed of several immense central volcanoes. Tamu Massif, the largest and oldest volcanic edifice within Shatsky Rise, is a massive, dome-like, volcano. It is characterized by shallow flank slopes (<0.5 °-1.5 °) constructed by lava flows mostly emanating from the volcano center and extending hundreds of kilometers down the generally smooth flanks to the surrounding seafloor. The morphology of the massif implies formation by extensive and far ranging lava flows emplaced at small slope angles. The relatively smooth flanks indicate that no significant rifting occurred due to spreading ridge tectonics, even though Shatsky Rise formed at a triple junction. In addition, the shape of the volcanic center appears to remain stable because the underlying lava flows follow the same shape at depth, suggesting that the volcanic emplacement must be in isostatic balance at all times. Important implications are that the addition of material cannot be concentrated at the

center of the volcano, or it would subside more than the flanks, and that isostatic balance requires the addition of material to the volcano root to balance eruptions on the surface. Ori Massif is another large, central volcano with similar structure but smaller in size compared to Tamu Massif. Ori Massif also shows no evidence of spreading-ridge rifting on its flanks. The basin between Tamu and Ori massifs (Helios Basin), which was thought to have formed by rifting, is not bounded by large faults and instead reflects a gap in the volcanism between the two volcanoes. Shallow water evidence had been found from drilling and dredging either at the summits or on the upper flanks of all three massifs of Shatsky Rise, suggesting that the summits of the massifs must have been in shallow water when they formed. In contrast, the seismic data show no evidence of subaerial erosion, implying that these volcanoes were never highly emergent.

CHAPTER III

THE MOHO STRUCTURE OF SHATSKY RISE OCEANIC PLATEAU, NORTHWEST PACIFIC, FROM MULTICHANNEL SEISMIC REFLECTION AND REFRACTION DATA

3.1 Overview

Moho structure provides important clues for understanding crustal structure, isostatic state and magmatic flux from the mantle. This structure is often poorly known because the discontinuity is deep within the Earth. Oceanic plateaus are large igneous constructs with anomalously thick crust whose crustal structure is important evidence about their formation. Multichannel seismic (MCS) reflection and wide-angle refraction data were collected over the south half of the Shatsky Rise oceanic plateau and these data allow us to image the Moho of the plateau. MCS reflection data reprocessed by Constant Velocity Stack (CVS) instead of normal CDP stack produced clearer seismic reflection images of the Moho. MCS reflection sections show Moho reflectors are highly variable in length and shape and strength. This variability is similar to other Moho observations in the oceans, likely resulting from a combination of the change of real Moho structure and the variable imaging conditions owing to the scattering effects in the crust. The Moho reflectors closer to the center of the massifs are weaker, probably because of greater attenuation with depth, masking by multiples, or lower Moho reflectivity due to more melting at the massif center. Moho reflectors start shallow (~7 km) beneath normal crust at the distal flanks of Shatsky Rise and dips (~3-5^{o}) towards

the center of plateau massifs, and it can be seen in MCS images up a thickness of ~17 km. Moho depths from MCS reflection data can be matched with those from refraction data, showing that the dip continues toward the middle, reaching maximum thickness of ~ 30 km at the center. Shatsky Rise crustal structure is consistent with the Moho topography of isostatically compensated crustal structures, which is why the plateau exhibits a small free-air gravity anomaly signature. Shatsky Rise was built on young oceanic lithosphere with little rigidity, so the plateau formed in isostatic equilibrium with a deep crustal root.

3.2 Introduction

The geometry of the Mohorovicic discontinuity (aka "Moho") is important for understanding crustal structure, isostatic compensation, and magmatic flux from mantle to crust, but the structure of the Moho is still poorly known because it is hidden deep within the Earth, making it difficult to image and study in detail. Although the Moho is commonly recognized as the boundary between the crust and the mantle, scientists have distinguished two versions, the petrologic and seismic Moho (e.g. Mengel and Kern, 1992). The petrologic Moho is considered the boundary between non-peridotitic crustal rocks (with gabbro composition) and olivine-dominated mantle rocks (with peridotite composition) (Nedimovic et al., 2005). The seismic Moho is defined as a first-order velocity discontinuity, which marks the boundary where P-wave velocities increase abruptly from crustal values (<7.2 km/s) to mantle values (>8.0 km/s) (Rohr et al., 1988; Holbrook et al., 1992). These two distinct definitions are based on different criteria: the

petrologic Moho is a compositional difference, whereas the seismic Moho reflects a change in elastic parameters. Both are based on a simple layered model, implying that the Moho is a sharp transition between crust and mantle. Furthermore, the two types of Moho may not be in identical positions in depth because lower crustal gabbros may be transformed into high-pressure mineral assemblages that have high velocities and densities similar to the mantle (Mengel and Kern, 1992). In this chapter I examine seismic data and are therefore imaging the seismic Moho.

Knowledge of the seismic Moho comes primarily from wide-angle seismic refraction, and near-vertical incidence multichannel seismic reflection (MCS) data (Holbrook et al., 1992; Trehu et al., 1989). Wide-angle refraction data generate a velocity-depth model using seismic wave travel time curves and ray tracing models (Holbrook et al., 1992). Vertical seismic profiling is usually designed to image the upper crustal structure, but sometimes reflections from the Moho are observed (Mutter and Carton, 2013). The near-vertical incidence of seismic waves limits the imaging efficiency at great depths, so Moho reflections are often intermittent. The advantage of wide-angle refraction is that the Moho is often clearly defined by travel time and amplitude differences between the mantle and crustal events. In contrast, with MCS profiles, the Moho is commonly associated with the deepest visible reflectors on stacked sections (Holbrook et al., 1992; Collier et al., 1994; Gallart et al., 1995). Nevertheless, a combination of MCS and wide-angle refraction data can produce a more robust seismic model of the crust than with one method alone (e.g. Mjelde et al., 1993; Gallart et al., 1995).

Oceanic plateaus are large submarine mountains, many of which were formed by extensive basaltic volcanism (Coffin and Eldholm, 1994). The deep crustal structures of oceanic plateaus from wide-angle seismic refraction surveys reveal that they have anomalously thick crust (Ridley and Richards, 2010), for example, Ontong Java Plateau (up to ~40 km thick; Furumoto et al., 1976; Gladczenko et al., 1997; Miura et al., 2004), Kerguelen Plateau (up to ~24 km thick; Charvis and Operto, 1999; Borissova et al., 2003), and Agulhas Plateau (up to ~25 km thick; Gohl and Uenzelmann-Neben, 2001; Parsiegla et al., 2008). A primary reason for the great crustal thickness is that such large features overwhelm the strength of the lithosphere, so they have deep crustal roots to effect Airy isostatic compensation (Watts and Ribe, 1984; Sandwell and MacKenzie, 1989). One result of the complete compensation is that plateaus typically exhibit small free-air gravity anomalies (Sandwell and Smith, 1997).

Shatsky Rise, located in the northwest Pacific Ocean, ~1500 km east of Japan, is one of the largest oceanic plateaus. Until recently, its crustal structure was poorly known owing to the lack of modern deep penetration seismic data. New marine seismic data were recently acquired from the seismic vessel R/V *Marcus G. Langseth* on two cruises in 2010 and 2012. During one of these cruises, wide-angle seismic refraction data were collected by ocean bottom seismometers (OBS) over the southern Shatsky Rise, allowing the calculation of a tomographic cross section (Korenaga and Sager, 2012). 2D MCS reflection profiles were collected over the southern half of Shatsky Rise, giving a picture of the upper crustal structure (Sager et al., 2013; refer to Chapter II). In this chapter, I examine deep reflectors in the MCS reflection data to show the geometry of

the Moho and give a more complete view of crustal structure of the rise. Shatsky Rise exhibits nearly zero free-air gravity anomaly (Sandwell and Smith, 1997) and this oceanic plateau is therefore in apparent isostatic equilibrium. Thus, the plateau Moho structure is expected to demonstrate crustal thickening consistent with the Airy mechanism of isostatic compensation, a hypothesis that can be tested with the new MCS data.

3.2.1 Geological framework

Shatsky Rise has an area of 4.8×10^5 km^2, similar to that of Japan (Sager et al., 1999). The plateau has an elevation of 3-4 km from the surrounding seafloor at ~ 6-5.5 km water depth to its shallowest summit at ~ 2.0 km water depth (Figure 16). Three bathymetric highs and a low ridge are recognized within Shatsky Rise. From southwest to northeast they are Tamu Massif (the oldest and largest), Ori Massif, Shirshov Massif and Papanin Ridge (Figure 16) (Sager et al., 1999).

Owing to its location exactly at the junction of two magnetic lineation sets, the Japanese and Hawaiian lineations, it is proposed that Shatsky Rise formed at a triple junction (usually with ridge-ridge-ridge geometry) (Sager et al., 1988; Nakanishi et al., 1999). The plateau began to form at Tamu Massif at about the time of adjacent magnetic chron M21 (149 Ma, using the time scale of Gradstein et al., 2004), which is consistent with a radiometric date of 144.6 ±0.8 Ma, determined from basalt cores recovered at Ocean Drilling Program (ODP) Site 1213 on the south flank of Tamu Massif (Mahoney et al., 2005). Magnetic anomalies show that the age of the seafloor becomes younger to

the NE and the axis of Shatsky Rise coincides with the triple junction until chron M1 (126 Ma). This progression implies that after Tamu Massif was created, the triple junction drifted northeast with Ori and Shirshov massifs and Papanin Ridge forming along its path (Sager et al., 1999; Nakanishi et al., 1999). Tamu Massif may have formed rapidly, within a period of 1-2 Myr or less (Sager and Han, 1993); however, based on the span of magnetic anomalies, it took ~23 million years for the entire Shatsky Rise to form.

This submarine plateau is mostly covered by thin pelagic sediments (Ludwig and Houtz, 1979), except for thick sediment ponds at the summits (mostly Cretaceous carbonates, up to ~1km) (Karp and Prokudin, 1985; Khankishiyeva, 1989; Silter and Brown, 1993). Basaltic basement rocks were recovered from Shatsky Rise at ODP Site 1213 (Shipboard Scientific Party, 2001; Koppers et al., 2010) and at Integrated Ocean Drilling Program (IODP) sites U1346, U1347, U1349 and U1350 (Sager et al., 2010; 2011), confirming the volcanic nature of this oceanic plateau. Two types of lava flows are found at most of the sites, massive sheet flows and pillow lavas, corresponding to volcanic eruptions at high and modest effusion rates respectively (Sager et al., 2013). Massive flows with thicknesses up to ~ 23m were cored at Tamu Massif and indicate voluminous eruptions (Sager et al., 2010; 2011). Thinner and less common massive flows make up the cored sections of the smaller Shatsky Rise massifs (Ori and Shirshov massifs), implying that igneous output waned in volume with time at Shatsky Rise, following an initial burst of massive magmatic eruption at Tamu Massif (Sager et al., 2010; 2011).

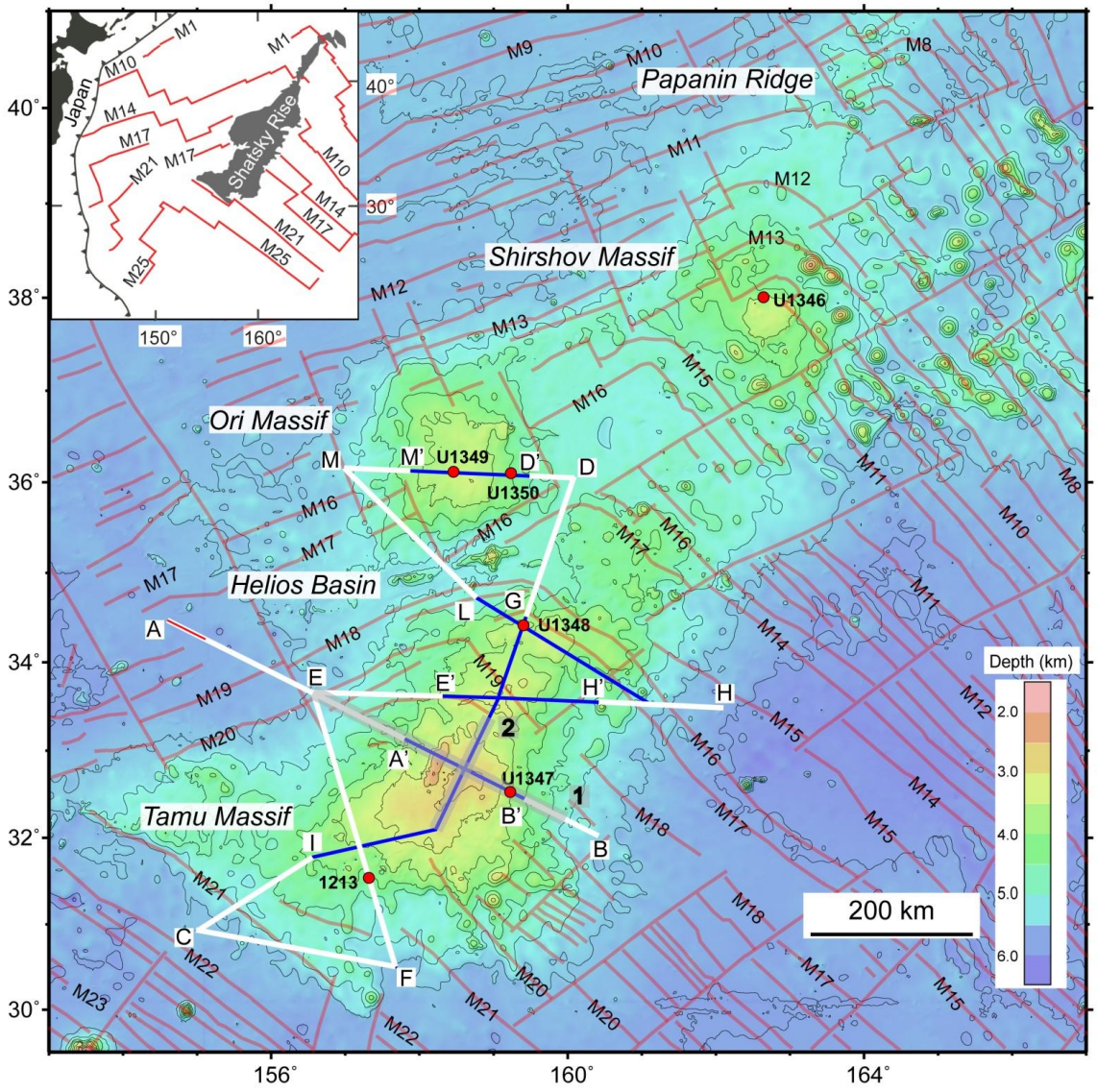

Figure 16. Bathymetry and tectonic map of Shatsky Rise with seismic track lines. Bathymetry is from satellite-predicted depths with 500-m contours (Smith and Sandwell, 1997). Heavy red lines show magnetic lineations with chron numbers labeled for reference (Nakanishi et al., 1999). Heavy lines show MCS reflection profiles collected by R/V *Marcus G. Langseth* on cruises MGL1004 and MGL1206. White lines denote seismic sections that display the Moho reflection, whereas blue lines are those that do not. Letters identify sections discussed in the text. Red line denotes the portion of section A-A' shown in Figures 17 and 18. Heavy gray lines with numbers 1 and 2 are OBS refraction lines (Korenaga and Sager, 2012). Filled red circles show locations of ODP and IODP drill sites mentioned in the text. Inset depicts the location of Shatsky Rise relative to Japan and nearby subduction zones (toothed lines) and the wider magnetic pattern.

3.2.2 Seismic data

Most of seismic data acquired over Shatsky Rise are of poor quality by current standards. Den et al., (1969) and Gettrust et al., (1980) both collected seismic refraction data from Tamu Massif to establish velocity-depth models. However, neither study recorded the base of the crust under the thickest part of the plateau, and their results are somewhat unreliable due to the outdated techniques applied. Most existing seismic reflection data are low-resolution single channel seismic reflection profiles, which are not useful for studying the sub-sediment structure of Shatsky Rise. Although cruise TN037 in 1994 collected a number of 2 and 3 fold MCS profiles over Shatsky Rise (Klaus and Sager, 2002), these data rarely have significant penetration into the igneous basement.

3.3 Data and methods

Two cruises of the R/V Marcus G. Langseth visited Shatsky Rise (cruises MGL1004 and MGL1206) to collect high quality marine seismic data. Two Ocean Bottom Seismometer (OBS) refraction lines were collected over Tamu Massif and twelve MCS reflection profiles totaling 3350 km in length were collected over the south half of Shatsky Rise (Figure 16). For both cruises, the refraction and reflection data were both acquired with using a source array with 36-airguns (volume 108.2 L), but in a 162-m and 50-m shot spacing respectively. For the refraction study, 28 OBS (21 on line 1 and 7 on line 2, spacing 20 km) collected data. For the reflection study, a 6-km-long,

468-channel streamer (hydrophone array) with a 12.5-m group interval was used as the receiver.

Refraction data were processed by adaptive-importance sampling to produce a tomographic cross section across the center of Tamu Massif, which shows a maximum crustal thickness of ~30 km (Korenaga and Sager, 2012). Reflection data processed with standard MCS processing steps showed the upper crustal structure with lava flows dipping down the flanks of Tamu and Ori massifs (Sager et al., 2013; refer to Chapter II). Although a Moho reflector was commonly observed in these data, the MCS data were reprocessed using constant velocity stacks (CVS) to enhance these reflections. CVS is a processing method that uses a pre-determined constant velocity for the entire time domain to stack the CDP traces, whereas normal CDP stack uses a velocity-depth model from standard semblance velocity analysis. Since the Moho reflection in MCS data is deep and weak in amplitude, it is difficult to obtain an optimal stacking velocity for the Moho by looking at the semblance. I tested a range of plausible velocities for CVS stacking to find the value that provided the clearest images.

Using standard seismic stratigraphy techniques (Mitchum et al., 1977), seismic horizons were correlated and interpreted in geologic terms. In particular, my focus was on layering within the part of the seismic sections that contain the Moho reflection. The Moho is interpreted by the deepest visible reflector in MCS reflection profiles.

To compare results from OBS refraction and MCS reflection data and to generate composite crustal structure sections, refraction Moho depths were taken from the seismic tomography model of Korenaga and Sager (2012) and MCS reflection Moho depths

were calculated from reflector two-way travel time with assumed velocities for the water column, sediment and igneous crust of 1500 m/s, 2000 m/s and 6500 m/s respectively. The latter value has the greatest effect on calculated Moho depth and it was adjusted by trail and error to fit the seismic refraction-determined depths where these data overlapped. For MCS reflection sections in the absence of refraction data or where the refraction data and reflection data do not overlap, the same velocities were used to convert Moho depths from two-way travel time to depth.

In order to compare Shatsky Rise Moho structure to Airy isostatic compensation, a simple isostatic model was calculated given the condition for isostatic equilibrium in the ocean (Kearey et al., 2009): r=h(c-w)/(m-c), where r is the thickness of the crustal root, h is the mountain height above the base level, c is average crustal density, w is water density, and m is mantle density. I assumed water, average oceanic crust and upper mantle densities of 1000 kg/m3, 2890 kg/m3(Carlson and Raskin, 1984), and 3150 kg/m3(Talwani et al., 1965), respectively. Given these densities, the isostatic model predicts that the relief on the Moho is approximately seven times the relief at the seafloor.

3.4 Results

3.4.1 Constant velocity stack

Taking a deep crustal portion of MCS line A-A' containing the Moho reflection (Figure 17), a range of CVS stacking velocities (2500 to 5000 m/s) were tried to determine which velocity provides the clearest image of the Moho. Initially, a large

range of values was tried, with steps at 500 m/s. Subsequently, 250 m/s steps were evaluated over a smaller range where the Moho reflectors were clearest. As shown in Figure 17, the Moho loses some segments of the reflection when the velocity is either ≤3000 or ≥5000 m/s. The clearest images were obtained between 3500 and 4500 m/s. Further examination indicated that velocities between 3750 and 4250 m/s worked well, with 4000 m/s giving optimal results.

Comparing the CVS stack image to a normal CDP stack for the short portion from line A-A' (Figure 18), the Moho is clearer and more continuous in the CVS stack. For example, the weak Moho reflector on the west side of the test section is unclear, whereas the CVS stack section shows the reflector clearly. In the rest of the section, the CVS stack displays strong Moho reflectors in the center and clearer and more consistent reflectors on the east.

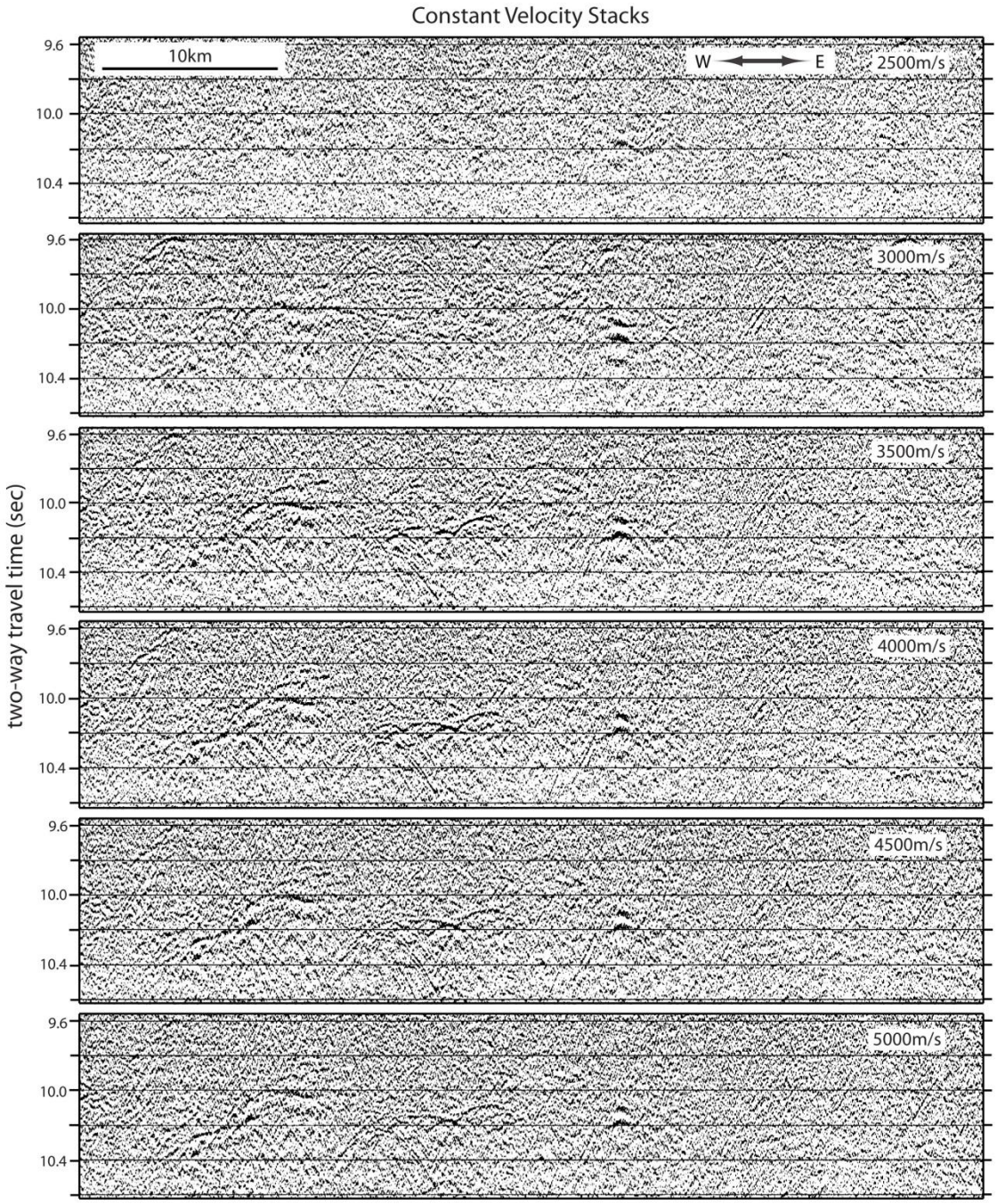

Figure 17. Constant velocity stack results from a portion of section A-A' containing the Moho reflection. Location is shown in Figure 16. Stacking velocities range from 2500 (top) to 5000 m/s (bottom).

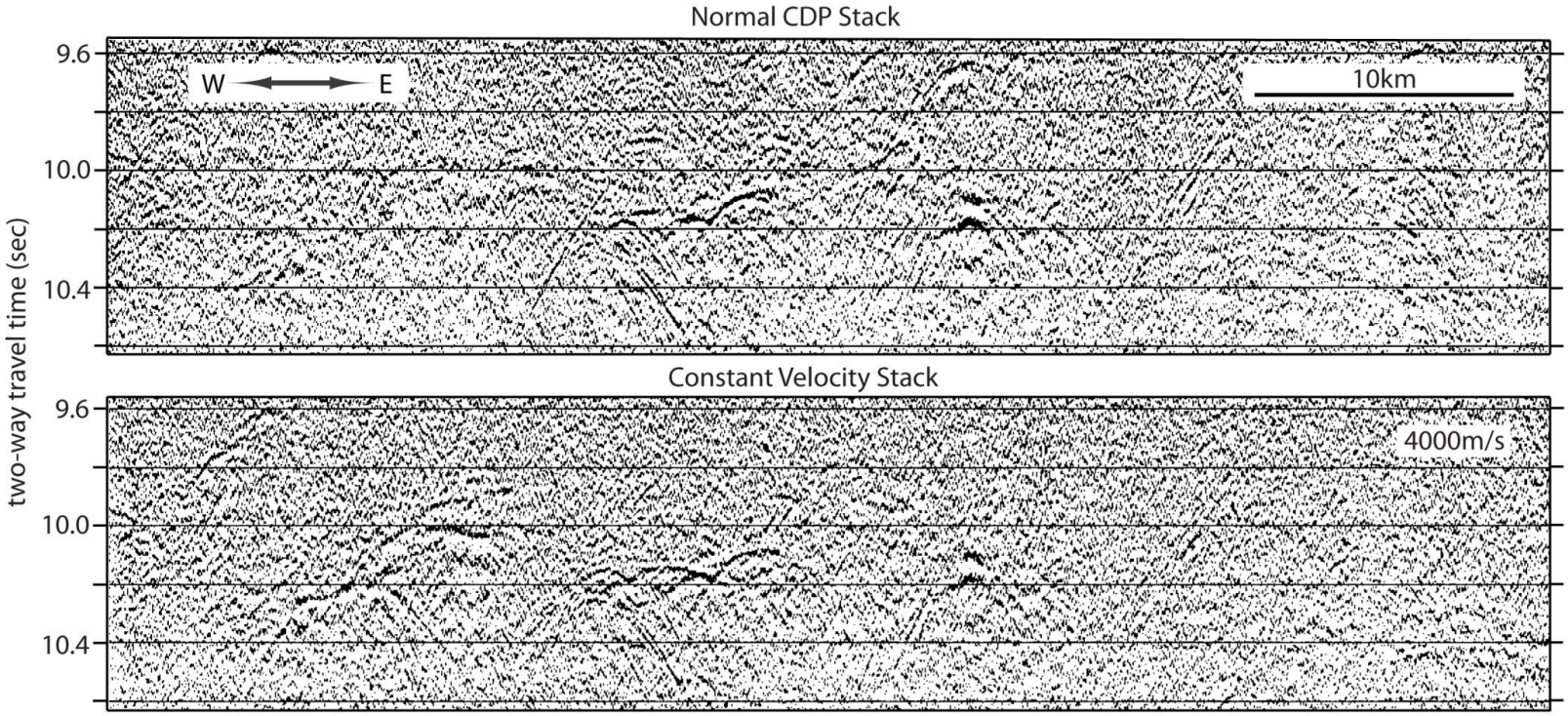

Figure 18. Comparison between the normal CDP stack and the constant velocity stack using a velocity of 4000 m/s for the portion of section A-A' shown in Figure 17.

3.4.2 Multichannel seismic reflection images of the Moho

Reflection Moho is routinely observed on MCS profiles over Shatsky Rise, but it is not observed everywhere. In particular, those MCS line segments containing the Moho reflection are located on the lower flanks of the massifs and on the surrounding seafloor (Figure 16). In the summit areas, where the crust is thickest (Korenaga and Sager, 2012), the Moho reflections are not observed.

Moho reflectors are highly variable in: (1)length, ranging from several to tens of kilometers; (2)shape, ranging from flat to curved or mounded; (3)strength, ranging from sharp and strong to weak or absent. In general, the Moho reflectors are discontinuous with gaps of a few kilometers in between segments, and they become weaker approaching the center of the massifs. However, the Moho reflectors appear to be piecewise-continuous, which means adjacent individual reflectors can be connected by following their trend to infer the broader structure of the Moho.

3.4.2.1 Tamu Massif

On Tamu Massif, the Moho reflection is observed beneath its lower flanks on all sides (Figure 16). Line A-B crosses the center of Tamu Massif. On segment A-A' (west flank), discontinuous Moho reflectors are clearly observed, starting from the basin at the depth of ~10 sec two-way travel time (TWTT) (~13 km), extending almost horizontally to ~shot point (SP) 8500, and then dipping (~3^{o}) down towards the center of the massif and finally disappearing at a depth of ~11 sec TWTT (~17 km), where multiples occur (Figure 19). Individual Moho reflector segments are several to tens of kilometers long

with gaps of a few kilometers in between. However, the Moho reflectors appear to be piecewise-continuous and individual Moho reflectors can be connected with one another to infer a long horizon beneath the west side of Tamu Massif. Individual Moho reflector segments display different shapes, for example, flat (SP 10400), curved (SP 11800, 8800), and mounded (SP 12800, 11000). The Moho reflectors also have variable strength, for example, strong reflectors occur at SP 10400, 11300, whereas weak ones occur at SP 8000, 9900.

Segment B-B' of line A-B images the lower eastern flank of Tamu massif, but not far enough to reach the surrounding deep water seafloor as segment A-A' does. The surface topography is rough due to the occurrence of secondary cones (refer to Chapter II; Figure 19). Beneath the cones (SP 1500, 2000 and 2600) no Moho reflectors are observed, likely because the cones scatter the seismic signal. However, Moho reflectors are seen in between the cones. Showing a geometry similar to segment A-A', they also decline (~4^{o}) down towards the center of the massif and die away before running into the multiples.

Similar to line A-B, line E-H (Figure 20), across the north of Tamu Massif, shows analogous structure of the Moho on both western and eastern flanks, i.e. discontinuous Moho reflectors representing a piecewise-continuous horizon that dips (~3) towards the center of the massif. In some places, the Moho reflectors are also missing beneath flank cones (e.g. at SP 3900 in segment H-H'; Figure 20). The Moho is observed to a depth of ~11 sec TWTT (~20 km) before disappearing near the multiple reflection (in segment E-E'; Figure 20).

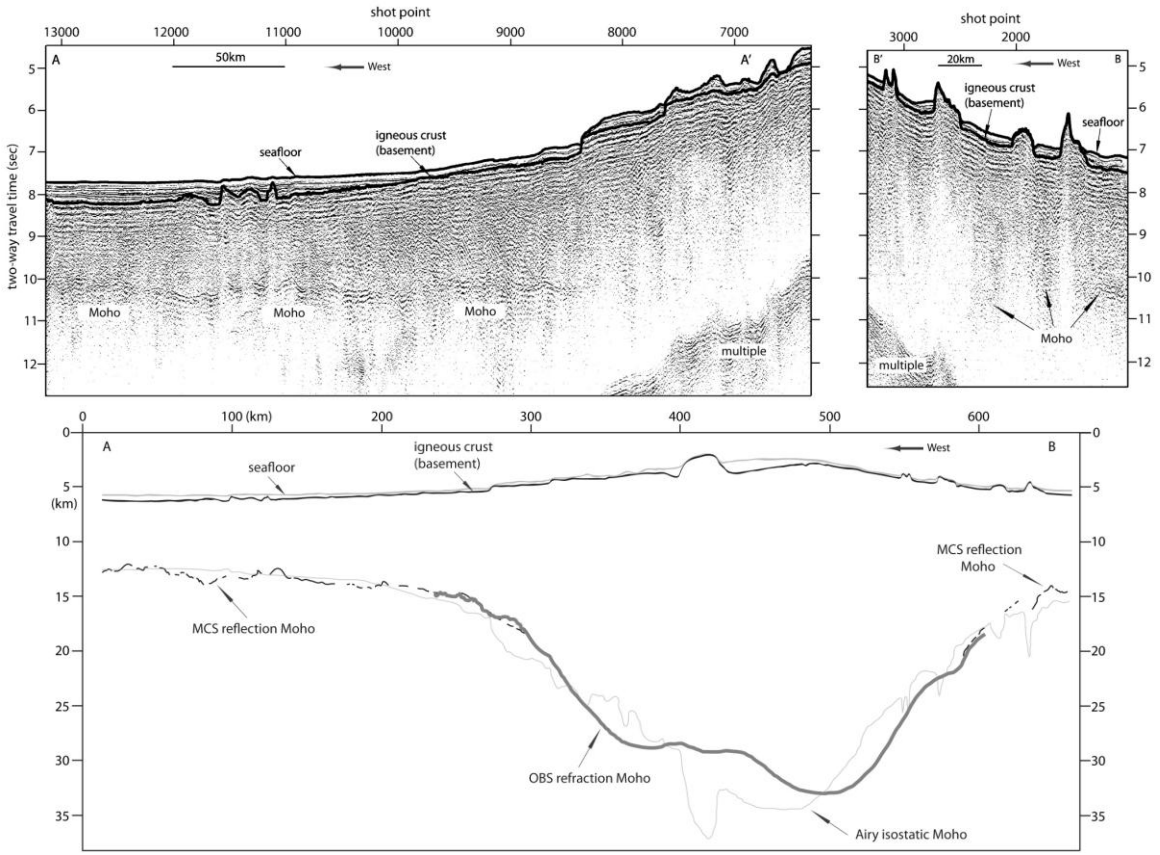

Figure 19. MCS reflection images and crustal structure of line A-B, across the center of Tamu Massif. Top panel shows MCS reflection images for the line segments A-A' and B-B', which display Moho reflectors. Vertical exaggeration = 22:1. Locations are shown in Figure 16. Bottom panel shows the interpretation of crustal structure along line A-B. The light gray and black lines represent the seafloor and top of igneous crust, respectively. The intermittent black lines show the MCS reflection Moho. The heavy dark gray line shows the Moho traced from OBS refraction data (Korenaga and Sager, 2012). The light gray line shows the predicted Moho from Airy isostasy. Vertical exaggeration = 7:1. Location shown in Figure 16.

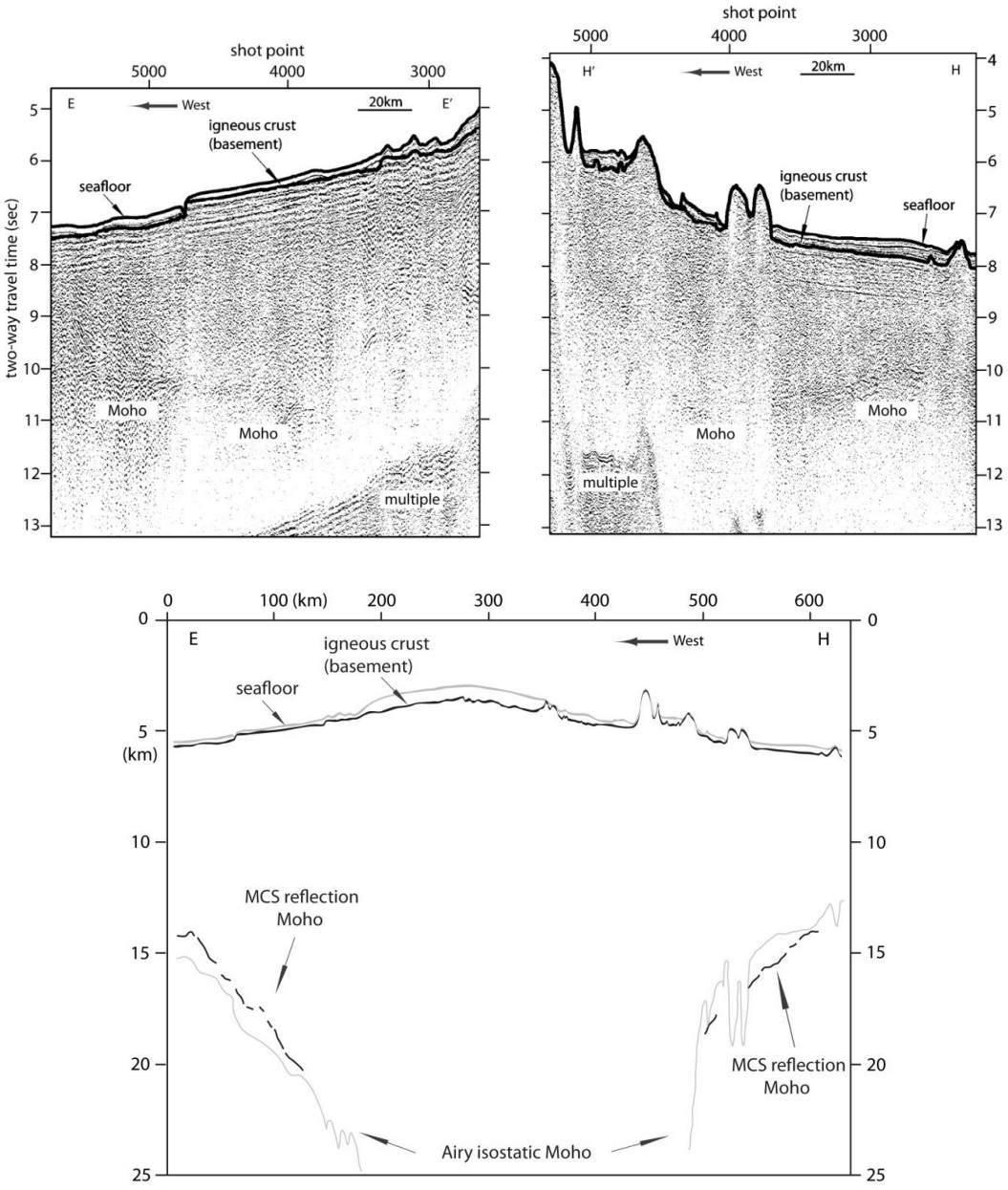

Figure 20. MCS reflection images and crustal structure of line E-H, on the north side of Tamu Massif. Top panel shows MCS reflection images for line segments E-E' and H-H', which display the Moho reflection. Locations are shown in Figure 16. Bottom panel shows crustal structure of line E-H. Vertical exaggeration = 20:1. Location shown in Figure 1. Other plot conventions as in Figure 19.

Line E-F (Figure 21) crosses the south flank of Tamu Massif. On the eastern side of line E-F, Moho reflectors show strong continuity and high amplitude at depths between 9 and 10 sec TWTT. Rough surface topography (a large fault at SP 6500) causes a 10 km gap in the Moho reflector and the Moho reflector disappears again around the time of the multiples (~11 sec TWTT; 22 km). On the western side of line E-F, the Moho reflectors are not as continuous, but segments can be connected to interpret a horizon that descends (~5^{o}) towards the center of the massif.

Line C-F, which crosses a low ridge at the southern distal flank of the massif, shows a discontinuous Moho reflector (Figure 22). As before, the Moho does not appear beneath several secondary cones, which may scatter the penetrating seismic signal. Nevertheless, between the cones, a few Moho reflectors are observed at SPs 2500, 4200, 4800.

Composite profile C-I-G-D (Figure 23), runs along the axis of Tamu Massif from the southwestern end to the northeastern end. Only the outer two segments display the Moho reflection. In segment C-I, at the southwest end of Tamu Massif, the Moho descends (~3^{o}) toward the center of the massif, reaching a depth of 10.5 sec TWTT (16 km) and disappearing around the multiples. In segment G-D (Figure 23), at the northeastern end of Tamu Massif, the Moho deepens rapidly (~10^{o}) towards the center of the massif at SP 3600, reaching a depth of 11.5 sec TWTT (21 km).

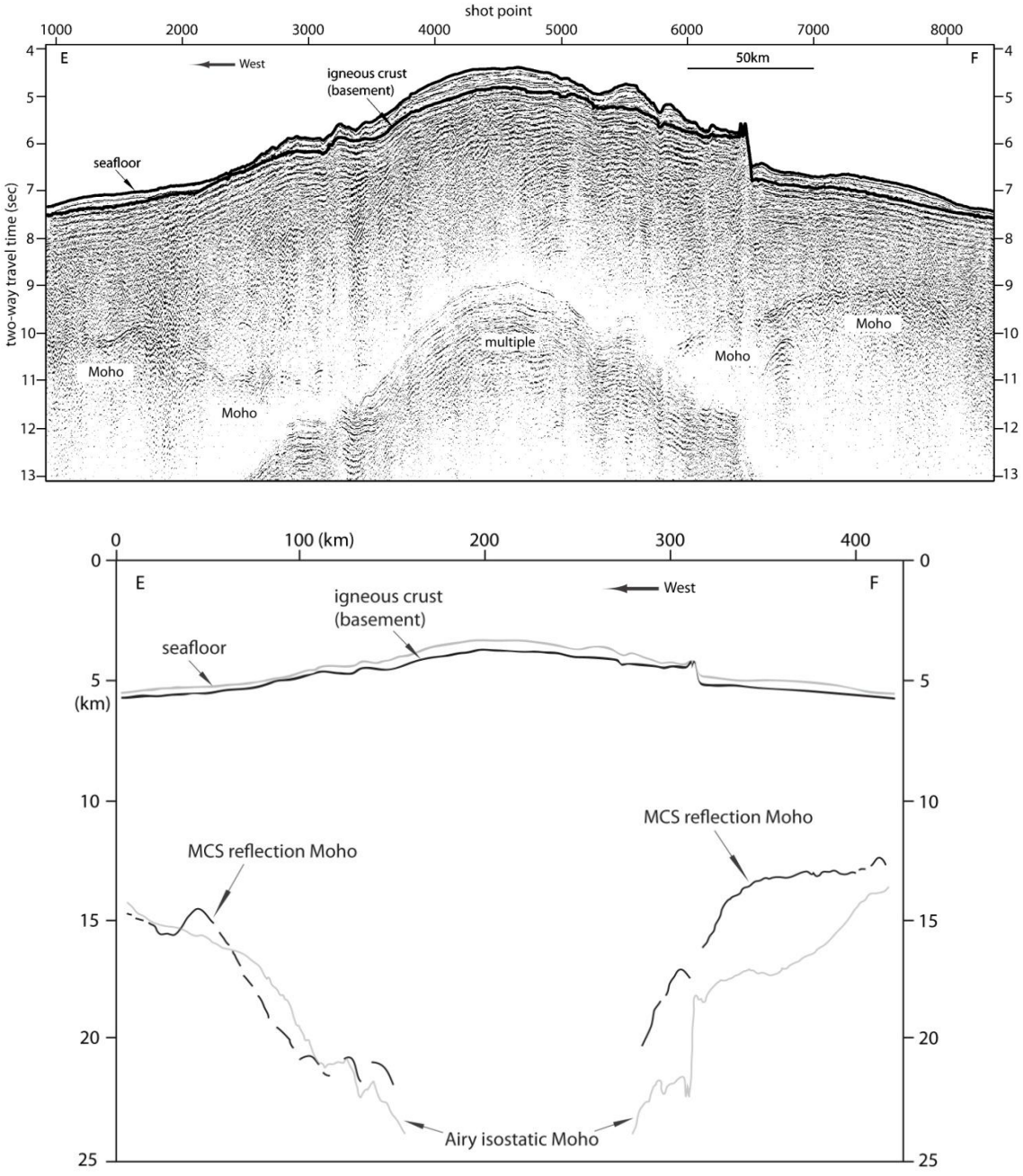

Figure 21. MCS reflection image and crustal structure of line E-F, on the south flank of Tamu Massif. Top panel shows MCS reflection image. Bottom panel shows crustal structure. Vertical exaggeration = 12:1. Location shown in Figure 16. Other plot conventions as in Figure 19.

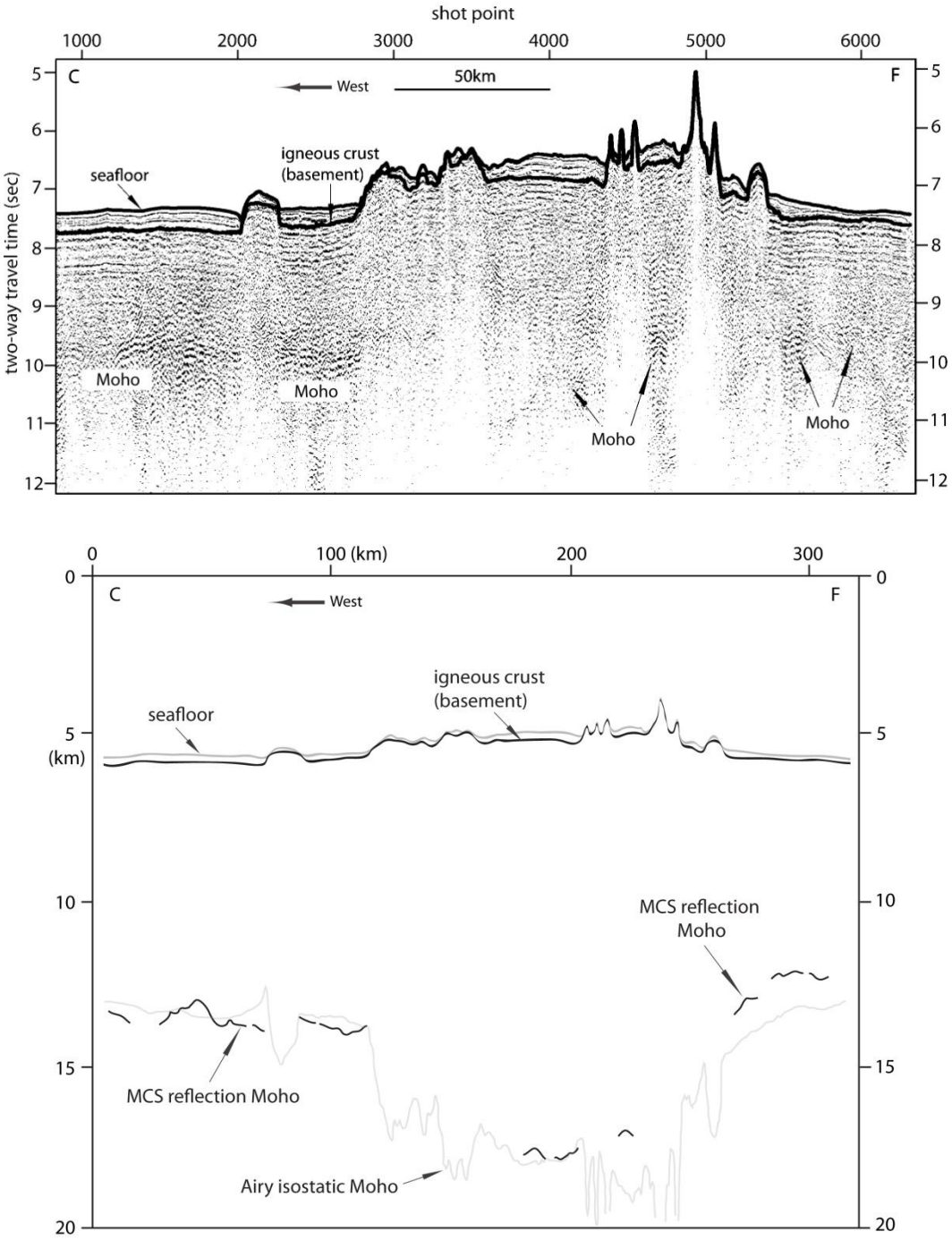

Figure 22. MCS reflection image and crustal structure of line C-F, on the distal south flank of Tamu Massif. Top panel is MCS reflection image. Bottom panel shows crustal structure. Vertical exaggeration = 14:1. Location shown in Figure 16. Other plot conventions as in Figure 19.

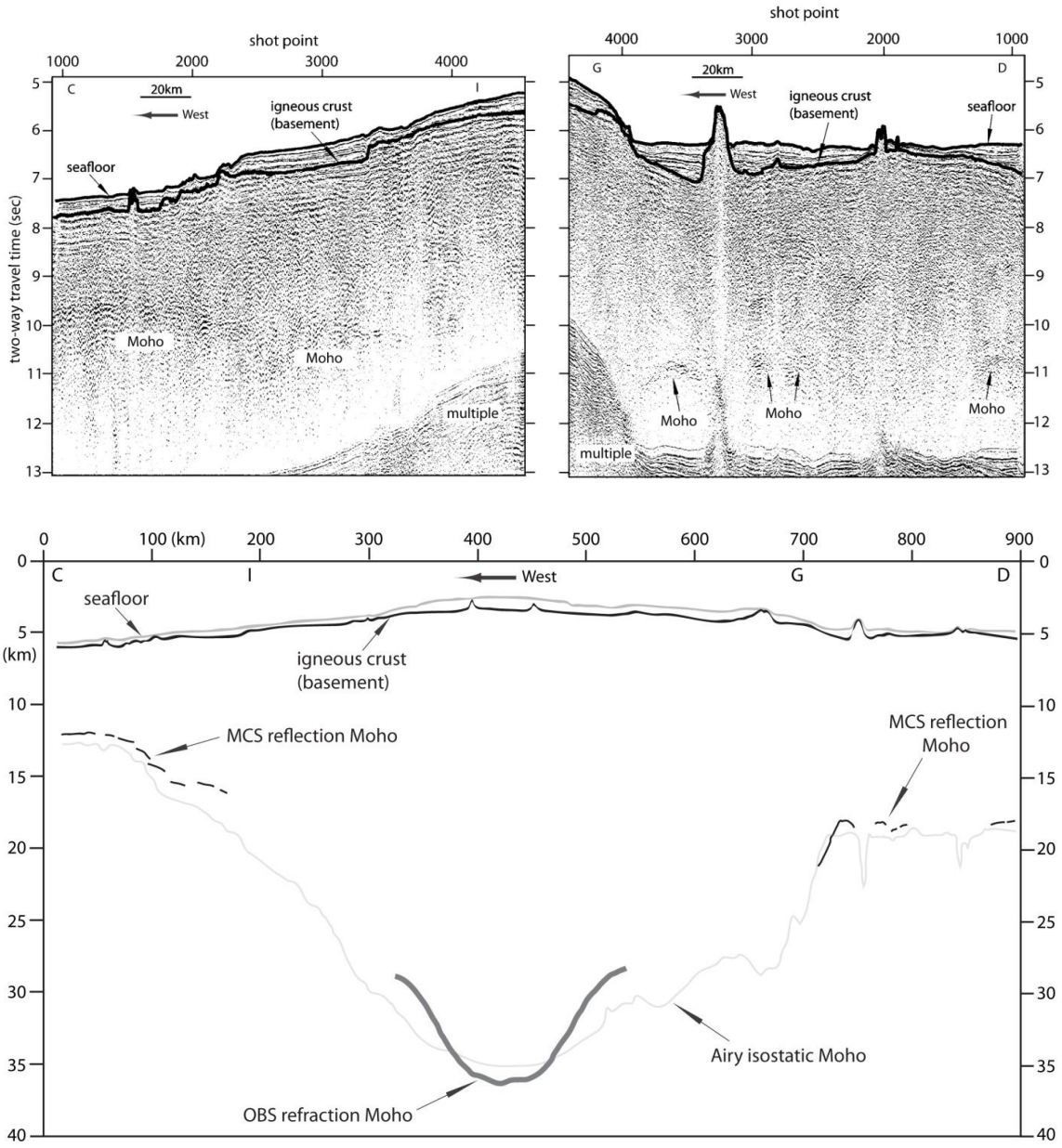

Figure 23. MCS reflection images and crustal structure of line C-D, along the axis of Tamu Massif. Top panel shows MCS reflection images of segments C-I and G-D, which display the Moho reflection. Segment C-I is located on the south flank, whereas segment G-D is located on the north flank. Locations are shown in Figure 16. Bottom panel shows crustal structure of line C-D. Letters at top refer to segment endpoints. Vertical exaggeration = 12:1. Location shown in Figure 1. Other plot conventions as in Figure 19.

3.4.2.2 Ori Massif

Beneath Ori Massif, like Tamu Massif, the Moho reflection is observed on Line M-D at the lower flanks (Figure 16). In Figure 24, two segments of line M-D (M-M' and D-D') on the western and eastern ends of Ori Massif respectively, show a few weak Moho reflectors that dip (~5^{o}) towards the center of the Massif and disappear around the multiples. The continuity of the Moho is different on either side with those in segment M-M' being more continuous than those in segment D-D'.

Line M-L, which crosses the southwestern flank of Ori Massif and the Helios Basin, displays Moho reflectors on both ends of the line (Figure 25). At the western end of line M-L, the Moho declines (~3^{o}) towards the center of Ori Massif, reaching a depth of ~11.3 sec TWTT (~22.5 km) before fading around the multiples. Interestingly, unlike other profiles, the symmetric Moho reflection is missing (or hard to see) on the east side of Ori Massif, even though the surface topography is smoother than the west side and less scattering would be expected. Additionally, a strong Moho reflector dips (~5^{o}) away from Ori Massif at the eastern side of the basin beneath the north flank of Tamu Massif. This reflector dips towards the center of Tamu Massif, so it is likely part of the root of Tamu Massif.

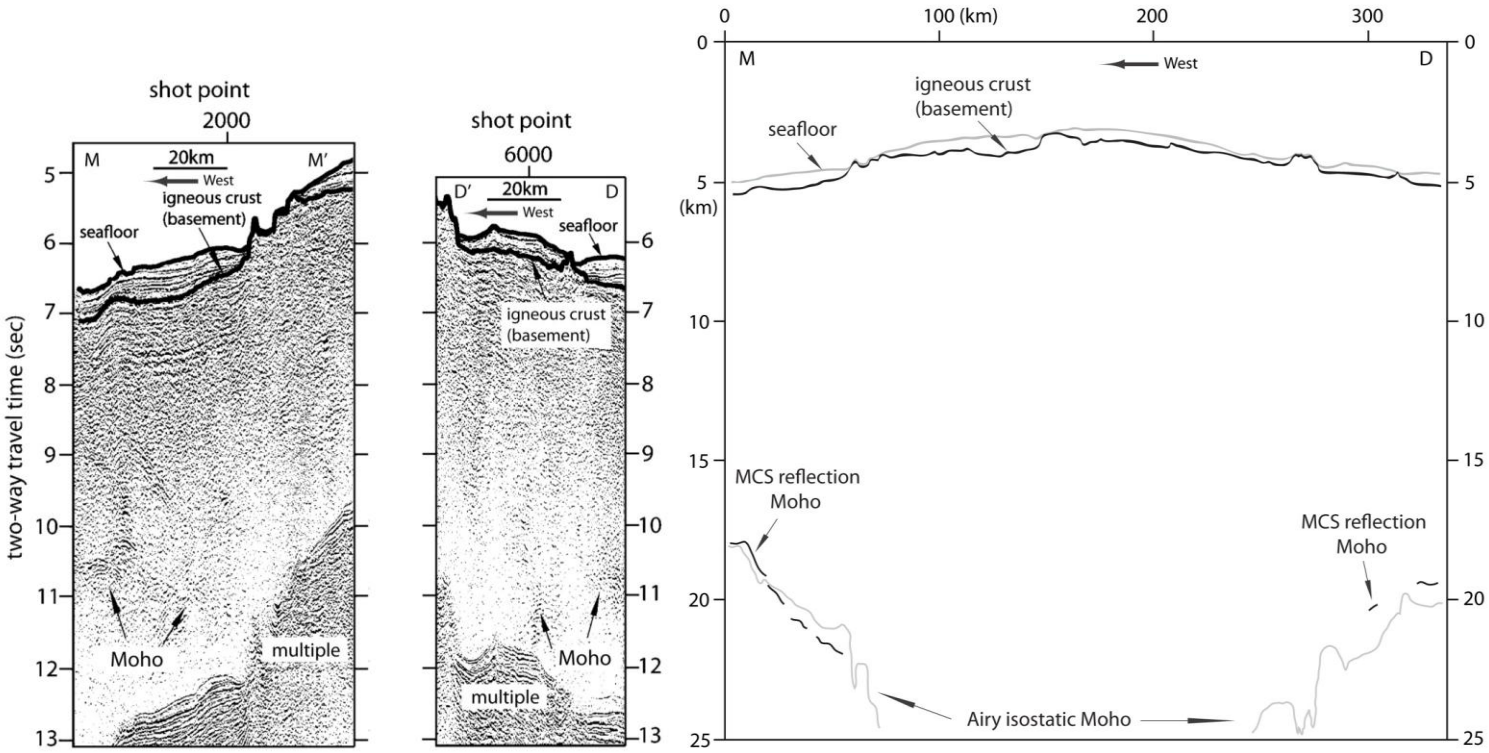

Figure 24. MCS reflection images and crustal structure of line M-D, across Ori Massif. Top panel shows MCS reflection images of segments M-M' and D-D', which display the Moho reflection. Locations are shown in Figure 16. Bottom panel shows crustal structure of line E-H. Vertical exaggeration = 14:1. Location shown in Figure 1. Other plot conventions as in Figure 19.

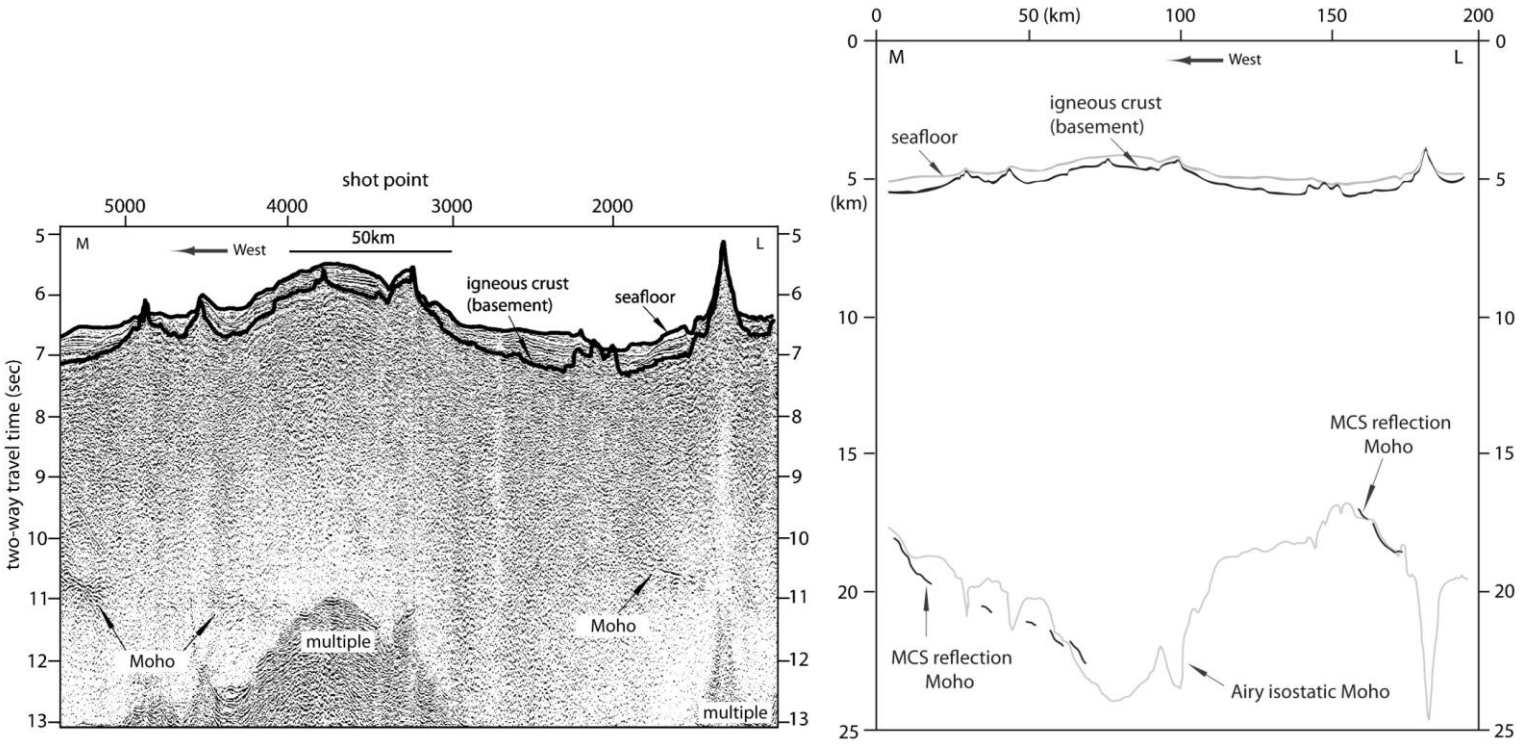

Figure 25. MCS reflection images and crustal structure of line M-L, on the southwest flank of Ori Massif and across Helios Basin. Top panel shows MCS reflection images. Bottom panel shows crustal structure. Vertical exaggeration = 9:1. Location shown in Figure 16. Other plot conventions as in Figure 19.

.

3.4.3 Composite crustal structure

MCS reflection images do not show the Moho at the center of Tamu and Ori massifs. Fortunately two refraction lines (lines 1 and 2; Figure 16), crossing the center of Tamu Massif, record the crustal structure beneath the thickest part of the massif (Korenaga and Sager, 2012). The MCS data are complementary and I can combine them to generate a composite Moho profile to show a more complete crustal structure of Shatsky Rise.

Line A-B across the SW-NE-oriented axis of Tamu Massif has refraction line 1 at its center, overlapping reflection Moho segments A-A’ and B-B' on the lower flanks (Figure 16). I must compute the reflection Moho depth from the observed TWTT of Moho reflectors using a plausible velocity function. I assumed average water and sediment column velocities of 1500 m/s and 2000 m/s, respectively and then tried various average velocities for the igneous crust. A velocity of 6500 m/s for the igneous crust gave the best match between the reflection and refraction Moho (Figure 19). This average crustal velocity is consistent with the velocity-depth profile from Korenaga and Sager (2012).

The 650-km-long composite profile A-B (Figure 19) yields a complete picture of the Moho structure of Tamu Massif. Thick crust (~30 km thick) exists at the center of the massif, thinning to normal thickness (~7 km) on both flanks beneath adjacent seafloor. The maximum crustal thickness occurs beneath the shield summit at 490 km in Figure 19 (see Sager et al., 2013; refer to Chapter II). Although Toronto Ridge (at 410 km) is the shallowest basement peak, it does not correlate with the thickest part of the

crust, consistent with the interpretation that Toronto Ridge is a late stage feature and the shield summit was the center of shield-building volcanism (Sager et al., 2013; refer to Chapter II). Although the eastern end of line A-B is truncated at transitional thickness crust (~9 km thick), the western end stretches into the surrounding basin where the Moho is nearly flat (Figure 19) with a thickness that is consistent with normal oceanic crust (White et al., 1992).

Another composite section is created with refraction and reflection data along line C-I-G-D, a ~900 km profile along the SW-NE axis of Tamu Massif (Figure 16). On this line, the two data sets do not overlap, so I used the same velocities as before to determine reflection Moho depth. There are two MCS reflection segments (C-I and G-D) displaying the Moho at each end of the profile and a short refraction line (Line 2) in the middle. These data sets are separated by gaps of ~200 km. In spite of large gaps in between the reflection and refraction Moho segments, this profile (Figure 23) shows a similar crustal structure to line A-B (Figure 19). The thickest crust occurs at the center of the massif and becomes thinner towards both sides. The southwest end probably reaches normal seafloor with crustal thickness of ~6-7 km (Figure 23). On the northeast side of the profile, the minimum crustal thickness is ~13 km, indicating thickened crust in the interior of the plateau, which is similar to other MCS profiles (e.g. lines E-H and E-F).

3.4.4 Airy isostatic Moho

Although the Airy isostatic Moho was calculated using a simple model of oceanic crust and mantle densities, it matches the seismic reflection and refraction Moho

in most places (Figures 4-10). Two notable exceptions are the summit of Tamu Massif along line A-B (Figure 19) and the eastern half of line E-F (Figure 21). This general agreement shows that the observed seismic and inferred Moho locations support the idea that the depth of this horizon is determined by isostasy. The mismatch at the summit of Tamu Massif on line A-B (Figure 19) occurs because of a combination of several factors. The deepest Moho is located beneath the broad, buried eastern summit at 490 km (Figure 19), an observation consistent with the interpretation that this summit was the center of shield-building eruptions (Sager et al., 2013). The shallower summit of Toronto Ridge (at 410 km in Figure 19) is not reflected by deeper Moho, likely because this ridge is a secondary volcanic feature formed long after the formation of the Tamu Massif shield (Sager et al., 1999; 2013) and is thus supported mostly by lithospheric strength. In addition, the thick sediment pond (maximum ~1 km thickness) located between ~430 and 480 km, causes an overestimation of root depth because of the simple isostasy model. Moreover, the wavelength of the calculated and observed refraction Moho profiles is different beneath the center of Tamu Massif: the refraction Moho displays a slightly steeper slope and broader expanse than the calculated Moho (Figure 19). This may occur because of lateral changes in density, for example with the massif becoming denser toward the center or the root becoming less dense. Another mismatch between the calculated Moho and observed seismic Moho occurs on the eastern half of line E-F (Figure 21). The calculated Airy isostatic Moho fits the reflection Moho on the western side but not the eastern side, where the calculated Moho is 2-2.5 km too deep.

This difference implies that the density structure must be different on the eastern side, even though the model works well elsewhere.

3.5 Discussion

3.5.1 Comparison between normal CDP stack and CVS

Marine multichannel seismic (MCS) reflection data are usually corrected for normal moveout (NMO) using semblance velocity analysis, with signals stacked to form CDP. It is often difficult to obtain a reliable velocity analysis for a deep seismic reflection like the Moho, because it is weak in amplitude. Constant velocity stack (CVS) is an alternative technique in which a constant, average velocity is used for stacking signals throughout the crust. The optimum stacking velocity is determined by trial and error, scanning a range of velocities to find the one that produces the clearest Moho reflection image. For my data, this velocity was 4000 m/s (Figure 17). In comparison with a standard semblance-velocity CDP stack (Figure 18), the CVS method yields clearer Moho reflections. Although the CVS velocity of 4000 m/s is obviously too high for sedimentary section, my imaging focus in this chapter is the Moho, so the poorly-corrected sediment reflection can be neglected.

3.5.2 Moho reflectors

The Moho represents an interface with significant contrast in elastic properties: velocity and density (Rohr et al., 1988; Holbrook et al., 1992), which may result in observable reflectivity in deep penetrating seismic reflection profiles. For the MCS

reflection data presented here, the Moho reflectors are observed on the lower flanks of Tamu and Ori Massifs and on the surrounding seafloor, whereas the Moho reflectors are not observed beneath the central parts of the massifs, where the crust is thickest (Korenaga and Sager, 2012). The absence of Moho reflections in the central areas may result from two factors. One explanation is that strong multiples mask the Moho reflectors near the center of the massifs (e.g. Figures 4, 6, 10). Another is that the seismic signal is attenuated with greater depth in the crust and the return is too weak to be observed.

MCS reflection data show that the Moho reflectors are highly variable in length (continuity), shape (character) and strength (amplitude). The Moho reflectors have variable length, ranging from several to tens of kilometers; variable shape, appearing flat, gently curved, or sometimes highly curved (mounded). Moho reflectors also have variable strength, ranging from sharp and strong to weak or absent. This Moho variability is seen in all the Moho reflectors beneath Tamu and Ori massifs and is similar to the character observed both at mid-ocean ridges and over normal oceanic crust (Mutter and Carton, 2013). Two explanations for Moho variability are suggested by Mutter and Carton (2013). One is that the real Moho structure varies from a sharp vertical discontinuity to a broad gradient zone. This explanation sounds very plausible because the Moho by its nature could be an interface with an abrupt change in elastic properties that generate strong seismic reflection recording its real structure, and the Moho also could be a thick transition zone that have gradually increase in elastic properties leading to weak or absent reflection (Collins et al., 1986; Nedimovic et al.,

2005; Singh et al., 2006). The other explanation given by Mutter and Carton (2013) is that scattering in the crust results in variable imaging conditions at the Moho level, so that the observed variation is apparent and not the real Moho structure. Rough topography or layering in the upper crust may scatter the penetrating acoustic energy so that the deeper structure is poorly imaged. In the Shatsky Rise MCS reflection profiles, I often observe that the Moho is absent beneath secondary cones (e.g. Figure 22). Where the upper crustal topography is smooth, I often observe continuous Moho reflectors. Although this correspondence is generally true for Shatsky Rise MCS data, there are exceptions. For instance, at the both ends of Figure 22, the upper crustal topography is horizontally layered, but no Moho reflectors are observed (see SP 1100 and 5800). Scattering effects at the top of the oceanic crust, therefore, cannot explain this absence of the Moho reflector. In the lower crust, rough topography of Moho itself may scatters acoustic energy as well, resulting in the loss of Moho reflectors (Nedimovic et al., 2005).

Moho reflectors are discontinuous with gaps of a few kilometers in between, but individual reflectors can be connected into a long horizon by following the trend, yielding a reflection that is piecewise-continuous. The piecewise-continuous pattern of Moho reflectors is similar to intra-basement reflectors (representing lava flows) observed in the upper crust of Tamu and Ori massifs (Sager et al., 2013; refer to Chapter II).

In addition, Moho reflectors closer to the center of the massifs are weaker. Aside from the previous explanations that shallow multiples mask the deep reflection at the center of the massifs and the Moho is deeper in these areas so there is more attenuation

of seismic energy with depth, this strength/amplitude difference may be caused by more melting close to the massif center, which weakens or destroys the Moho reflectivity (Collier et al., 1994). Shatsky Rise massifs are central volcanoes (Sager et al., 2013; refer to Chapter II), so the volcanic source is at the massif center, which may lead to more melting at the massif center than the flanks. Melting at the massif center may destroy the sharp vertical discontinuity of Moho or make it a broad gradient zone, resulting in weak or absent Moho reflectors to be observed.

3.5.3 Structure of the Moho

The structure of the Moho on Tamu and Ori massifs is similar in all MCS reflection profiles. The Moho is observed at normal depths (~7 km crustal thickness) beneath adjacent abyssal crust and dips (~3-5^{o}) towards the center of the massifs. That is to say, the massif crust thickens with the elevation of seafloor from the surrounding normal oceanic crust. Line A-B (Figures 1, 4) is a remarkable profile across the center of Tamu Massif showing the complete Moho structure from combined MCS reflection and refraction data. The Moho begins horizontally, with a thickness of ~7 km beneath the surrounding normal seafloor and dips toward the center of the massif, reaching a maximum crustal thickness of ~30 km.

The crustal structure of Tamu and Ori massifs is consistent with Airy isostasy, because the observed seismic Moho matches the predicted Airy isostatic Moho along most of the seismic lines (e.g. Figures 4, 8, 9). This observation confirms inferences from gravity data, which show small free air anomalies over Shatsky Rise (and other

oceanic plateaus) (Sandwell and Mackenzie, 1989). Moreover, from drilling results and seismic data, Tamu and Ori massifs appear to be immense volcanoes (Shipboard Scientific Party, 2001; Koppers et al., 2010; Sager et al., 2010, 2011; Sager et al., 2013; refer to Chapter II). As such massive igneous edifices formed at a thin, young lithosphere with little rigidity near a triple junction (Sager et al., 1988; Nakanishi et al., 1999) and would be expected to overwhelm the slight strength of the lithosphere (Watts et al., 1984). To support these massive volcanoes, deep crustal roots are required to maintain isostatic equilibrium. Thus the great bulk of Tamu and Ori Massifs is located deep within the crust, whereas the surface expression is a broad, low mound (Sager et al., 2013; refer to Chapter II).

One interesting mismatch between the MCS reflection Moho and Airy isostatic Moho is observed on line E-F (Figure 21). The discrepancy implies something must be different on the eastern side of the line from the western side, probably either the density contrast or the Moho structure difference. The Airy isostatic Moho is simply calculated and does not account for density variations within the crust or upper mantle, thus it is an inadequate model for lateral variations in density. Besides variable density structure, two other explanations could explain the difference in terms of Moho structure. One is related to extra buoyancy on the eastern side. Melt extraction might have been inefficient in the region where the eastern end of the line is close to the location of the beginning of Shatsky Rise formation (Figure 16), because melt migration might have had to struggle its way through and could have been inefficient. Another possibility is that what is

identified as the MCS reflection Moho on the east half of the line is actually the base of the pre-existing crust, and there may be crustal underplating beneath it.

3.6 Conclusions

Deep penetrating marine multichannel seismic (MCS) reflection data over the two largest massifs (Tamu and Ori) within Shatsky Rise oceanic plateau were reprocessed by Constant Velocity Stack (CVS), instead of the normal CDP stack, computed by standard semblance velocity analysis. Clearer seismic reflection images of the Moho were produced by CVS at a constant stacking velocity of 4000 m/s.

MCS reflection data show the Moho reflectors are highly variable in: length, ranging from several to tens of kilometers; shape, ranging from flat to curved or mounded; and strength, ranging from sharp and strong to weak or absent. This variability is similar to other Moho observations in the oceans, likely resulting from a combination of changes Moho structure and variable imaging conditions owing to the scattering effects in the crust. The Moho reflectors closer to the center of the massifs are weaker, probably because of greater attenuation with depth, masking by multiples, or lower Moho reflectivity due to more melting at the massif center.

Moho reflectors are discontinuous, but individual reflectors can be connected into a long horizon by tracing their trend, appearing to be piecewise-continuous. The piecewise-continuous Moho reflectors are shallow (~7 km) beneath normal crust near the distal flanks of Shatsky Rise massifs and dips (~3-5^{o}) downward towards the center of the massifs from all directions, indicating an overall structure of crustal thickening at

Shatsky Rise. Moho reflectors can be seen in MCS images up a thickness of ~17 km. Moho depths from MCS reflection data can be matched with those from refraction data, showing that the dip continues toward the middle, reaching maximum thickness of ~ 30 km at the center.

Shatsky Rise crustal structure is consistent with the Moho topography of isostatically compensated crustal structures, which is why the plateau exhibits a small free-air gravity anomaly signature. Shatsky Rise was built on young oceanic lithosphere with little rigidity, so the plateau formed in isostatic equilibrium with a deep crustal root.

CHAPTER IV

MORPHOLOGY OF SHATSKY RISE OCEANIC PLATEAU FROM HIGH-RESOLUTION BATHYMETRY

4.1 Overview

High resolution multi-beam sonar data collected on *R/V Marcus G. Langseth* during cruises MGL1004 and MGL1206 are combined with previous bathymetry data to produce an improved bathymetric map of Shatsky Rise oceanic plateau. Because most of Shatsky Rise is covered with only a thin sedimentary layer, the bathymetry reflects the primary shape and structure of the plateau. Bathymetry data show that two massifs within Shatsky Rise are immense central volcanoes. Tamu Massif is a huge, slightly elongated, and dome-like volcanic edifice with gentle flank slopes declining from a central summit. Ori Massif has similar morphology but is square shape and smaller in area. The massifs are surrounded by magnetic lineations and fracture zones, implying that their morphology may have been controlled by ridge tectonics. However, few faults are seen on the massif flanks, contrary to expectations of ridge-related faults controlling morphology. A small number of down-to-basin normal faults are observed on the western flanks of the massifs, but these faults do not parallel the magnetic lineations, indicating that these faults are probably not related to spreading ridge faulting. Moreover, these faults are observed only on one side of the massifs. This is contrary to expectations from a mechanism of differential subsidence of the massif center, which should lead to faulting on all sides of these volcanoes. Multi-beam data show many

small cones on the massif flanks that are too small to be resolved in the satellite predicted bathymetry and would otherwise be poorly represented. These are volcanic cones with different shapes and sizes and are widely-distributed on Shatsky Rise massifs, which implies small magma sources scattered across the surface of the volcanoes. These numerous secondary cones probably come from late-stage volcanism, which can either be in the form of lava flows or explosive volcanism. Erosional canyons occur on the flanks of Shatsky Rise volcanoes due to mass wasting and display evidence of down-slope sediment movement. These canyons are likely formed by sediments spalling off the edges of summit sediment cap. Moreover, some erosional channels exist along the basal contours of some ridges and probably result from bottom current scouring against one side or around the ridges.

4.2 Introduction

Oceanic plateaus are extensive submarine mountains, and many are basaltic volcanic edifices (Large Igneous Provinces or LIPs) representing massive eruptions of material from the mantle (Coffin and Eldholm, 1994). Oceanic plateau bathymetry is important as a constraint of edifice structure, providing clues about plateau evolution, volcanic processes, regional tectonics, and mantle behavior. Nevertheless, for most oceanic plateaus, morphology is poorly mapped because of a combination of remote location, sediment cover, and large size. Oceanic plateaus often with nearly flat tops and low slopes (Coffin and Eldholm, 1994), but their shapes in plan views can be irregular. Some plateaus have rounded shapes (e.g. Ontong Java Plateau and Magellan Rise),

whereas some are angular (e.g. Manihiki Plateau and Hikurangi Plateau). Although large scale oceanic plateau morphology is often known from scattered bathymetry soundings and satellite altimetry-based bathymetry estimates, most contain smaller features, such as small seamounts, secondary cones, canyons, and faults, which are poorly sampled.

How oceanic plateaus form is a subject of lively debate. While there are number of different models proposed to explain their formation, none explains all observed features (Foulger, 2007). One such explanation is the plate model, in which volcanic edifices form where extension exists in the lithosphere (e.g. Hilde et al., 1976; Anderson et al., 1992; Saunders, 2005; Foulger, 2007). Another model is the plume head hypothesis, in which a nascent plume ascends from deep in the mantle and arrives at the base of lithosphere to form an oceanic plateau (e.g. Richards et al., 1989; Mahoney and Spencer, 1991; Duncan and Richards, 1991; Coffin and Eldholm, 1994; Courtillot et al. 2003; Campbell, 2006). In addition, some authors have suggested that oceanic plateaus formed from a bolide impact (Rogers, 1982; Alt et al., 1988; Ingle and Coffin, 2004), but there is little evidence to support this model.

Shatsky Rise is interesting among oceanic plateaus because it is one of the largest and it has characteristics that fit both the plume head and the plate formation hypotheses (Sager, 2005). Its eruptions were associated with a triple junction (Sager et al., 1988; Nakanishi et al., 1999) but its morphology suggests that it began with an initial massive eruption (Sager et al., 1999) as is expected of a plume head eruption. This unique combination spurred several recent investigations. The Ocean Drilling Program (ODP) and Integrated Ocean Drilling Program (IODP) cored igneous basement on Shatsky Rise

at six sites, indicating that massive volcanic eruptions built the largest and oldest edifice, Tamu Massif (Shipboard Scientific Party, 2001; Koppers et al., 2010; Sager et al., 2010; 2011). The seismic vessel R/V Marcus G. Langseth visited the southern half of Shatsky Rise to acquire modern deep-penetration seismic data (cruises MGL1004, MGL1206). Refraction seismic tomography from the seismic study was reported in Korenaga and Sager (2012). The shallow crustal structure of the southern Shatsky Rise from multichannel seismic reflection data were interpreted in Sager et al. (2013) and Chapter II and the deep crustal structure were discussed in Chapter III. In this study, I present an updated bathymetry map of the southern Shatsky Rise, based on new bathymetry data collected by multibeam sonar from the R/V Marcus G. Langseth, combined with previous bathymetry data, and discuss the implications of the new map. Because most of Shatsky Rise is covered with only a thin sedimentary layer, the bathymetry reflects the primary shape and structure of the plateau.

4.3 Geologic background

Shatsky Rise is located ~1600 km east of Japan (Figure 26). Its summits reach depths of 2-3 km, with surrounding seafloor at a depth of ~5.5 to 6.0 km. The primary features of Shatsky Rise are three very large volcanic constructs (massifs), named Tamu, Ori, and Shirshov, arranged in a northeast trend (Sager et al., 1999). The edifices are broad, domal features with gentle flank slopes of ~0.5 °-1.5 °(Sager et al., 2013; Chapter II). Both Ori and Shirshov massifs have nearly circular shapes, but Tamu Massif is elongated along the trend of the rise. Tamu Massif, the oldest and largest of the three,

has a volume of ~2.53 $\times 10^6\ km^3$, whereas the volumes of Ori and Shirshov are 0.69 x 10^6 and 0.65 $\times 10^6 \text{km}^3$, respectively (Sager et al., 1999). Papanin ridge lies north of Shirshov Massif and shares the same northeast trend as the rest of the rise. It bends near 45 ℃N, changing trend to southeast, perhaps connecting with Hess Rise (Bercovici and Mahoney, 1994; Sager et al., 2005). In total, the area of Shatsky Rise is ~4.8 $\times 10^5 km^2$ - roughly the same as that of California or Japan. However, this may have been larger in the past, as it is possible that part of the rise was rafted away on other plates and later subducted into the mantle (Nakanishi et al., 1999).

Because Shatsky Rise formed before the Cretaceous Normal Superchron, magnetic lineations are present and contain information about the plateau's tectonic history. Maps of magnetic anomalies show that Shatsky Rise sits at the intersection of two magnetic lineation sets: the Japanese lineations trending northeast and the Hawaiian lineations trending northwest (Larson and Chase, 1972; Hilde et al., 1976; Nakanishi et al., 1999). At about the time of M21 (149 Ma), the Pacific-Izanagi-Farallon triple junction jumped ~800 km east to the location of Tamu Massif (Nakanishi et al., 1999). The triple junction migrated northeast along the axis of the rise and the volcanic edifices were created in its wake. Gravity data imply that the massifs were formed on young lithosphere (Sandwell and McKenzie, 1989), so the magnetic lineations indicate the order of formation. Tamu massif, the largest, formed first, followed by Ori and Shirshov massifs, and finally Papanin ridge (Nakanishi et al., 1999). A radiometric age of 144.5 ±0.8 Ma from Site 1213 on Tamu Massif (Mahoney et al., 2005), nearly matches that of the nearby magnetic lineations (Sager, 2005), confirming that the massifs formed near

the spreading ridges. Magnetic anomalies M21(149 Ma) and M1(126 Ma) bound Shatsky Rise to the south and north, respectively (Nakanishi et al., 1999; using the time scale of Gradstein et al., 2004), implying that even though individual edifices may have formed rapidly (Sager and Han, 1993), the plateau as a whole formed over about 21 million years.

Shatsky Rise has never been close to land so the sediment cap is largely pelagic in nature (Sliter and Brown, 1993). Sediment on the flanks is less than 500 m in thickness (Houtz and Ludwig, 1979; Ludwig and Hutz, 1979) and some places it is absent likely as a result of erosion (Ewing et al., 1966; Neprohnov et al., 1984; Sliter and Brown, 1993). On the summits, where the topography is generally flat, sediment collects into ponds up to ~1.2 km thick (Ewing et al.,1966; Zdorovenin et al., 1972; Neprohnov et al., 1984; Karp and Prokudin, 1985; Khankishieyeva, 1989; Sliter and Brown, 1993; Sager et al., 1999). Core samples indicate that sediments are mostly Cretaceous pelagic carbonates that were deposited when the summits were above the calcite compensation depth and closer to the equator (Sliter and Brown, 1993).

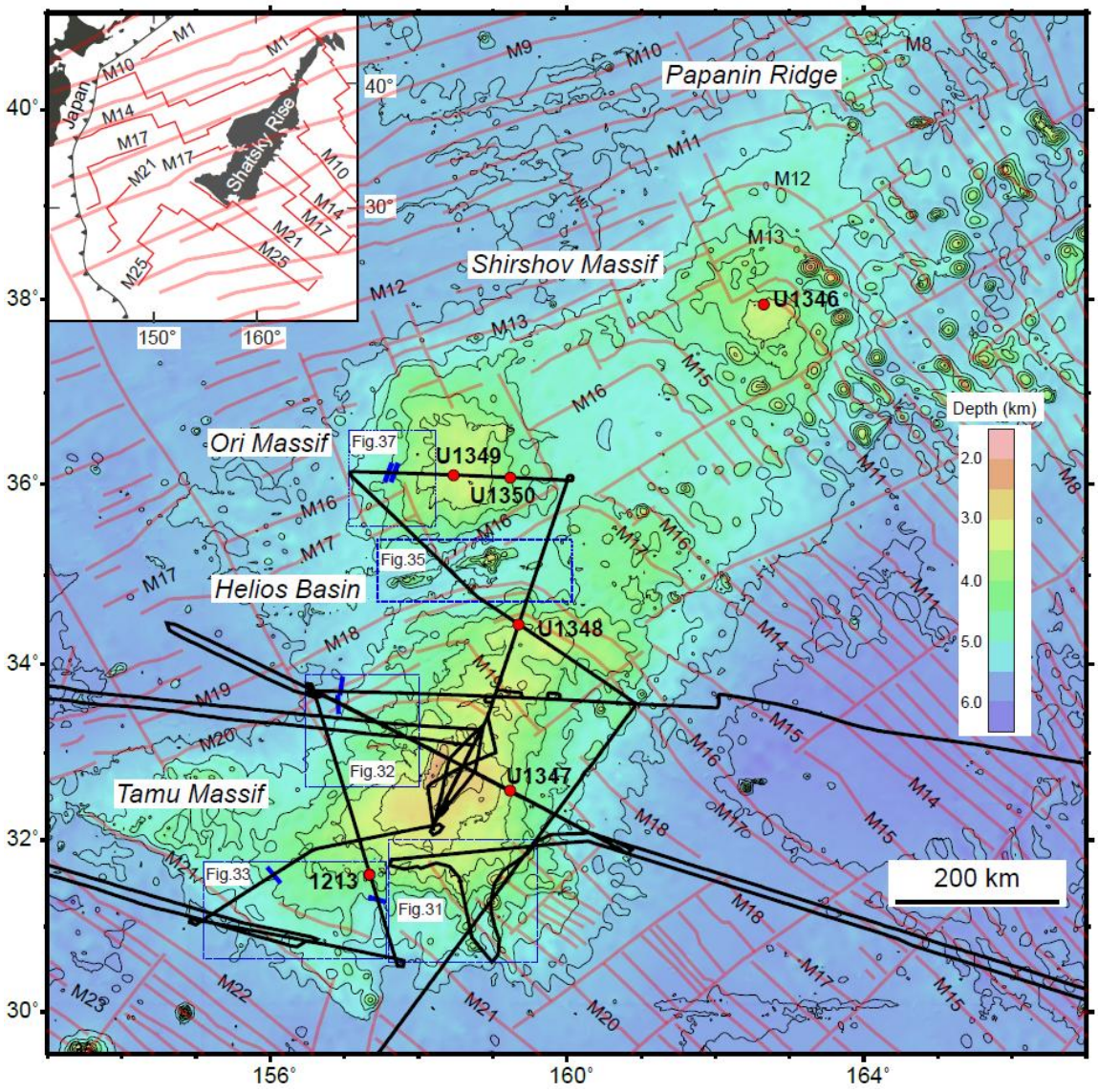

Figure 26. Bathymetry and tectonic map of Shatsky Rise with multi-beam track lines from *R/V Marcus G. Langseth* cruises MGL1004 and MGL1206. Bathymetry is from satellite-predicted depths with 500-m contours (Smith and Sandwell, 1997). Heavy red lines show magnetic lineations with chron numbers labeled for reference (Nakanishi et al., 1999). Heavy black lines show multi-beam track lines collected by *R/V Marcus G. Langseth*. Filled red circles show locations of the ODP and IODP drill sites mentioned in the text. Inset depicts the location of Shatsky Rise relative to Japan and nearby subduction zones (toothed lines) and the wider magnetic pattern. Heavy blue tick marks show the locations of large down-to-basin faults seen on multi-beam bathymetry and seismic profiles (Chapter II). The fault strikes are estimated from multi-beam bathymetry. Dashed blue boxes denote the areas shown in Figures 31-33, 35 and 37.

Basaltic basement rocks were recovered from all Shatsky Rise massifs. Basalts sampled from Tamu Massif contain massive flows up to ~23 m thick (at ODP Site 1213, Shipboard Scientific Party, 2001; Koppers et al., 2010, and IODP Site U1347, Sager et al., 2010; 2011) interlayered with pillow lavas. The massive flows are analogous to sheet flows in continental flood basalt provinces (Kesthelyi and Self, 1998) and are evidence of massive volcanic eruptions with high effusion, similar to what is seen in continental flood basalts (Jerram and Widdowson, 2005; Bryan et al., 2010). As the massifs become younger and smaller, thinner and less massive basalts, and more pillow basalts are found on Ori Massif (at IODP Sites U1349 and U1350) and Shirshov Massif (at IODP Site U1346), implying construction of these edifices by submarine eruptions with more modest effusion rates (Sager et al., 2010; 2011). This shift implies that a highly effusive eruption at Tamu Massif was followed by waning volcanic eruptions at Ori and Shirshov massifs. In addition, Volcaniclastics were found at IODP Site U1348 on Tamu Massif and at Site U1349 on Ori Massif, which may be associated with explosive volcanism occurring in shallow water (Sager et al., 2010; 2011).

The evidence from sediment cores implies that the summits of the three massifs within Shatsky Rise were in shallow water or at sea level. For example, IODP Sites U1346 on Shirshov Massif and U1347 on Tamu Massif contain foraminifera that lived water less than 500 m deep. Similarly, Site U1348 on Tamu Massif yielded shallow water fossils and Site U1349 on Ori Massif yielded shallow water carbonates and a possible paleosol, which imply that the site was right at sea level. Paradoxically, seismic

reflection profiles do not show any evidence of subaerial erosion for Shatsky Rise, implying that the plateau was never highly emergent (Chapter II).

Together with rock samples taken from drilling and dredging, recently collected multichannel seismic reflection profiles reveal that the two largest massifs with in Shatsky Rise are large central volcanoes (Sager et al., 2013; Chapter II). Tamu Massif is a single, immense shield volcano, constructed by massive lava flows emanating from the volcano center and extending down the smooth flanks with shallow slopes, perhaps traveling hundreds of kilometers to the surrounding seafloor. Tamu Massif could be the largest single volcano on Earth and has a comparable size to the largest volcano in the Solar System, Olympus Mons on Mars (Sager et al., 2013). Ori Massif has similar structure but is smaller in size than Tamu Massif, implying that it is another large shield volcano. The structure of the massifs implies that they were formed by highly effusive lava flows erupted at small slope angles, which probably resulted from low viscosity and high effusion rate (Self et al., 1997; Self et al., 2008). The size and low morphology of the massifs are significantly different from the thousands of seamounts found throughout the oceans with smaller sizes and steeper flank slopes (Sager et al., 2013; Chapter II).

Shatsky Rise is mostly made up of several large central volcanoes (Sager et al., 1999; Sager et al., 2013; Chapter II) and those volcanoes were formed at a ridge-ridge-ridge triple junction (Sager et al., 1988; Nakanishi et al., 1999). Eruption of massive basaltic piles must therefore have been interacting with spreading ridge tectonic evolution. The morphology of Shatsky Rise in bathymetry should reflect the interaction between the large-scale volcanism and local tectonic evolution. Because seismic

evidence implies that Shatsky Rise volcanoes erupted lavas from their centers, it is expected that flank slopes decline from the central summit of a volcano in all directions. The proximity to the triple junction spreading ridges suggests that the shapes of volcanoes may have been constrained by nearby ridges (whose positions are known from magnetic lineations). In a related development, Shatsky Rise volcanoes were constructed near ridges, so evidence of ridge-related rifting is expected on the flanks of the volcanoes. In addition, the presence of down-to-basin normal faults on the flanks of oceanic plateaus (including Shatsky Rise) has been interpreted to be evidence of differential subsidence, with the plateau center buoyed by subcrustal magmatic underplating (Ito and Clift, 1998).

4.4 Data and methods

Multi-beam sonar data were collected continuously on the *R/V Marcus G. Langseth* during the MGL1004 and MGL1206 cruises using a hull-mounted Simrad-Kongsberg EM122 multi-beam echo sounder. This 12-kHz instrument produced 432 beams per sonar ping in a swath 140 °wide and collected bathymetry data with a resolution of 50 m.

A model T-5 expendable bathymetry thermograph (XBT) was dropped every 24 hours to record temperature profiles to produce sound velocity profiles (SVP), which were used by the multi-beam acquisition software to correct for water column refraction.

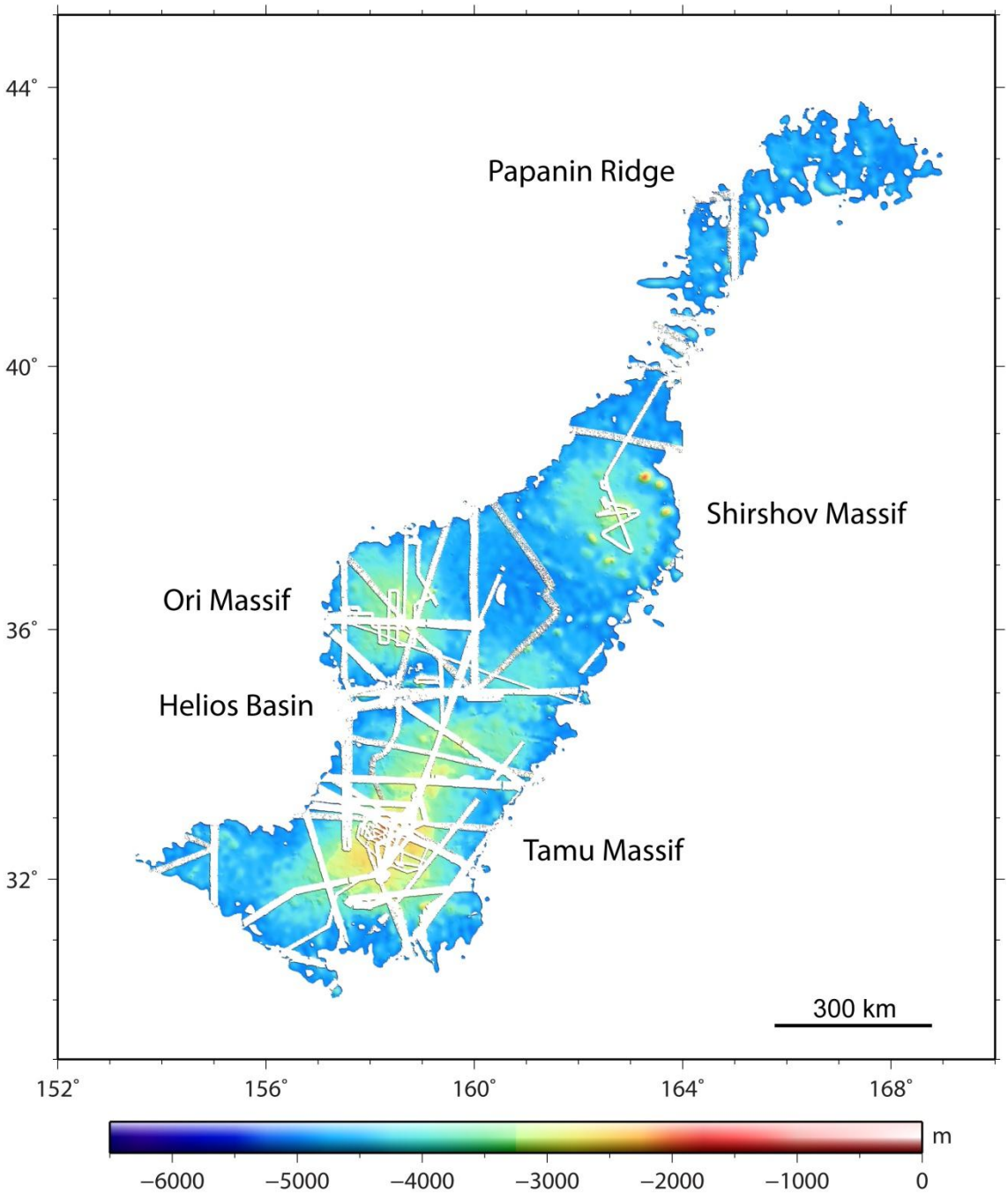

Figure 27. Bathymetry map of Shatsky Rise showing multi-beam bathymetry coverage. Shatsky Rise area <5000 m depth is shown by colored bathymetry. White lines show the swaths of multi-beam survey coverage.

Bathymetry data were processed using MB-System software (Caress and Dale, 1996). Bad soundings were identified as outliers from the otherwise smooth cross-track depth profile and were removed manually. The data were then converted to a net CDF format grid of soundings that can be plotted using GMT software (Wessel and Smith, 1998).

The new bathymetry data were combined with previously-collected bathymetry data from Shatsky Rise, which include an extensive survey collected during *R/V Thomas G. Thompson* cruise TN037 in 1994 (Sager et al., 1999). This survey used a Hydrosweep multi-beam echosounder, which collected a swath with 59 soundings with a width up to twice the water depth. In addition, multi-beam data were available from over 80 incidental ship tracks (61 cruises with multi-beam sonar data) that crossed the rise in the past 50 years. These data were obtained from JAMSTEC and NGDC databases. Different bathymetry data have different resolutions. New multi-beam bathymetry data have the highest resolution of 50 m. To keep this resolution, I would have to grid the entire Shatsky Rise with that spacing, however, this method is impractical, especially because most of those depths estimates would come from oversampled satellite bathymetry. In order to combine new bathymetry data with old bathymetry data, the final bathymetry maps were layered following high to low data resolution, i.e., with MGL1004 and MGL1206 on top, followed by TN037, JAMSTEC, and finally NGDC. This layering method does miss the opportunity to grid the successive data sets where the ship tracks are dense, but these spots are few. Altogether, multi-beam bathymetry data covers less than 20% of the entire Shatsky Rise (Figure 27). In general, the multi-

beam bathymetry coverage is dense at the summit areas of the massifs within Shatsky Rise, but with one notable exception that Helios Basin also has dense data coverage. The lower flanks of the massifs and the basins among them and Papanin Ridge have very sparse coverage. Large gaps in coverage are filled using the global seafloor topography dataset (version 16.1) of Smith and Sandwell (1997) with data resolution of 1 minute grid.

4.5 Results

Shatsky Rise is composed of three large, isolated sub-circular, dome-shaped massifs, a low linear ridge, and a number of small seamounts, mostly located around Shirshov Massif and to its east (Figure 26). The massifs have dome-like shapes and low slopes, whereas the seamounts are typically tall and with steeper slopes. The massifs are therefore morphologically distinct from the seamounts, suggesting that something was fundamentally different about the eruptions. The flank slopes of all three massifs decline from central summits, implying that the massifs are central volcanoes.

4.5.1 Tamu Massif

In a large scale view, Tamu Massif has a dome-like shape and it is elongated along SW-NE (~800 km by 400 km) (Figure 28). It has a generally smooth, flat top because of a thick sediment cap on its summit (Ewing et al.,1966; Zdorovenin et al., 1972; Neprohnov et al., 1984; Karp and Prokudin, 1985; Khankishieyeva, 1989; Sliter and Brown, 1993; Sager et al., 1999). It has gentle flank slopes declining from the

central summit of the massif. Slope angles near the summit are ~1 °but decline to <0.5 ° on the lower flanks (Sager et al., 2013; Chapter II). The broad, dome-like shape and small angle slopes make the massif significantly different in morphology from numerous tall and steeper flanked seamounts all over Shatsky Rise and surrounding seafloor (e.g. a large guyot to the SW of Tamu Massif, and the seamounts in the center of Helios Basin, Figure 29). In addition, the flanks of Tamu Massif are generally parallel to adjacent magnetic lineations or fracture zones, especially for the southwest distal flank and the northeast flank (Figure 26). The southwest flank appears to be somewhat angular and parallel to the surrounding magnetic lineations, suggesting this flank edge is controlled by spreading ridge tectonics. The northeast flank has similar situation that the curved contours are basically parallel to nearby magnetic lineation bights, which is also suggesting the shape of the flank was influenced by ridge evolution. Hence, the overall shape of Tamu Massif is surrounded by magnetic lineations or fracture zones (Figure 26), implying that the outline of the massif is controlled by ridge tectonics.

Although the summit of Tamu Massif appears as a broad dome, it has a shallower, round-topped ridge, called Toronto Ridge (Sager et al., 1999), on the western summit (Figure 28). This large basement ridge is ~1 km tall, linear along a SW-NE axis, ~20 km wide and ~70 km long. It has significantly steeper flank slopes than the summit dome (~ 5 °compared to < 1 °, Chapter II). In addition, Toronto Ridge has many small cones on its surface (Figure 30), probably formed by individual small eruptive vents.

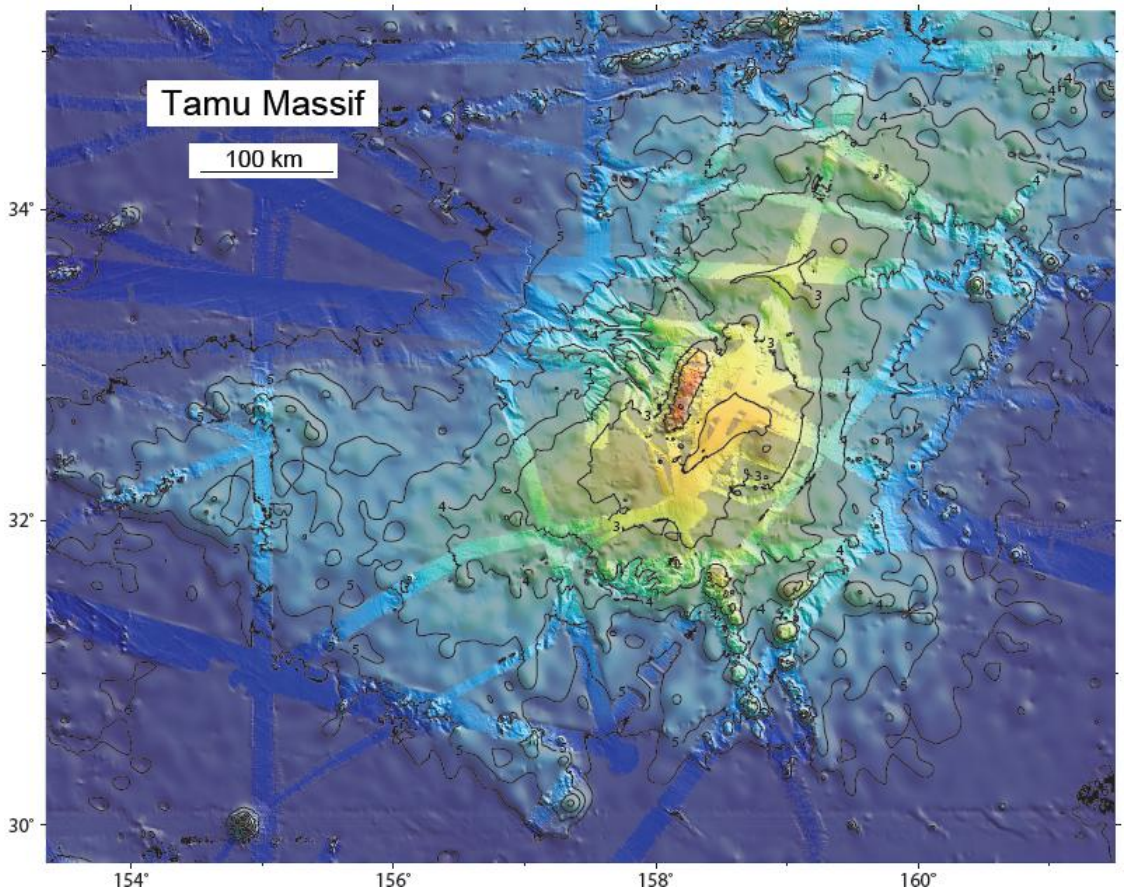

Figure 28. Shaded relief bathymetry map of Tamu Massif. Color scale as in Figure 27.

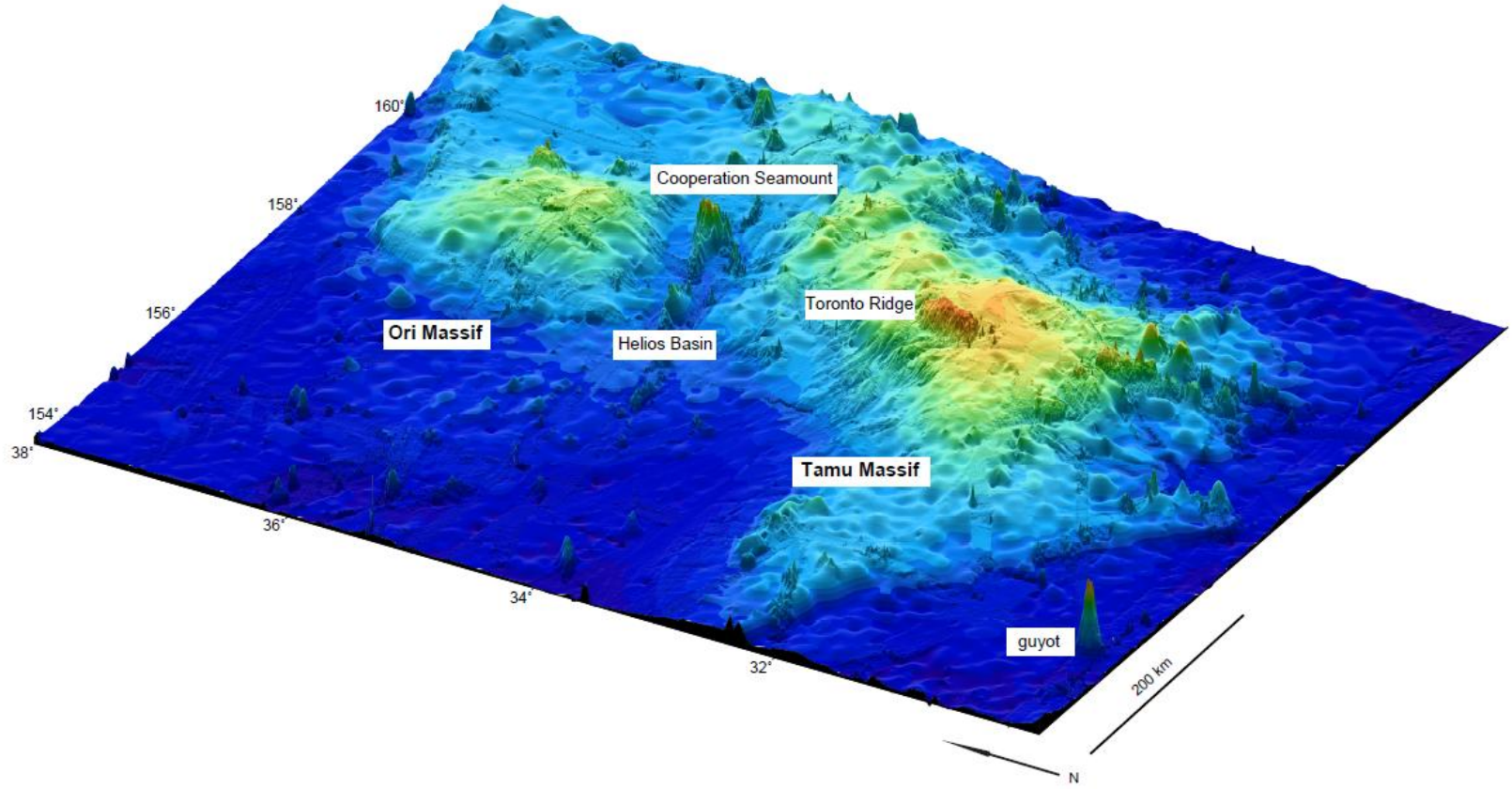

Figure 29. Oblique perspective view of Tamu Massif, Ori Massif and Helios Basin. Color scale as in Figure 27.

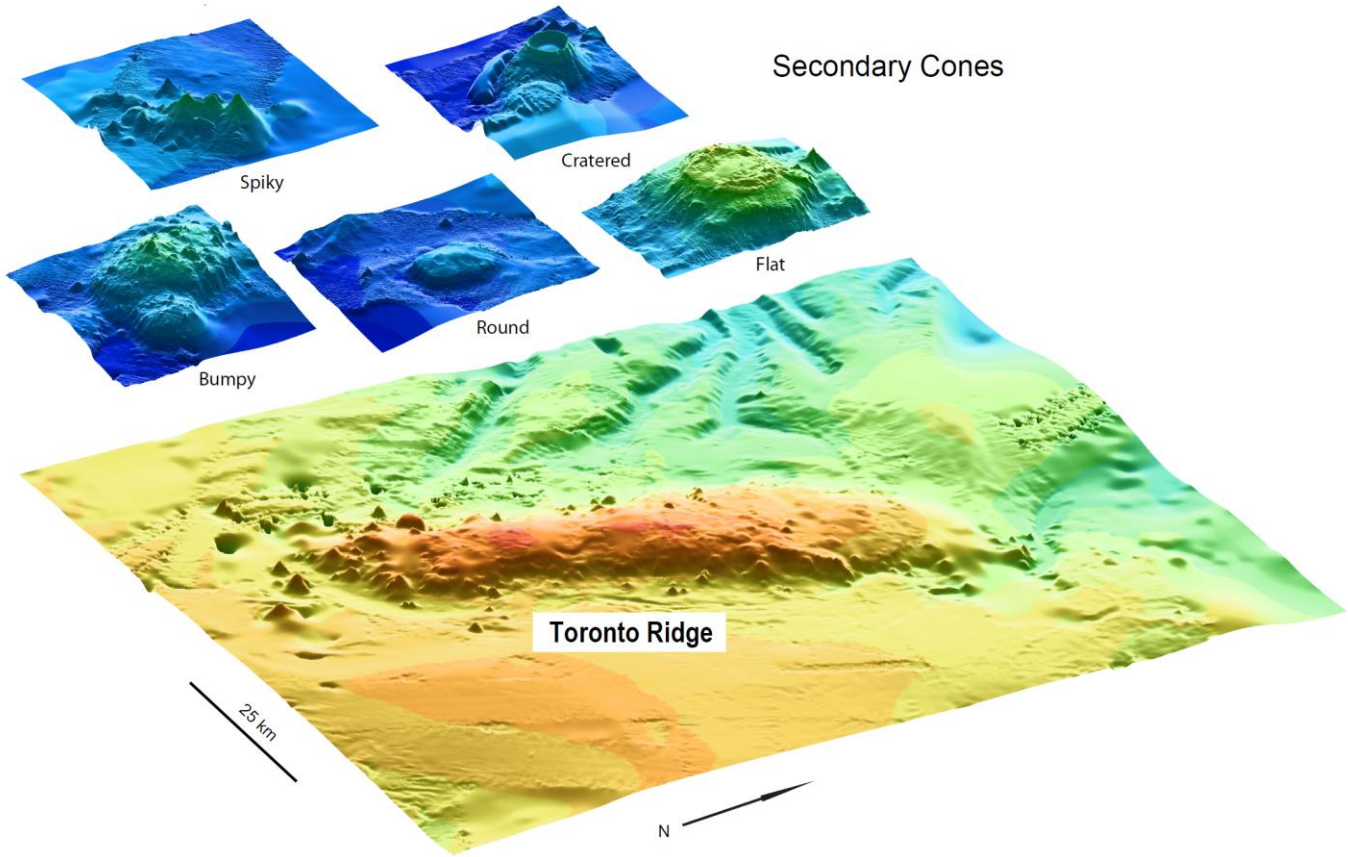

Figure 30. Oblique perspective view of Toronto Ridge and selected secondary cones. Color scale as in Figure 27.

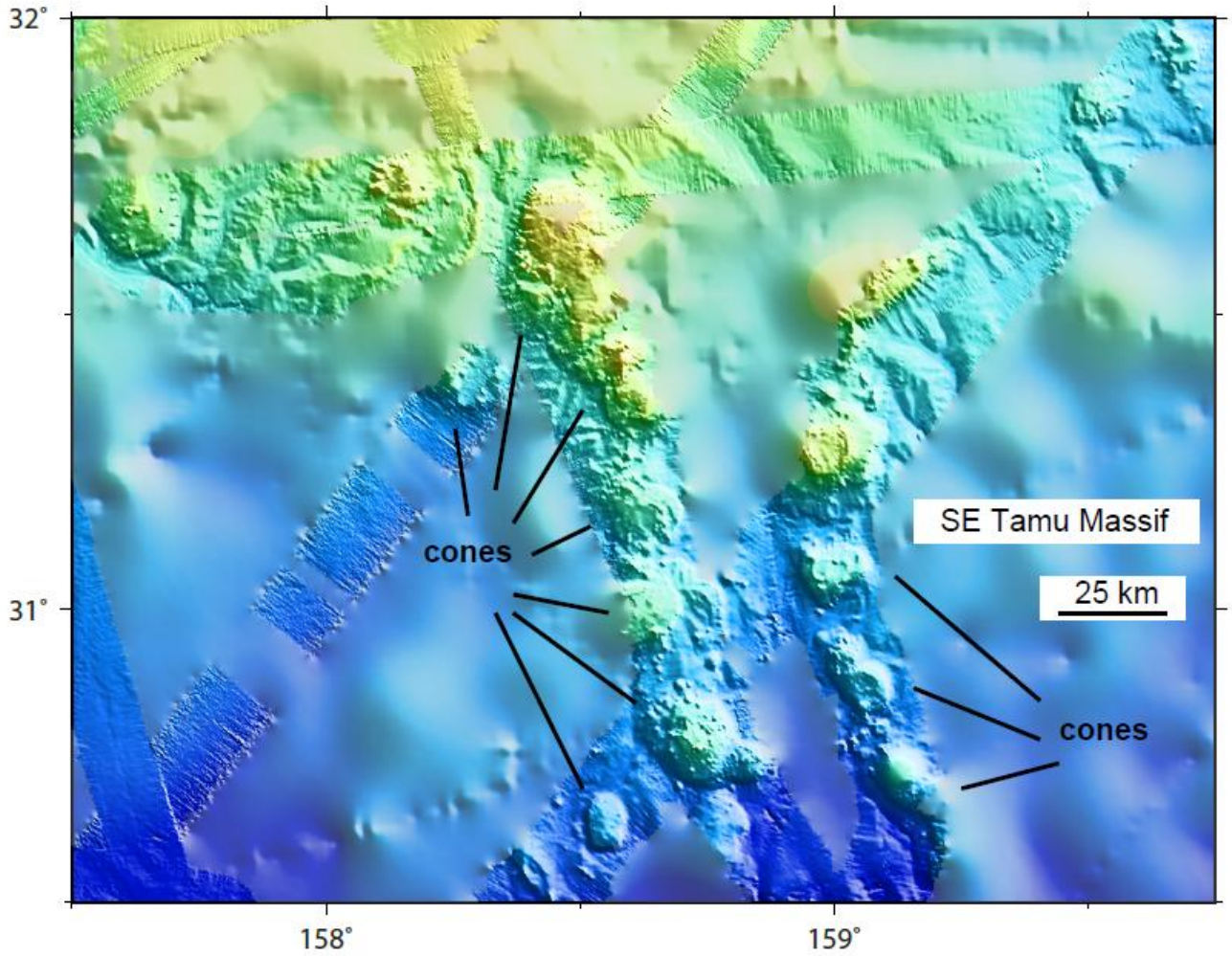

Figure 31. Shaded relief bathymetry map of SE Tamu Massif. Color scale as in Figure 27. Location shown in Figure 26.

Small cones are widely observed on the flanks of Tamu Massif (Figure 28). For example, on the southeast flank of the massif more than 15 cones are mapped (Figure 31). They are generally circular in plan, but sometimes are slightly elongated. They are a few to tens of km in diameter, and 0.5-1 km in height. Their flank slopes are ~5 °or greater (Chapter II). Taking a closer look at these cones in perspective view in Figure 30, they have a variety of appearances, characterized by different tops: spiky (pointy), cratered, bumpy (hummocky), round or flat.

Canyons are seen on the flanks of Tamu Massif in all directions. The northwest flank of the massif shows especially well-developed canyons (Figure 32). On this flank these fettures are generally >100 m deep and ~5-10 km wide. These canyons begin at the edges of the summit sediment cap, and trend from the summit down to the surrounding seafloor. The morphology of the canyons imply that the sediments on the summit edges are spalling off and creating canyons, showing evidence of sediment shedding from the northwest flank. The canyons observed here are similar to other erosional canyons due to mass wasting processes (Hampton et al., 1996). Moreover, seismic profiles show the upper reaches of some canyons near the summit sediment cap with several hundred meters of incision and erosion (Sager et al., 1999; Chapter II).

On the lower flanks of Tamu Massif, channel-like features are seen beside some small ridges (e.g. on the southwest distal flank, Figure 33). The channels extend along the basal contours of the ridges. On crossing seismic profiles, they appear to be formed by erosion of sediments (Chapter II). Channels occur along the base of the ridges with relatively uniform width, probably because of scouring by bottom currents (Habgood et

al., 1993; Marani et al., 2003; Masson et al., 2004). These erosional channels are unlike the erosional canyons on the massif's flanks caused by mass wasting, which are less regular in shape.

Down-to-basin normal faults cut through basement on the lower flanks of the massif are at two locations on the western side of Tamu Massif (Figure 26). Where observed in the bathymetry, the faults are sinuous (Figures 32, 33). Faults appear to be not very straight but slightly curvy. The fault on the west side of Tamu Massif trends ~N5 °E (Figure 32), whereas nearby Japanese magnetic lineations have a trend of ~N60 °E (Figure 26). The two observed on the south flank (Figure 33) have strikes of N25 °W and N75 °W), whereas the nearby Hawaiian magnetic lineations have an average strike of N45 °W (Figure 26). Thus all of the observed faults have strikes that do not follow the magnetic anomaly trends. Additionally, on the southwest flank of Tamu Massif, a small cone is seen atop a fault in the east side of Figure 33. The cone does not seem to be offset by the fault, implying that the cone may have formed after the fault.

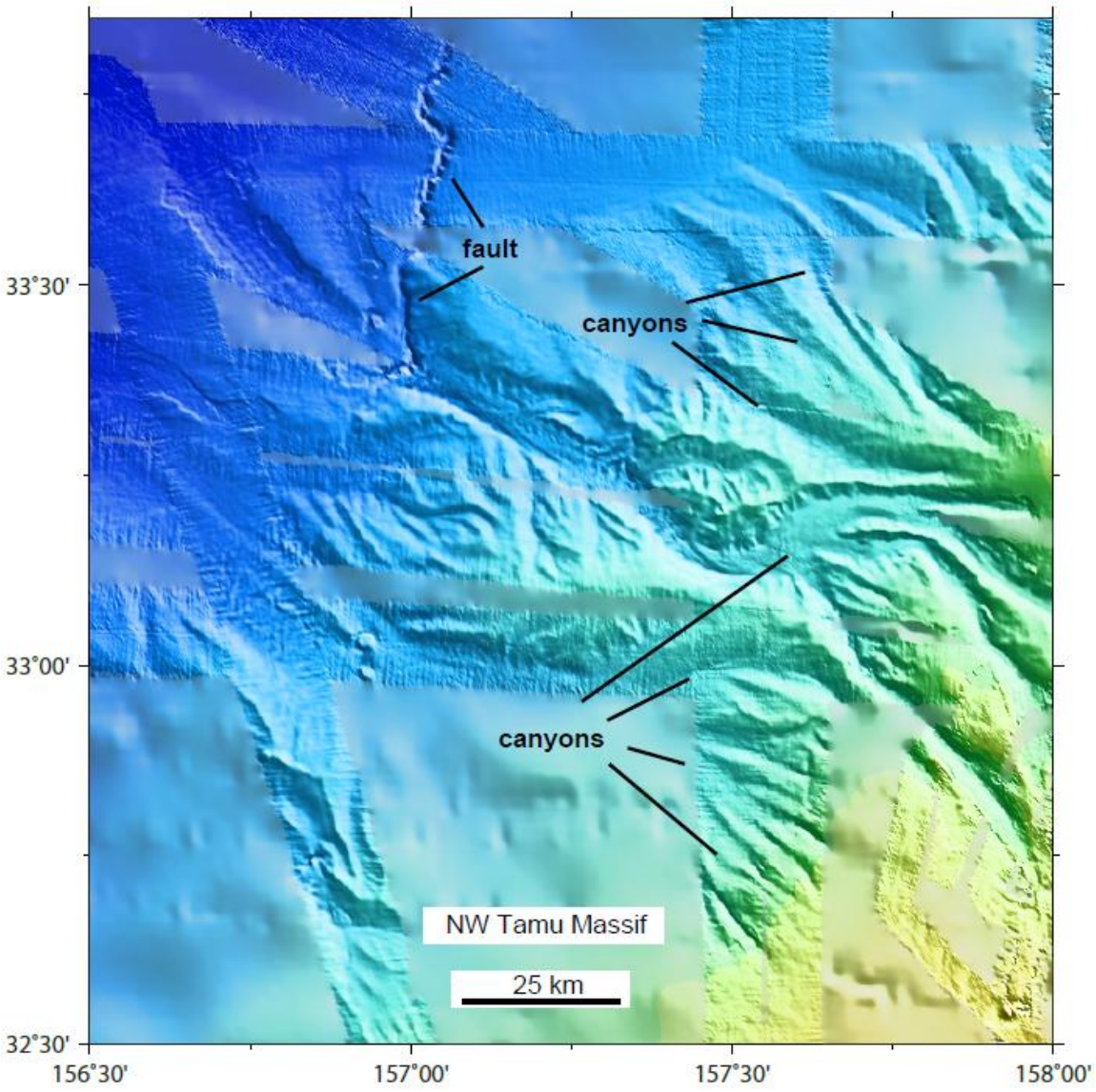

Figure 32. Shaded relief bathymetry map of NW Tamu Massif. Color scale as in Figure 27. Location shown in Figure 26.

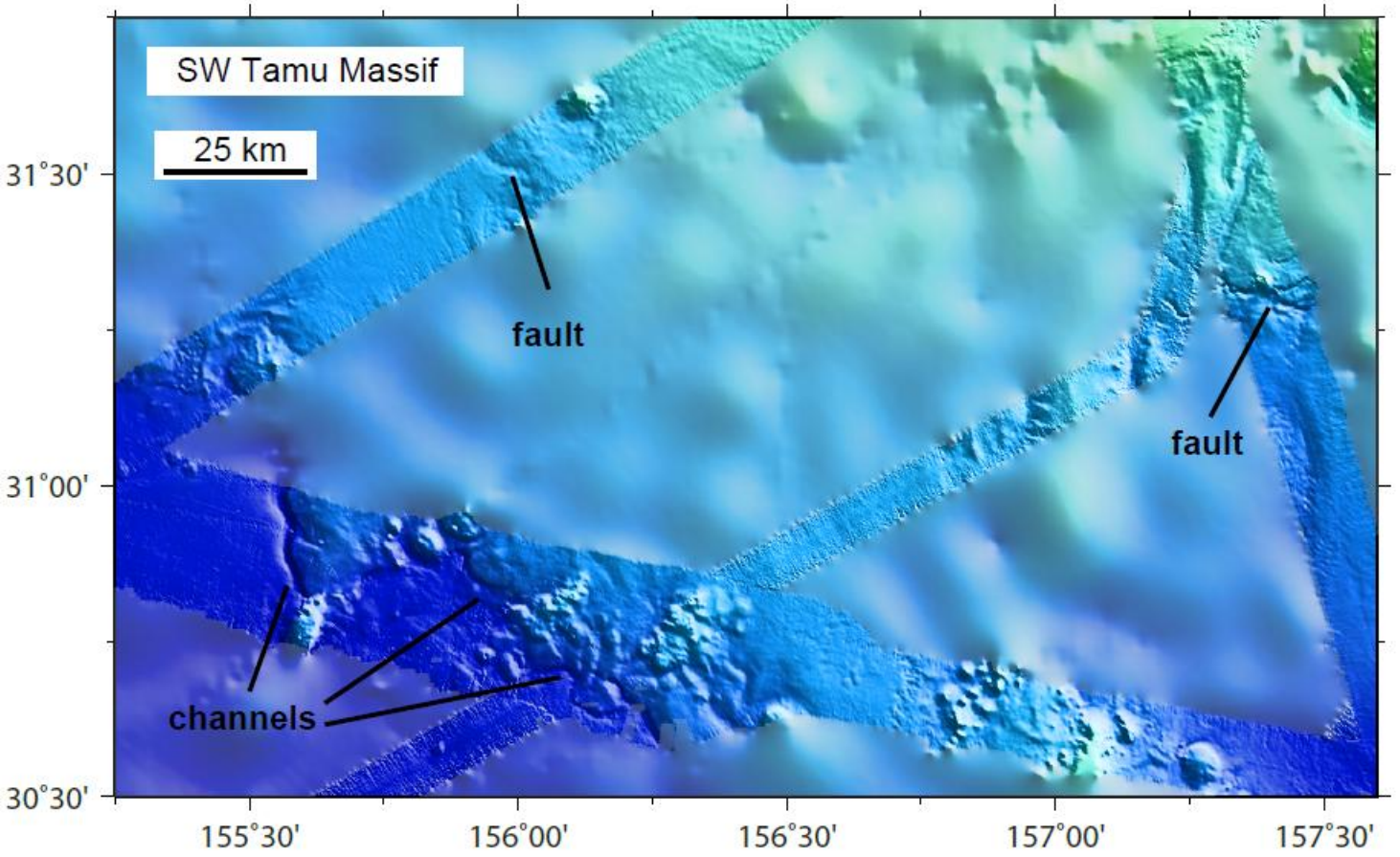

Figure 33. Shaded relief bathymetry map of SW Tamu Massif. Color scale as in Figure 27. Location shown in Figure 26.

4.5.2 Helios Basin

Helios Basin is a rectangular basin between Tamu and Ori massifs with depths > 5 km (Figure 34). The basin is covered by sediment thicknesses of 1-2 km, which is thicker than that in the abyssal plain outside of Shatsky Rise (<1 km), implying that sediments accumulate in the basin between the massifs. These extra sediments may come from the massifs.

Smooth surfaces in the basin show that most of it is buried by sediments with the exception of a linear group of volcanic ridges at the center of the basin (Figure 34). The trend of the linear edifices follows the axis of the basin from east to west, which parallels observed magnetic lineations (Nakanishi et al., 1999) (Figure 26). The largest edifice is called Cooperation Seamount in Sager et al. (1999), an elongated, twin-peaked, basaltic volcano (Figure 35). To the east and west of Cooperation Seamount, there are other linear edifices with similar trends. Linear volcanic ridges are nearly parallel to magnetic lineations (Figure 26), implying that the ridges seem to be related to spreading ridge volcanism. In addition, Helios Basin and magnetic lineations are parallel (Figure 26), which were used to suggest that the basin was formed by rifting of Tamu and Ori massifs by spreading ridges (Sager et al., 1999). Nevertheless, crossing seismic profiles reveal that the sides of the basin are not bounded by large normal faults, as would be expected for a rift basin, suggesting Helios Basin is just a gap in between the two volcanic eruptions (Chapter II).

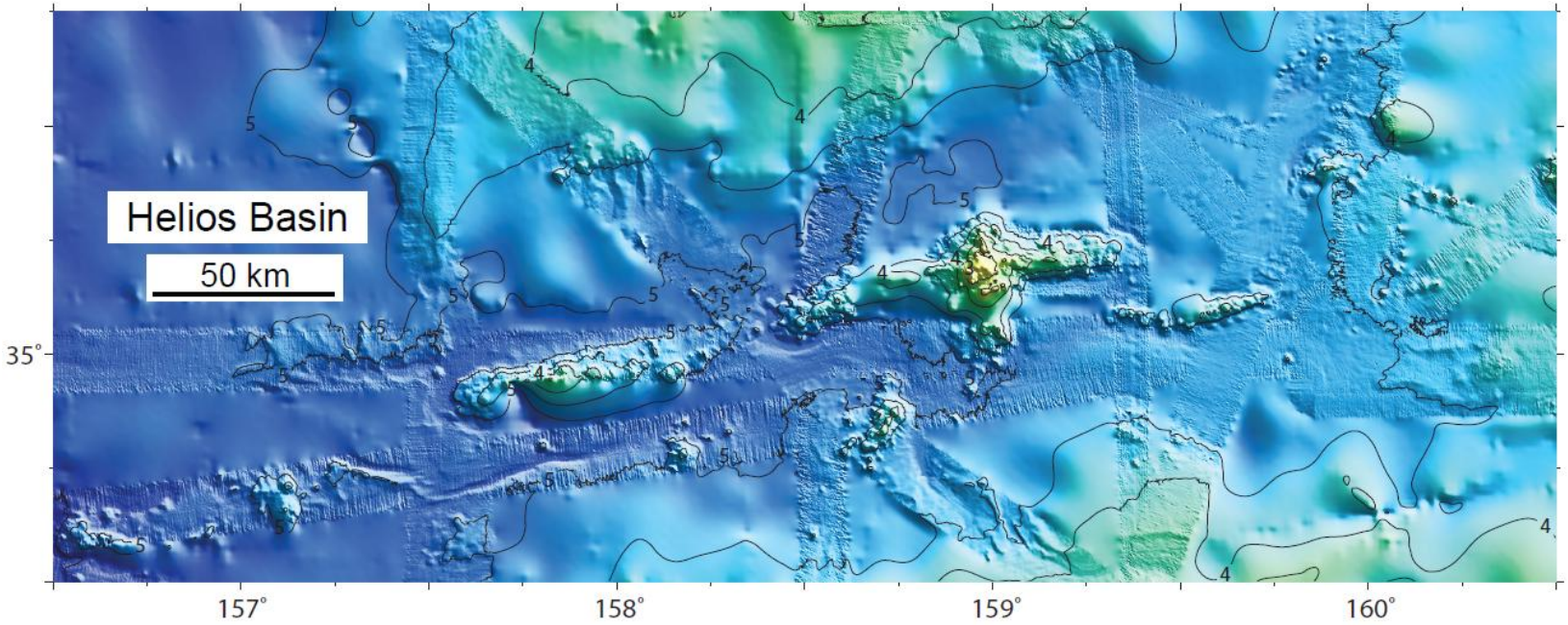

Figure 34. Shaded relief bathymetry map of Helios Basin. Color scale as in Figure 27.

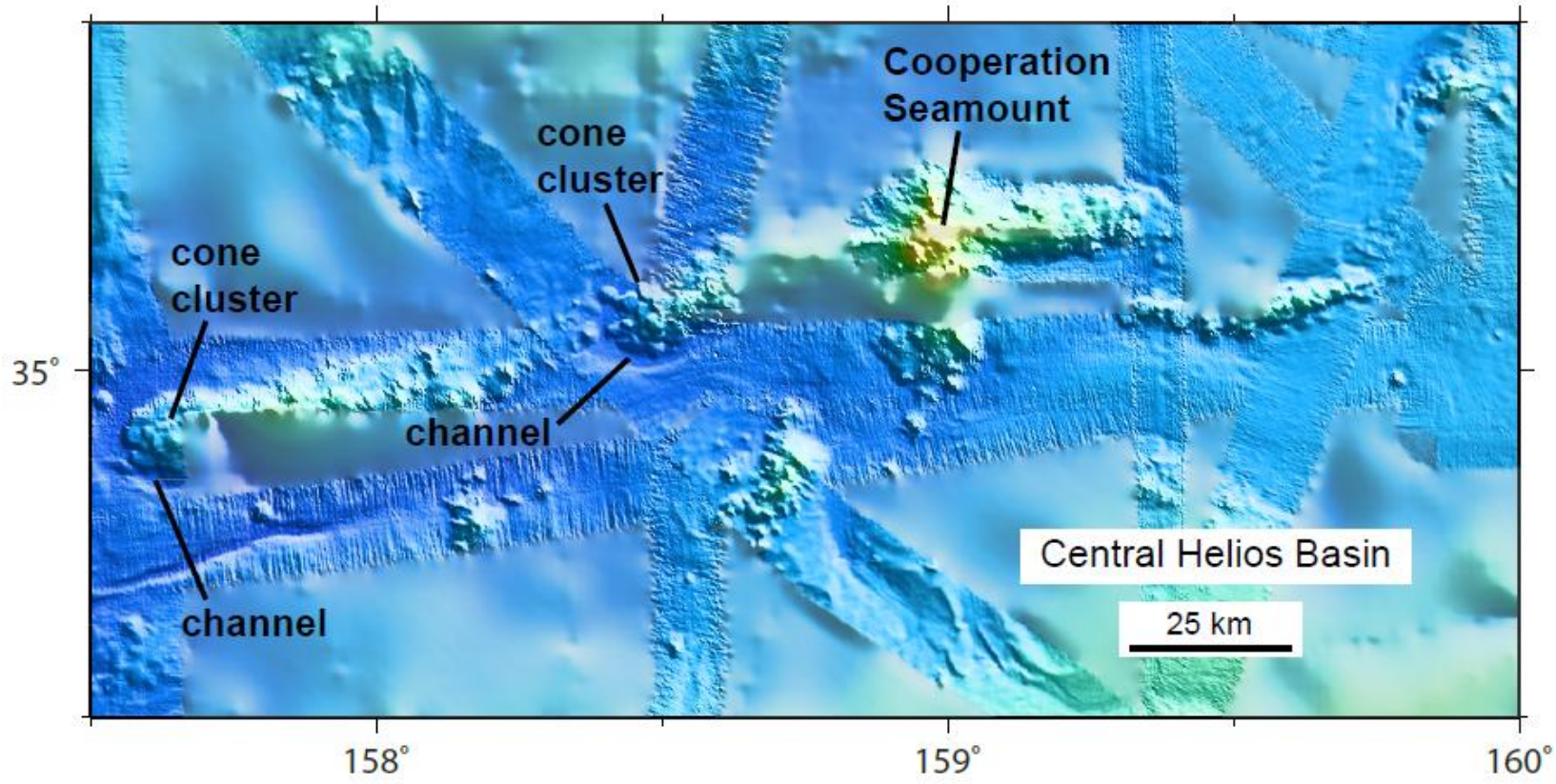

Figure 35. Shaded relief bathymetry map of central Helios Basin. Color scale as in Figure 27. Location shown in Figure 26.

Many small cones are seen on the surfaces of the linear ridges (Figure 35), implying individual small eruptive vents. Some cones are in clusters, and the clusters coalesce to form part of a ridge.

Around the linear ridges, channel-like features are clearly seen (Figure 35). They extend along the basal contours of the ridges, probably resulting from water current scouring (Habgood et al., 1993). Thus, these channels are likely erosional features.

4.5.3 Ori Massif

Ori Massif has a square shape, and it is very equidimensional, unlike the elongated Tamu Massif (Figure 36). The west and east flanks of Ori Massif are N-S, and the north and south flanks are W-E. Magnetic lineations M15 and M16 go through Ori Massif (Figure 26), which may have implied that Ori Massif formed at the spreading ridge. But the trend of the two magnetic lineations is at 45 °to the square shape of Ori Massif's flanks, showing the relationship between the massif and spreading ridges is not definite. However, the outline of Ori Massif is surrounded by adjacent magnetic lineations or fracture zones (Figure 26), implying its overall shape could be affected by ridge tectonic evolution.

The summit of Ori Massif, like Tamu Massif, is also a broad dome, reaching ~3 km depth at its shallowest (Figure 36). Thick sediments (>500 m) bury most basement features on the summit of Ori Massif (Klaus and Sager, 2002; Chapter II), giving the massif a smooth and flat top. On the massif flanks, where the sedimentary coverage is thin, three large cones are exposed to the surface and they are observed in the

bathymetry (Figure 36). Two of them are on the east flank and one is on the north flank. They have a size similar to Toronto Ridge, even though they are not elongated like Toronto Ridge.

Two parallel basement faults on western flank of Ori Massif are observed in the bathymetry as step-like features (Figure 37). The two faults are normal faults, dipping down to basin and striking ~N30 ºE. Although the faults scarps are not as clear as those on Tamu Massif, seismic cross-sections demonstrate conclusively that these steps are faults, with basement offsets of ~200 m (west) and ~180 m (east) (Chapter II). Additionally, the faults are partly covered by a cluster of small cones, implying the faults were formed before those small cones because the cones were not offset.

On the distal west flank of Ori Massif, additional scarps are seen (Figure 37). The scarps appear analogous to fault scarps, but they are highly curved and form box canyons. These scarps are probably the head scarps where mass wasting occurred (Hampton et al., 1996).

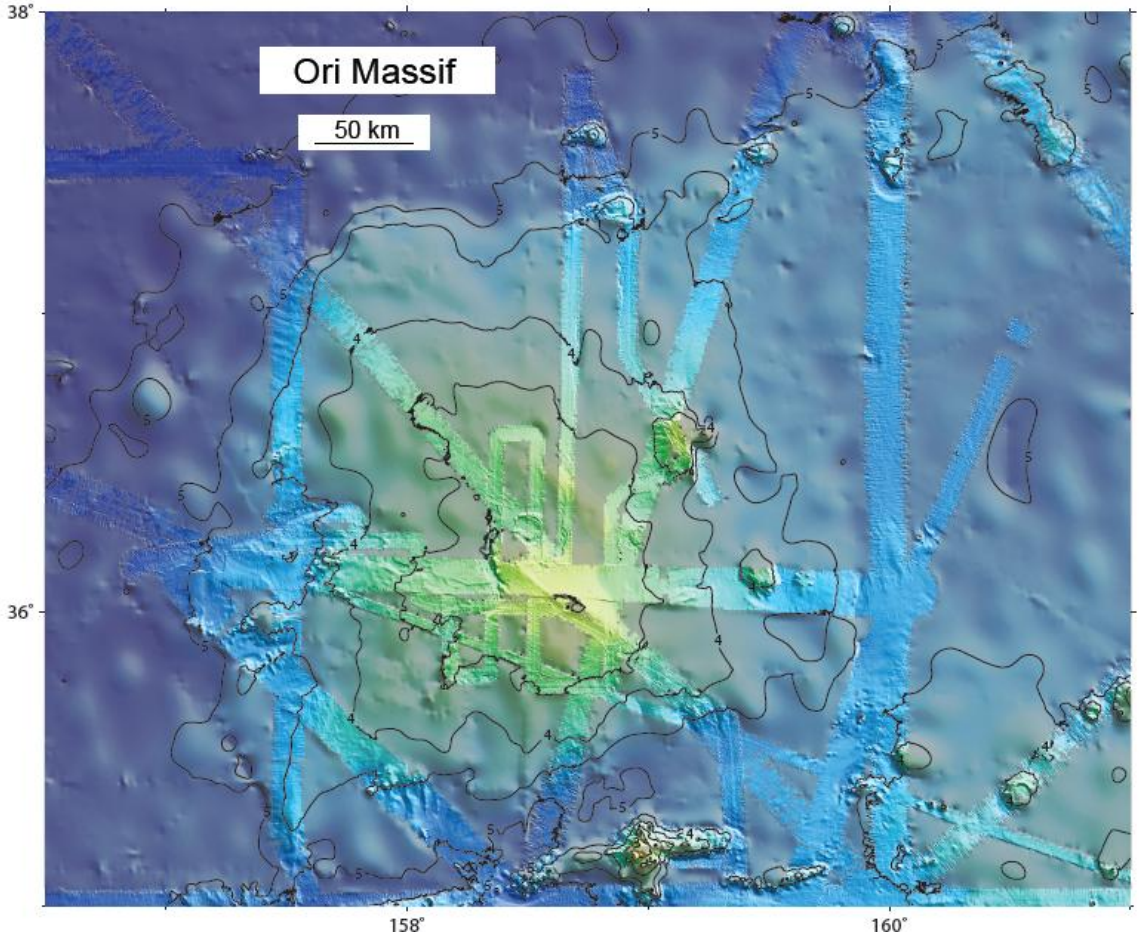

Figure 36. Shaded relief bathymetry map of Ori Massif. Color scale as in Figure 27. Location shown in Figure 26.

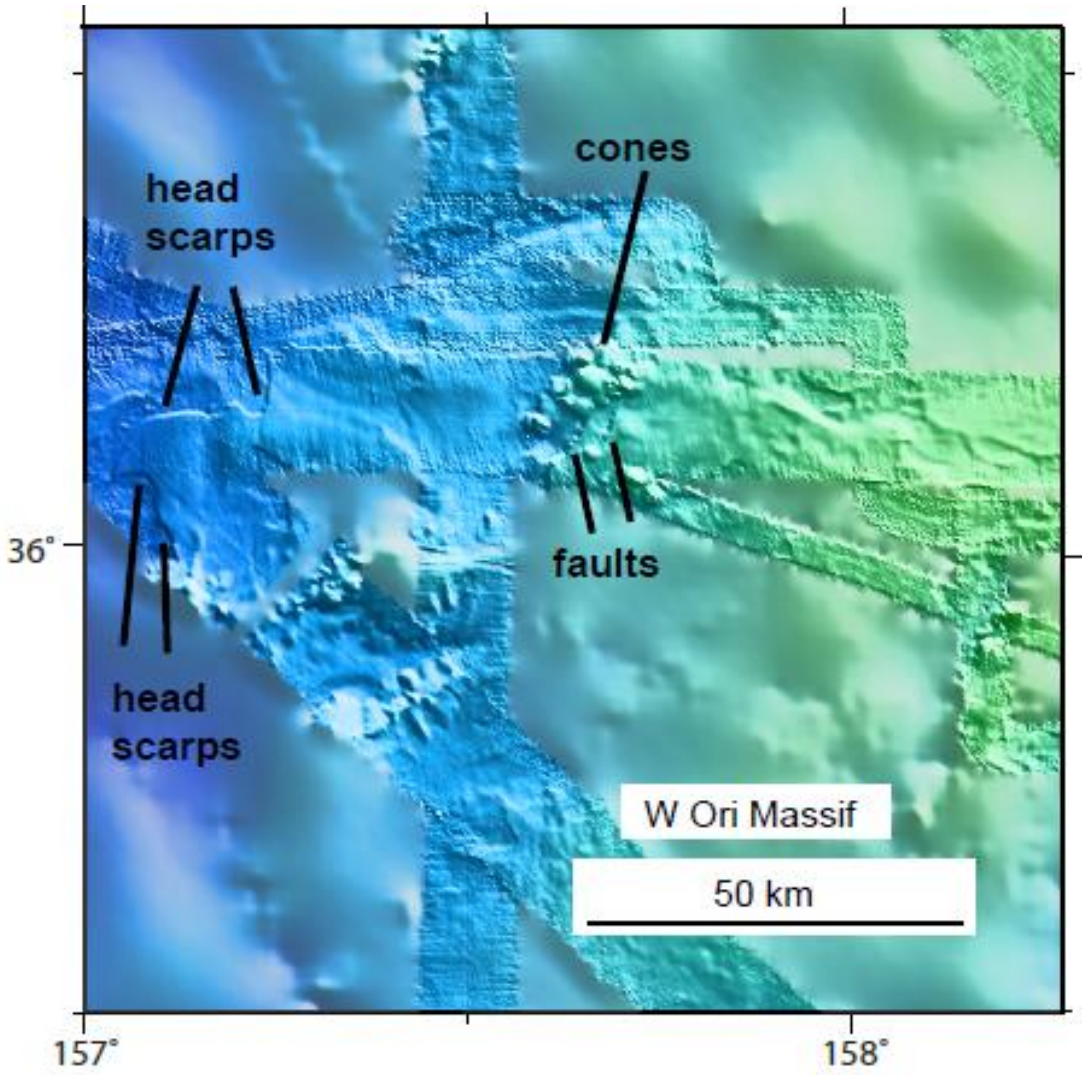

Figure 37. Shaded relief bathymetry map of W Ori Massif. Color scale as in Figure 27. Location shown in Figure 26.

4.6 Discussion

4.6.1 Shatsky Rise massifs and large volcanoes

The most striking morphologic features from Shatsky Rise bathymetry are large massifs. These large volcanic edifices have significantly different morphologies compared to the thousands of seamounts found throughout the oceans (Figure 29). The massifs are much larger in area, and have much shallower slope than the seamounts (<0.5-1.5 °compared to >5 °, Sager et al., 2013; Chapter II). This implies that the massifs formed by different style of volcanic eruptions from the normal seamounts in the oceans. Based on seismic profiles collected over Tamu and Ori massifs and rock samples taken from Integrated Ocean Drilling Program (IODP) core sites, it is thought that such immense dome-like constructs are formed by low viscosity lava flows emanating from the volcano center and extending long distances down the shallow-slope flanks to surrounding seafloor (Sager et al., 2013; Chapter II). The broad dome, shallow slope morphology implies that the erupting lava flows were highly fluid and effusive, so the lavas did not build steep slopes on volcanoes. Massive lava flows recovered from Tamu Massif imply flows erupted at a high effusion rate, with low viscosity and with the potential to travel long distances from their source vents (Shipboard Scientific Party, 2001; Koppers et al., 2010; Sager et al., 2010; 2011). Smaller volume volcanic features with steeper slopes (e.g. common seamounts) must have been erupted with less effusive, more viscous lavas, such as pillow flows (Ballard et al., 1979; McClinton et al., 2013) that do not travel as far.

Shatsky Rise massifs appear to be large isolated domes (Figures 26, 28, 36). Deep-penetration seismic data indicate that Tamu Massif is an immense single central volcano (Sager et al., 2013). Seismic data are limited over Ori Massif, but give a similar picture (Chapter II). Thus, its analogous morphology implies that Ori Massif is also a large shield volcano. No deep-penetration seismic data exist for Shirshov Massif, but its dome-like shape implies the same. Shatsky Rise may be the only oceanic plateau with a trail of individual volcanic massifs. It is not certain why individual, separate volcanoes formed within Shatsky Rise; although, it has been suggested that they occurred because of the Pacific plate drifting over a mantle source with gaps in time between magmatic pulses (Sager et al., 2013). Although, rifting could also split the volcanoes apart, for example, Manihiki Plateau (Beiersdorf and Eringer, 1989; Ai et al., 2008; Uenzelmann, 2012), there is no evidence for the repeated magnetic anomaly sequences that would indicate ridge jumps (Nakanishi et al.,1999). In addition, it does not appear that Shatsky Rise contains faults that would have formed by rifting (Chapter II).

The overall shapes of Shatsky Rise massifs are outlined by surrounding magnetic lineations or fracture zones (Figure 26), suggesting that there could be ridge-hotspot interaction. For instance, Tamu Massif, formed by a massive eruption, could have been a point source volcanism with circular shape, but its elongated shape and somewhat angular southwest may have resulted from ridge tectonics. The angular southwest side of Tamu Massif is bounded by magnetic lineations M21 and M20 (Figure 26), implying ridge control. In addition, the northeast part of Tamu Massif has a shallow slope that is rougher than other flanks as well as features that follow magnetic lineations, implying

ridge crest tectonism. Other oceanic plateaus with similar near-ridge settings to Shatsky Rise also show modification of volcanic flanks by spreading ridge tectonics. For example, the Azores Plateau was also formed at a triple junction and has a triangular shape that follows magnetic anomalies suggesting ridge crest tectonic control (Lourenco et al., 1998). Tamu Massif has magnetic lineations through some parts, but more coherent in others (Figure 26), maybe because some parts were formed at the ridge (e.g. the southwest and northeast ends), but the middle was formed as a massive eruption.

Despite the apparent interaction between Shatsky Rise volcanism and spreading ridge tectonics, only a small number of down-to-basin normal faults are found on the generally smooth massif flanks (Figure 26), providing little evidence of rifting related to spreading ridges. Furthermore, the observed faults do not follow the orientations of the adjacent magnetic lineations (Figure 26) as is expected for ridge-related faults. Although some basement faults may be covered by thick sediments, making them difficult to resolve by bathymetry alone, all of the seismic sections over Shatsky Rise show the same observation that the massif flanks are smooth except for a few down-to-the-basin normal faults, implying that Shatsky Rise volcanoes were not greatly affected by rifting due to spreading ridge tectonics (Chapter II). Faulting is not observed at the surface or on the few seismic lines, maybe because either the faults are missed by data coverage or the volcano covers them over with erupted lava flows. Drilling data show massive flows up until the end of Tamu volcanism, and probably the massive eruption covers the faults.

4.6.2 Down-to-basin normal faults

For the formation of those few down-to-basin normal faults observed on the flanks of Shatsky Rise volcanoes, seafloor spreading is one likely mechanism because of near-ridge setting. It would be expected that ridge-related faults be parallel to the ridges (indicated by magnetic lineations). Large basement faults observed at Shatsky Rise from bathymetry data do not follow the orientations of the adjacent magnetic lineations (Figure 26), implying that the faults may not have been formed by spreading ridge tectonics. Moreover, the north flank of Tamu Massif and Helios Basin are both thought to be faulted because the contours parallel the magnetic lineations (Sager et al., 1999). However, neither bathymetry or seismic profiles from Chapter II shows evidence for such faulting, implying that both the north flank of Tamu Massif and the south flank of Ori Massif are smooth volcanic flanks and Helios Basin is a gap between Tamu and Ori eruptions.

Another explanation given for the observed faulting is differential subsidence, which suggests the volcano center does not subside as much as the flanks due to magmatic underplating (Ito and Clift, 1998). This hypothesis implies that large down-to-basin basement faults should occur all around the volcano flanks, but I only observe such faults on the western flanks of the volcanoes (Figure 26). This unevenly distributed faulting implies either the model is incorrect or the differential subsidence of Shatsky Rise is asymmetric, which is unexpected.

4.6.3 Secondary cones and late-stage volcanism

Bathymetry data show many small cones on the surface of the Shatsky Rise massifs. Many are too small to be resolved in the satellite predicted bathymetry and would otherwise be missed. Most are observed on the flanks of the massifs where the sediment coverage is thin. A few are observed beneath the sediment cap (see Chapter II). Several, such as Toronto Ridge and several large cones on Ori Massif, are large enough to protrude through the sediment cap. The cones range from a few to tens of km in diameter and 0.5-1km in height (Figure 30). Their flanks are steeper than that of the massifs, tending to be >5 °. In general, these cones are circular or sub-circular in plan, but some are elongated, like Toronto Ridge. Most have a round or flat top, some have a top that is bumpy (hummocky), some are spiky (pointy) and some may feature a crater (Figure 30).

Basalts were dredged from Toronto Ridge (Tejada et al., 1998) and some other cones within Shatsky Rise (Sager et al., 1999), revealing the basaltic nature of these features, similar to basaltic cones that form on other large volcanoes (Beiersdorf et al., 1995). However, volcaniclastics recovered from a large buried basement cone from IODP drill site U1348 (Sager et al., 2010), indicating that some cones are formed from this material. Volcaniclastics from Site U1348 were deposited by explosive volcanism (Sager et al., 2011), implying that the buried cone was formed differently from the initial eruption of lava flows that build up Shatsky Rise.

Several lines of evidence imply that at least some of the cone-forming volcanism occurs after the initial shield-building eruptions of Shatsky Rise volcanoes. The

elevation of Toronto Ridge indicates that it occurred after the summit subsided significantly (Sager et al., 2013). Preliminary radiometric dating or rocks dredge from this ridge indicate an age gap of ~8 Myr from the massive lava flows. In addition, the cones that are observed in bathymetry sit atop the lava flows, so they were formed last. They are therefore likely late-stage features. The different form of volcanism, with steeper slopes, also implies that the volcanism that formed Toronto Ridge and other cones was different than the effusive, shield-builing volcanism. Moreover, some cones are large, like Toronto Ridge, contrast with the other smaller cones, implying that some late-stage eruptions are voluminous.

Secondary cones are seen almost everywhere on Shatsky Rise (Figure 29), although they can be buried by thick sediments at the massifs' summits. Seemingly, they are distributed across the massifs at all depths, with no particular area of concentration, implying they may not be tied to any large-scale structure. Since ~50 such cones are observed on the Tamu and Ori massifs with limited bathymetry data coverage of 20%, there must be at least ~250 (=50/20%) secondary cones across Shatsky Rise oceanic plateau (because some cones may be buried the estimate is a minimum). Once secondary cones were thought to be concentrated near volcanic rift zones where there are sources of magma, for example, Hawaiian volcanoes (Macdonald and Abbott, 1970); however, this does not appear to be true for Shatsky Rise because secondary cones occur all over the plateau. The random distribution of such cones implies that this small, secondary eruptions can occur anywhere on the volcano after the shield-building stage.

4.6.4 Erosional canyons and mass wasting

Canyons are commonly seen on flanks of Shatsky Rise volcanoes, as notable as >100 m deep and 5-10 km wide (e.g. Figures 31, 32, 33). Canyons such as those seen in Figure 32 are probably caused by fluid flows, like turbidity currents (Hampton et al., 1996). They show down-slope movement of sediments by the force of gravity. They are likely erosional features due to mass wasting, similar to other mass wasting features on volcanic flanks (e.g. Moore et al., 1989; Lenat et al., 1989; Holcomb and Searle, 1991; Keating et al., 2000; Kristoffersen et al., 2007). Since there is a thick sediment cap at the massif summit and these canyons have their heads in that area, they are likely formed by sediments spalling off the edges of summit sediment cap.

Canyons seem to be unevenly distributed on Tamu Massif. Figure 32 shows that the whole slope of northwest flank of Tamu Massif is a tangle of canyons, whereas figures 31, 33 (on southeast and southwest flanks, respectively) show a few canyons, but not as many. A reason for this difference may be because of locally higher slopes around Toronto Ridge on the northwest flank (Figures 28, 29). Toronto Ridge also dams the sediments on the west side of the summit (Sager et al., 1999) and this may lead to sediments flowing around the edges of the ridge.

4.6.5 Erosional canyons and current scouring

At places on the abyssal plain around Shatsky Rise, I observe erosional channels along the basal contours of some ridges (Figures 33, 35). In bathymetry maps, they are narrower than most of the erosional canyons on the volcanoes' flanks (e.g. Figure 32).

Sometimes they occur on one side of the ridges (e.g. southern distal flank of Tamu Massif, Figure 33). Sometimes they surround the seamounts (e.g. in Helios Basin, Figure 35). These localized features are similar to erosional channels caused by bottom current scouring (Habgood et al., 1993; Marani et al., 2003; Masson et al., 2004). When the flow of a current is obstructed by a ridge, the current velocity increases and carries sediment with it. If the ridge is a small obstruction, water current will transport the sediments around it and create an erosional channel surrounding the ridge (e.g. in Helios Basin, Figure 35). If the ridge is too large an obstruction, the current will scour the sediments on one side of the ridge where the current approaches (e.g. on southern distal flank of Tamu Massif, Figure 33). The current direction is therefore indicated by which side of the seamount is eroded by scouring. For instance, in the case of southern distal flank of Tamu Massif, the erosional channels on the west side of the ridges indicate that the bottom current flowed from west to east.

4.7 Conclusions

High resolution multi-beam sonar data collected on *R/V Marcus G. Langseth* during cruises MGL1004 and MGL1206 are combined with previous bathymetry data to produce an improved bathymetric map of Shatsky Rise oceanic plateau. Because most of Shatsky Rise is covered with only a thin sedimentary layer, the bathymetry reflects the primary shape and structure of the plateau.

Tamu Massif is a huge, slightly elongated, and dome-like volcanic edifice with gentle flank slopes (~0.5 °-1.5 °) declining from a central summit. This suggests it is an

immense central volcano. Ori and Shirshov massifs have similar morphology but with more equidimensional shape and smaller size, implying both are also large central volcanoes. The overall shapes of the massifs are surrounded by adjacent magnetic lineations or fracture zones, implying that their morphology was constrained by ridge tectonic evolution. However, a small number of down-to-basin normal faults are seen on the western flanks of the massifs and the faults were not parallel to magnetic lineations, providing little evidence that the massifs were greatly affected by rifting due to spreading ridge tectonics. Moreover, differential subsidence may cause down-to-basin normal faults on the volcano's flanks, but faults are not seen as ringing around the volcano as would be expected, implying incorrect model or asymmetric Shatsky Rise's subsidence.

Multi-beam data show many cones that are too small to be resolved in the satellite predicted bathymetry and would otherwise be poorly represented. Their small size and steep flank slope (~5 °) distinguish themselves from Shatsky Rise large volcanoes (massifs). They are volcanic cones with different shapes and sizes and are widely-distributed on Shatsky Rise volcanoes, which implies small magma sources scattered across the surface of the volcanoes. These numerous cones probably come from late-stage volcanism, which can either be in the form of lava flows or explosive volcanism.

Erosional canyons occur on the flanks of Shatsky Rise large volcanoes caused by mass wasting and display evidence of down-slope sediment movement. These canyons are likely formed by sediments spalling off the edges of summit sediment cap.

Moreover, some erosional channels exist along the basal contours of some ridges and probably result from bottom current scouring against one side or around the ridges.

CHAPTER V

SUMMARY AND CONCLUSIONS

To gain a better knowledge of Shatsky Rise oceanic plateau and to get a better understanding of oceanic plateau evolution, deep penetrating marine seismic data and high-resolution bathymetry data were newly acquired over the plateau, and these data show the structure and morphology of Shatsky Rise with unprecedented detail. 2D multichannel seismic (MCS) reflection profiles allow us to image the crustal structure of Shatsky Rise. Intra-basement reflections observed in the upper crust are caused by alternations of lava flow packages with differing properties and by thick inter-flow sediment layers, so the reflectors show the structure of lava flows. MCS profiles show that two of the volcanic massifs within Shatsky Rise are immense central volcanoes. Tamu Massif, the largest (~450 × 650 km) and oldest (~145 Ma) volcano, is a single central volcano with rounded shape and shallow flank slopes (<0.5°-1.5°), characterized by lava flows emanating from the volcano center and extending hundreds of kilometers down smooth, shallow flanks to the surrounding seafloor. Ori Massif is another large volcano that is similar, but smaller in size than Tamu Massif. The morphology of the massifs implies formation by extensive and far ranging lava flows emplaced at small slope angles. The relatively smooth flanks of the massifs imply that the volcanoes were not greatly affected by rifting due to spreading ridge tectonics. Observation of deep intra-basement reflectors parallel to the upper basement surface implies long-term isostasy, with the balanced addition of material to the surface and subsurface. No

evidence of subaerial erosion is found at the summits of the massifs, suggesting that they were never highly emergent.

Deep reflectors observed in MCS reflection images are interpreted as the Moho and show the deep crustal structure of Shatsky Rise. MCS reflection sections show Moho reflectors are highly variable in length and shape and strength. This variability is similar to other Moho observations in the oceans, likely resulting from a combination of the change of real Moho structure and the variable imaging conditions owing to the scattering effects in the crust. The Moho reflectors closer to the center of the massifs are weaker, probably because of greater attenuation with depth, masking by multiples, or lower Moho reflectivity due to more melting at the massif center. Moho reflectors start shallow (~7 km) beneath normal crust at the distal flanks of Shatsky Rise and dips (~3-5^{o}) towards the center of plateau massifs, and it can be seen in MCS images up a thickness of ~17 km. Moho depths from MCS reflection data can be matched with those from refraction data, showing that the dip continues toward the middle, reaching maximum thickness of ~ 30 km at the center. Shatsky Rise crustal structure is consistent with the Moho topography of isostatically compensated crustal structures, which is why the plateau exhibits a small free-air gravity anomaly signature. Shatsky Rise was built on young oceanic lithosphere with little rigidity, so the plateau formed in isostatic equilibrium with a deep crustal root.

Bathymetry data show the morphology of Shatsky Rise that it consists of several immense central volcanoes. Tamu Massif is a huge, elongated, and dome-like volcanic edifice with gentle flank slopes declining from a central summit. Ori Massif has similar

morphology but is square shape and smaller in size. The overall shapes of the massifs are surrounded by adjacent magnetic lineations or fracture zones, implying that their morphology was constrained by ridge tectonic evolution. However, a small number of down-to-basin normal faults are seen on the western flanks of the massifs and the faults were not parallel to magnetic lineations, providing little evidence that the massifs were greatly affected by rifting due to spreading ridge tectonics. Moreover, differential subsidence may cause down-to-basin normal faults on the volcano's flanks, but faults are not seen as ringing around the volcano as would be expected, implying incorrect model or asymmetric Shatsky Rise's subsidence. Multi-beam data show many cones that are too small to be resolved in the satellite predicted bathymetry and would otherwise be poorly represented. Their small size and steep flank slope ($\sim 5^0$) distinguish themselves from Shatsky Rise large volcanoes (massifs). They are volcanic cones with different shapes and sizes and are widely-distributed on Shatsky Rise volcanoes, which implies small magma sources scattered across the surface of the volcanoes. These numerous cones probably come from late-stage volcanism, which can either be in the form of lava flows or explosive volcanism. Erosional canyons occur on the flanks of Shatsky Rise large volcanoes caused by mass wasting and display evidence of down-slope sediment movement. These canyons are likely formed by sediments spalling off the edges of summit sediment cap. Moreover, some erosional channels exist along the basal contours of some ridges and probably result from bottom current scouring against one side or around the ridges.

REFERENCES

Ai, H. A., Stock, J. M., Clayton, R., and Luyendyk, B., 2008, Vertical tectonics of the High Plateau region, Manihiki Plateau,Western Pacific, from seismic stratigraphy, Marine Geophysical Researches, v. 29, p. 13-26.

Anderson, D. L., Tanimoto, T., and Zhang, Y. S., 1992, Plate tectonics and hotspots: the third dimension, Science, v. 256, p. 1645-1651.

Ballard, R. D., Holcomb, R. T., and Van Andel, T. H., 1979, The Galapagos Rift at 86 ℃W: sheet flows, collapse pits, and lava lakes of the rift valley, Journal of Geophysical Research, v. 84, p. 5407-5422.

Beiersdorf, H., Bach, W., Duncan, R., Erzinger, J., and Weiss, W., 1995, New evidence for the production of EM-type ocean island basalts and large volumes of volcaniclastics during the early history of the Manihiki Plateau, Marine Geology, v. 122, p. 181-205.

Bercovici, D., and Mahoney, J., 1994, Double flood basalts and plume head separation at the 660-kilometer discontinuity, Science, v. 266, p. 1367-1369.

Borissova, I., Coffin, M. F., Charvis, P., and Operto, S., 2003, Structure and development of a microcontinent: Elan Bank in the southern Indian Ocean, Geochemistry Geophysics Geosystems, v. 4(9), p. 1071-1088.

Bryan, S. E., Peate, I. U., Peate, D. W., Self, S., Jerram, D., Mawby, M., R., Marsh, J. S., and Miller, J. A., 2010, The largest volcanic eruptions on Earth, Earth-science Reviews, v. 102(3), p. 207-229.

Campbell, I. H., 2005, Large igneous provinces and the mantle plume hypothesis, Elements, v. 1(5), p. 265-269.

Caress, D. W., and Dale, N. C., 1996, Improved processing of Hydrosweep DS multibeam data on the R/V Maurice Ewing, Marine Geophysical Researches, v. 18(6), p. 631-650.

Carlson, R. L., and Raskin, G. S., 1984, Density of the ocean crust, Nature, v. 311, p. 555-558.

Charvis, P., and Operto, S., 1999, Structure of the Cretaceous Kerguelen Volcanic Plateau: evidence for wide-angle seismic data, Journal of Geodynamics, v. 28, p. 51-71.

Coffin, M. F., and Eldholm, O., 1994, Large igneous provinces: crustal structure, dimensions, and external consequences, Reviews of Geophysics, v. 32, p. 1-36.

Collier, J. S., Buhl, P., Torne, M., and Watts, A. B., 1994, Moho and lower crustal reflectivity beneath a young rift basin: results from a two-ship, wide-aperture seismic-reflection experiment in the Valencia Trough (western Mediterranean), Geophysical Journal International, v. 118, p. 159-180.

Collins, J. A., Brocher, T. M., and Karson, J. A., 1986, Two-dimensional seismic reflection modeling of the inferred fossil oceanic crust/mantle transition in the Bay of Islands Ophiolite, Journal of Geophysical Research, v. 91, p. 12520-12538.

Courtillot, V., Davaille, A., Besse, J., and Stock, J., 2003, Three distinct types of hotspots in the Earth's mantle, Earth and Planetary Science Letters, v. 205(3), p. 295-308.

Den, N., Ludwig, W. J., Murauchi, S., Ewing, J. I., Hotta, H., Edgar, N. T., Yoshii, T., Asanuma, T., Hagiwara, K., Sato, T., and Ando, S., 1969, Seismic refraction measurements in the northwest Pacific Basin, Journal of Geophysical Research, v. 74, p. 1421-1434.

Dieterich, J. H., 1988, Growth and persistence of Hawaiian volcanic rift zones, Journal of Geophysical Research, v. 93, p. 4258-4270.

Duncan, R. A., and Richards, M. A., 1991, Hotspots, mantle plumes, flood basalts, and true polar wander, Reviews of Geophysics, v. 29, p. 31-50.

Ewing, M., Saito, T., Ewing, J. I., Burckle, L. H., 1966, Lower Cretaceous sediments from the northwest Pacific, Science, v. 152(3723), p. 751-755.

Fitton, J. G., Mahoney, J. J., Wallace, P. J., and Saunders, A. D., 2004, Leg 192 synthesis: origin and evolution of the Ontong Java Plateau, Proceedings of the ODP, Scientific Results, v. 192, p. 1-18.

Floyd, P., 1991, Oceanic Islands and Seamounts in Oceanic Basalts, Van Nostrand Reinhold, New York, p. 174-218.

Foulger, G. R., 2007, The plate model for the genesis of melting anomalies, Plates, Plumes, and Planetary Processes, edited by Foulger, G. R., and Jurdy, D. H., Special Papers GSA, Boulder, p. 1-28.

Furumoto, A., Webb, M. O., and Hussong, D., 1976, Seismic studies in the Ontong-Java Plateau, Tectonophysics, v. 34, p. 71-90.

Gallart, J., Vidal, N., and Danobeitia, J. J., 1995, Multichannel seismic image of the crustal thinning at the NE Iberian margin combining normal and wide angle reflection data, Geophysical Research Letters, v. 22 (2), p. 489-492.

Gettrust, J. F., Furukawa, K., and Kroenke, L. W., 1980, Crustal structure of the Shatsky Rise from seismic refraction measurements, Journal of Geophysical Research, v. 85, p. 5411-5415.

Gladczenko, T. P., Coffin, M. F., and Eldholm, O., 1997, Crustal structure of the Ontong Java Plateau: modeling of new gravity and existing seismic data, Journal of geophysical Research, v. 102, p. 27711-27722.

Gohl, K., and Uenzelmann-Neben, G., 2001, The crustal role of the Agulhas Plateau, southwest Indian Ocean: evidence from seismic profiling, Geophysical Journal International, v. 144, p. 632-646.

Gradstein, F. M., Ogg, J. G., and Smith, A. G., 2004, A Geologic Time Scale, Cambridge University Press, Cambridge.

Habgood, E. L., Kenyon, N. H., Masson, D. G., Akhmetzhanov, A., Weaver, P. P. E., Gardner, J., and Mulder, T., 2003, Deep-water sediment wave fields, bottom current sand channels and gravity flow channel-lobe systems: Gulf of Cadiz, NE Atlantic, Sedimentology, v. 50(3), p. 483-510.

Hampton, M., Lee, H., and Locat, J., 1996, Submarine Slides, Reviews of Geophysics, v. 34, p. 33-59.

Hilde, T. W., Isezaki, C. N., and Wageman, J. M., 1976, Mesozoic seafloor spreading in the north central Pacific, Geophysics of the Pacific Ocean Basin and Its Margin: a Volumn in Honor of George P. W., Geophysical Monograph Series, p. 205-226.

Hoernle, K., Hauff, F., Werner, R., and Mortimer, N., 2004, New insights into the origin and evolution of the Hikurangi oceanic plateau, Eos Transactions of the AGU, v. 85(41), p. 401-408.

Holbrook, W. S., Reiter, E. C., Purday, G. M., and Toksoz, M. N., 1992, Image of the Moho across the continent-ocean transition, U.S. east coast, Geology, v. 20, p. 203-206.

Holcomb, R., and Searle, R., 1991, Large slides from oceanic volcanoes, Marine Geotechnology, v. 10(1-2), p. 19-32.

Houtz, R. E., and Ludwig, W. J., 1979, Distribution of reverberant subbottom layers in the southwest Pacific basin, Journal of Geophysical Research, v. 84, p. 6003-6010.

Ingle, S., and Coffin, M. F., 2004, Impact origin for greater Ontong Java Plateau, Earth and Planetary Science Letters, v. 218, p. 123-134.

Inoue, H., Coffin, M. F., Nakamura, Y., Mochizuki, K., and Kroenke, L. W., 2008, Intra-basement reflections of the Ontong Java Plateau: implications for plateau construction, Geochemistry Geophysics Geosystems, v. 9, p. 29-38.

Ito, G., and Clift, P. D., 1998, Subsidence and growth Pacific Cretaceous plateaus, Earth and Planetary Science Letters, v. 161, p. 85-100.

Jerram, D.W., and Widdowson, M., 2005, The anatomy of Continental Flood Basalt Provinces: geological constraints on the processes and products of flood volcanism, Lithos, v. 79, p. 385-405.

Karp, B. Y., and Prokudin, V. G., 1985, The structure of the sedimentary layer on the Shatsky Rise according to seismic data, Geology, v. 3, p. 26-33.

Kashintsev, G. L., and Suzymov, A. Y., 1981, Basalts of the Shatsky Rise, SSSR, v. 258(4), p. 218-238.

Kearey, P., Klepeis, K. A., and Vine, F. J., 2009, Global Tectonics, third edition, Wiley-blackwell, UK, p. 108-168.

Keating, B., Helsley, C., and Karogodina, I., 2000, Sonar studies of submarine mass wasting and volcanic structures off Savaii Island, Samoa, Pure and Applied Geophysics, v. 157(6-8), p. 1285-1313.

Kesthelyi, L., and Self, S., 1998, Some physical requirements for the emplacement of long basaltic lava flows, Journal of Geophysical Research, v. 103(B11), p. 27447-27464.

Khankishiyeva, L. M., 1989, The structure and seismostratigraphy of the sedimentary cover on the Shatsky Rise (Pacific Ocean), Okeanologiya, v. 29, p. 178-183.

Kim, S. S., and Wessel, P., 2011, New global seamount census from altimetry-derived gravity data, Geophysical Journal International, v. 186(2), p. 615-631.

Klaus, A., and Sager, W.W., 2002, Data report: high-resolution site survey seismic reflection data for ODP Leg 198 drilling on Shatsky Rise, northwest Pacific.

Koppers, A. A. P., Sano, T., Natland, J. H., Widdowson, M., Almeev, R., Greene, A. R., Murphy, D. T., Delacour, A., Miyoshi, M., Shimizu, K., Li, S., Hirono, N., Geldmacher, J., and the Expedition 324 Scientists, 2010, Massive basalt flows on the southern flank of Tamu Massif, Shatsky Rise: a reappraisal of ODP Site 1213 basement units, Proceedings of IODP Expedition 324.

Korenaga, J., 2005, Why did not the Ontong Java Plateau form subaerially?, Earth and Planetary Science Letters, v. 234, p. 385-399.

Korenaga, J., and Sager, W.W., 2012, Seismic tomography of Shatsky Rise by adaptive importance sampling, Journal of Geophysical Research, v. 117, p. 1-26.

Kristoffersen, Y., Coakley, B. J., Hall, J. K., and Edwards, M., 2007, Mass wasting on the submarine Lomonosov Ridge, central Arctic Ocean, Marine Geology, v. 243, p. 132-142.

Larson, R. L., and Chase, C. G., 1972, Late Mesozoic evolution of the western Pacific Ocean, Geological Society of America Bulletin, v. 83, p. 3627-3644.

Lenat, J., Vincent, P., and Bachelery, P., 1989, The off-shore continuation of an active basaltic volcano Piton de la Fournaise (Reunion Island, Indian Ocean): structural and geomorphological interpretation from seabeam mapping, Journal of Volcanology and Geothermal Research, v. 36(1-3), p. 1-36.

Lourenco, N., Miranda, J. M., Luis, J. F., Ribeiro, A., Mendes-Victor, L. A., Madeira, J. and Needham, H. D., 1998, Morpho-tectonic analysis of the Azores Volcanic Plateau from a new bathymetric compilation of the area, Marine Geophysical Researches, v. 20, p. 141-156.

Ludwig, W. J., and Houtz, R. E., 1979, Isopach map of sediments in the Pacific Ocean basin and marginal sea basins, American Association of Petrolem Geologists.

MacDonald, G. A., 1972, Volcanoes: Prentice Hall, Englewood Cliffs, NJ.

MacDonald, G. A., and Abbott, A. T., 1970, Volcanoes in the Sea: Honolulu, HI, University of Hawaii Press.

Mahoney, J. J., Duncan, R. A., Tejada, M. L. G., Sager, W. W., and Bralower, T. J., 2005, Jurassic-Cretaceous boundary age and mid-ocean ridge type mantle source for Shatsky Rise, Geology, v. 33, p. 185-188.

Mahoney, J. J., and Spencer, K. J., 1991, Isotopic evidence for the origin of the Manihiki and Ontong Java oceanic plateaus, Earth and Planetary Science Letters, v. 104, p. 196-210.

Marani, M., Argnani, A., Roveri, M. and Trincardi, F., 1993, Sediment drifts and erosional surfaces in the central Mediterranean: seismic evidence of bottom-current activity, Sedimentary Geology, v. 82, p. 207-220.

Masson, D. G., Wynn, R. B., and Bett, B. J., 2004, Sedimentary environment of the Faroe-Shetland and Faroe Bank Channels, north-east Atlantic, and the use of bedforms as indicators of bottom current velocity in the deep ocean, Sedimentology, v. 51(6), p. 1207-1241.

McClinton, T., White, S. M., Colman, A., and Sinton, J. M., 2013, Reconstructing lava flow emplacement processes at the hotspot-affected Galapagos spreading center, 95 º W and 92 ºW, Geochemistry Geophysics Geosystems, in press.

Mengel, K., and Kern, H., 1992, Evolution of the petrological and seismic Moho-implications for the continental crust-mantle boundary, Terra Nova, v. 4, p. 109-116.

Mitchell, N. C., 2001, Transition from circular to stellate forms of submarine volcanoes, Journal of Geophysical Research, v. 106(2), p. 1987-2003.

Mitchum, R. M., Vail, P. R., and Sangree, J. B., 1977, Seismic stratigraphy and global changes in sea level, part 6: stratigraphic interpretation of seismic reflection patterns in depositional sequences, Seismic Stratigraphy – Applications to Hydrocarbon Exploration, edited by Payton, C. E., American Association of Petroleum Geologists, Tulsa, OK, p. 117-143.

Miura, S., Sueyehiro, K., Shinohara, M., Takahashi, N., Araki, E., and Taira., A., 2004, Seismological structure and implications of collision between the Ontong Java Plateau and Solomon Island Arc from ocean bottom seismometer-airgun data, Tectonophysics, v. 389, p. 191-220.

Mjelde, R., Sellevoll, M. A., Shimamura, H., Iwasaki, T., and Kanazawa, T., 1993, Crustal structure beneath Lofoten, north Norway, from vertical incidence and wide-angle seismic data, Geophysical Journal International, v. 114, p. 116-126.

Moore, J. G., Clague, D. A., Holcomb, R. T., Lipman, P. W., Normark, W. R., and Torresan, W. E., 1989, Prodigious submarine landslides on the Hawaiian Ridge, Journal of Geophysical Research, v. 94(B12), p. 17465-17484.

Mutter, J. C., 1985, Seaward dipping reflectors and the continent-ocean boundary at passive continental margins, Tectonophysics, v. 114, p. 117-131.

Mutter, J. C., and Carton, H. D., 2013, The Mohorovicic discontinuity in ocean basins: some observations from seismic data, Tectonophysics, in press.

Nakanishi, M., Sager, W. W., and Klaus, A., 1999, Magnetic lineations within Shatsky Rise, northwest Pacific Ocean: implications for hot spot-triple junction interaction and oceanic plateau formation, Journal of Geophysical Research, v. 104, p. 7539-7556.

Nakanishi, M., Sager, W. W., and Korenaga, J., 2013, Reorganization of the Pacific-Izanagi-Farallon triple Junction in Late Jurassic: tectonic events before the formation of the Shatsky Rise, GSA Special Papers, in press.

Nedimovic, M. R., Carbotte, S. M., Harding, A. J., Detrick, R. S., Caniles, J. P., Diebold, J. B., Kent, G. M., Tischer, M., and Babcock, J. M., 2005, Frozen magma lenses below the oceanic crust, Nature, v. 436, p. 1149-1152.

Neprohnov, Y. P., Merklin, L. R., and Khankishiyeva, L. M., 1984, Map of distribution of the sedimentary cover on the Shatskiy Rise, SSSR, v. 277, p. 628-638.

Parsiegla, N. K., Gohl, K., and Uenzelmann-Neben, G., 2008, The Agulhas Plateau: structure and evolution of a large igneous province, Geophysical Journal International, v. 174, p. 336-350.

Planke, S., and Edholm, O., 1994, Seismic response and construction of seaward dipping wedges of flood basalts: Voring volcanic margin, Journal of Geophysical Research, v. 99, p. 9263-9278.

Planke, S., Symonds, P. A., Alvestad, E., and Skogseid, J., 2000, Seismic volcanostratigraphy of large-volume basaltic extrusive complexes on rifted margins, Journal of Geophysical Research, v. 105, p. 19335-19351.

Pueringer, M., Sager, W. W., Ooga, M., Housen, B., Carvallo, C., and Tominaga, M., 2013, Paleomagnetism of igneous rocks from Shatsky Rise and implications for oceanic plateau volcanism, GSA Special Papers, in press.

Richards, M. A., Duncan, R. A., and Courtillot, V. E., 1989, Flood basalts and hot-spot tracks: plume heads and tails, Science, v. 246, p. 103-107.

Richards, M. A., Jones, D. L., Duncan, R. A., and Depaolo, D. J., 1991, A mantle plume initiation model for the Wrangellia flood basalt and other oceanic plateaus, Science, v. 254 (5029), p. 263-267.

Ridley, V. A., and Richards, M. A., 2010, Deep crustal structure beneath large igneous provinces and the petrologic evolution of flood basalt, Geochemistry Geophysics Geosystems, v. 11, p. 35-44.

Rogers, G. C., 1982, Oceanic plateau as meteorite impact signatures, Nature, v. 299, p. 341-342.

Rohr, K. M. M., Milkereit, B., and Yorath, C. J., 1988, Asymmetric deep crustal structure across the Juan de Fuca Ridge, Geology, v. 16, p. 533-537.

Rossi, M. J., 1996, Morphology and mechanism of eruption of postglacial shield volcanoes in Iceland, Bulletin of Volcanology, v. 57, p. 530-540.

Rotstein, Y., Schlich, R., and Munschy, M., 1992, Structure and tectonic history of the southern Kerguelen Plateau (Indian Ocean) deduced from seismic reflection data, Tectonics, v. 11, p. 1332-1347.

Rutten, M. G., 1964, Formation of a plateau basalt series (from the example of Iceland), Bulletin of Volcanology, v. 27, p. 93-111.

Sager, W. W., 2005, What built Shatsky Rise, a mantle plume or ridge tectonics? GSA Special Papers, v. 388, p. 721-733.

Sager, W. W., and Han H. C., 1993, Rapid formation of Shatsky Rise oceanic plateau inferred from its magnetic anomaly, Nature, v. 364, p. 610-613.

Sager, W. W., Handschumacher, D. W., Hilde, T. W. C., and Bracey, D. R., 1988, Tectonic evolution of the northern Pacific plate and Pacific-Farallon-Izanagi triple junction in the Late Jurassic and Early Cretaceous (M21-M10), Tectonophysics, v. 155, p. 345-364.

Sager, W. W., Kim, J., Klaus, A., Nakanishi, M., and Khankishieva, L. M., 1999, Bathymetry of Shatsky Rise, northwest Pacific Ocean: implications for ocean plateau development at a triple junction, Journal of Geophysical Research, v. 104, p. 7557-7576.

Sager, W. W., Sano, T., Geldmacher, J., and the Expedition 324 Scientists, 2010, Proceedings of the IODP Expedition 324, p. 1-68.

Sager, W. W., Sano, T., and Geldmacher, J., 2011, How do oceanic plateaus form? Clues from drilling at Shatsky Rise. Eos Transactions of the AGU, v. 92, p. 37-44.

Sager, W. W., Zhang, J., Korenaga, J., Sano, T., Koppers, A. A. P., Mahoney, J., and Widdowson, M., 2013, An immense shield volcano within Shatsky Rise oceanic plateau, northwest Pacific Ocean, Nature Geoscience, v. 10, p. 1-6.

Sandwell, D. T., and MacKenzie, K. R., 1989, Geoid height versus topography for oceanic plateaus and swells, Journal of Geophysical Research, v. 94, p. 7403-7418.

Sandwell, D. T., and Smith, W. H. F., 1997, Marine gravity anomaly from Geosat and ERS-1 satellite altimetry, Journal of Geophysical Research, v. 102, p. 10039-10054.

Saunders, A. D., 2005, Large igneous provinces: origin and environmental consequences, Elements, v. 1, p. 259-263.

Self, S., Jay, A. E., Widdowson, M., and Keszthelyi, L. P., 2008, Correlation of the Deccan and Rajamundry trap lavas: are these the longest and largest flows on Earth? Journal of Volcanology and Geothermal Research, v. 173, p. 3-19.

Self, S., Thordarson, T., and Keszthelyi, L., 1997, Large Igneous Provinces, Continental, Oceanic, and Planetary Flood Volcanism, edited by Mahoney, J. J., and Coffin, M. F., Geophysical Monograph Series, AGU, p. 381-410.

Shipboard Scientific Party, 2001, Leg 192 Summary, Proceedings of the Ocean Drilling Program, Initial Reports, edited by Mahoney, J. J., Fitton, J. G., and Wallace, P. J., Ocean Drilling Program, College Station, TX, p. 1-88.

Sigmundsson, F., 2005, Iceland Geodynamics: Crustal Deformation and Divergent Plate Tectonics, Springer, UK, p. 68-98.

Singh, S. C., Harding, A. J., Kent, G. M., Sinha, M. C., Combier, V., Bazin, S., Tong, C. H., Pye, J. W., Barton, P. J., Hobbs, R. W., White, R. S., and Orcutt, J. A., 2006,

Seismic reflection images of the Moho underlying melt sills at the East Pacific Rise, Nature, v. 442, p. 287-290.

Sliter, W. V., and Brown, G. R., 1993, Shatsky Rise: seismic stratigraphy and sedimentary record of Pacifc paleoceanography since the Early Cretaceous, Proceedings of the ODP, Scientific Results, v. 132, p. 3-13.

Smith, D. K., 1988, Shape analysis of Pacific seamounts, Earth and Planetary Science Letters, v. 90, p. 457-466.

Smith, W. H. F., 1993, On the accuracy of digital bathymetric data, Journal of Geophysical Research, v. 98, p. 9591-9603.

Smith, W. H. F., and Sandwell, D. T., 1994, Bathymetric prediction from dense satellite altimetry and sparse shipboard bathymetry, Journal of Geophysical Research, v. 99(11), p. 21803-21824.

Smith, W. H. F., and Sandwell, D. T., 1997, Global seafloor topography from satellite altimetry and ship depth soundings, Science, v. 277, p. 1957-1962.

Spitzer, R., White, R. S., Christie, P. A. F., and the iSIMM Team, 2008, Seismic characterization of basalt flows from the Faroes margin and the Faroe-Shetland basin, Geophysical Prospecting, v. 56, p. 21-31.

Talwani, M., Pichon, X. L., and Ewing, M., 1965, Crustal structure of the mid-ocean ridges, computed model from gravity and seismic refraction data, Journal of Geophysical Research, v. 70(2), p. 342-352.

Tejada, M. L. G., Mahoney, J. J., Sager, W. W., and Shipboard Scientific Party, 1995, Isotopic study of basement rocks from Shatsky Rise, northwest Pacific Ocean, Eos Transactions of the AGU, v. 76(46), p. 699-718.

Trehu, A. M., Klitgord, K. D., Sawyer, D. S., and Buffler, R. T., 1989, Atlantic and Gulf of Mexico Continental Margins, edited by Pakiser, L. C., and Mooney, W. D., Geophysical Society of America Memoir, p. 349-382.

Tryggvason, E., and Bath, M., 1961, Upper crustal structure of Iceland, Journal of Geophysical Research, v. 66(6), p. 1913-1925.

Uenzelmann-Neben, G., 2012, The expedition of the research vessel Sonne to the Manihiki Plateau in 2012 (So 224): reports on polar and marine research, Bremerhaven, Alfred Wegener Institute for Polar and Marine Research, v. 656 , p. 70-90.

Uenzelmann-Neben, G., Gohl, K., Ehrhart, A., and Seargent, M., 1999, Agulhas Plateau, SW Indian Ocean: new evidence for excessive volcanism, Geophysical Research Letters, v. 26, p. 1941-1944.

Vogt, P. R., and Smoot, N. C., 1984, The Geisha Guyots: multibeam bathymetry and morphometric interpretation, Journal of Geophysical Research, v. 89(B13), p. 11085-11107.

Vuong, A. K., Zhang, J., Gibson, R. L. Jr., and Sager, W. W., 2013, Application of the 2D continuous wavelet transform to image of Shatsky Rise plateau using marine seismic data, GSA Special Papers, in press.

Walker, G. P. L., 2000, Encyclopedia of Volcanoes, edited by Sigurdsson, H., Houghton, B., Rymer, H., Stix, J., and McNutt, S., Academic, p. 283-289.

Watts, A. B., and Ribe, N. M., 1984, On geoid heights and flexture of the lithosphere at seamounts, Journal of Geophysical Research, v. 89 (B13), p. 11152-11170.

Wessel, P., 2001, Global distribution of seamounts inferred from gridded Geosat/ERS-1 altimetry, Journal of Geophysical Research, v. 106(B9), p. 19431-19441.

Wessel, P., and Smith, W. H. F., 1998, New improved version of Generic Mapping Tools released, Eos Transactions of the AGU, v. 79(47), p. 579-579.

White, R. S., MacKenzie, D., and O'Nions, R. K., 1992, Oceanic crustal thickness from seismic measurements and rare earth element inversions, Journal of Geophysical Research, v. 97(B13), p. 19683-19715.

Winterer, E. L., and Sager, W. W., 1995, Synthesis of drilling results from the Mid-Pacific Mountains: regional context and implications, Proceedings of the Ocean Drilling Program, Scientific Results, v. 143, p. 497-535.

Zdorovenin, V. V., Shekhvatov, B.V., Kuzmin, V.A., Suzyumov, A.Y., Filatyev, V.P., and Sheina, L.P., 1972, Origin of the sedimentary cover of the Shatsky Rise, SSSR, v. 202, p. 368-383.